

DISS. ETH NO. 22442

From Powder to Technical Body: Structured Zeolite Catalysts with Enhanced Functionality

A thesis submitted to attain the degree of
DOCTOR OF SCIENCES of ETH ZURICH

(Dr. sc. ETH Zurich)

presented by

NINA-LUISA MICHELS

M.Sc. ETH, École Polytechnique Fédérale de Lausanne, Switzerland

born on 20.05.1986

citizen of Germany

accepted on the recommendation of

Prof. Dr. J. Pérez-Ramírez, examiner

Prof. Dr. M. Morbidelli, co-examiner

Dr. N. Marti, co-examiner

Dr. S. Mitchell, co-examiner

2014

To the ones I love

Acknowledgments

Each thesis bears the signature of its author, and yet it is never the work of a single individual but of an ensemble of people contributing towards its realization. I would like to take this unique rhetorical moment to convey my genuine gratitude for their invaluable support and intellectual, personal, and moral assistance.

First and foremost, I wish to express my sincere gratitude to Prof. Dr. Javier Pérez-Ramírez, my Doktorvater, for giving me this opportunity of conducting the doctoral studies in this exceptional environment; the fascinating topic of research, a real niche in academia, the good organization, and the excellent facilities – just to name a few. Javier, thank you for your thoughtful guidance, timely support, and inspiration through all the cycles of ups-and-downs, giving me the impulse to push forward in the right direction. I greatly appreciate all the efforts and time you invested in my academic and personal development, having taught me that dedication, passion, diligence, and communication are a few of the most important skills to master if you want to succeed. You give me a lifetime of unforgettable memory, full of advice, lessons learned, and invaluable experience, from which I will often draw in the future.

Prof. Dr. Massimo Morbidelli is kindly acknowledged for agreeing to act as co-examiner to my thesis.

My special thanks go to my external co-referee, Dr. Nadia Marti, firstly, for her interest in my work, and secondly, for the close industrial collaboration we enjoyed with Zeochem AG (Uetikon, Switzerland), scaling-up hierarchical ZSM-5 and unveiling some of the secrets of catalyst structuring.

I would also like to deeply thank my third co-examiner, Dr. Sharon Mitchell, who has worked together with me from day one, and whose valuable scientific input was essential to shape this thesis into its final form. Sharon, thanks so much for the devoted supervision and tremendous help during these past four years. I particularly appreciate the patience and support you showed me, cheering me on in moments when everything seemed gloomy.

The research in this thesis has also benefited from a number of fruitful collaborations. Zeochem AG (Uetikon, Switzerland) is acknowledged for providing the infrastructure and sharing of expertise in the scale-up of hierarchical zeolites, in particular, Dr. Nadia Marti and Dr. Mandy Erdmann, for contributing to the results presented in Chapter 2. Dr. Frank Krumeich for analysis of several samples by TEM and SEM. BASF SE (Ludwigshafen, Germany) is thanked for testing the zeolite extrudates in the conversion of methanol to olefins (Chapter 3). A major part of this thesis would not have been imaginable without the expertise of the team at the Scientific Center for Optical and Electron Microscopy (ScopeM). Dr. Karsten Kunze is sincerely thanked for having contributed to the work presented in Chapter 3, and instructing me on the use of Leo1530 (SEM microscopy) and NVision40 (FIB-SEM tomography), to whom I became very much attached, despite their inherent mood swings and freezing atmosphere. Moreover, I am grateful to Dr. Miriam Lucas and Dr. Tobias Schwarz for the CSLM work, Maja Günthert for her training on specimen preparation (microtome), and Dr. Joakim Reutler, Dr. Anne-Greet Bittermann, and Dr. Roger Wepf for help and advice. Special thanks also goes to the TOMCAT beamline team at the Swiss Light Source (Paul Scherrer Institute, project no. 20110115), in particular Prof. Dr. Marco Stampanoni, Dr. Federica Marone, and Dr. Rajmund Mokso, for their support with the synchrotron radiation X-ray tomographic microscopy (SRXTM) measurements (Chapter 3). Maria Milina, who has been my longtime office-sister, is thanked for conducting the diffusion studies (Chapter 4). Dr. Lars Borchardt for his collaboration on the thermal conductivity project, and Torsten Nowak (Fraunhofer Institute for Reliability and Microintegration, Berlin, Germany) for conducting the thermography imaging (Chapter 5).

Furthermore, the Swiss National Science Foundation (project no. 200021-134572) is acknowledged for financial support.

Special thanks go to all aCe teammates for providing a very enjoyable, humorous, and positive working atmosphere, being always generous with their time to respond to questions, concerns, and for discussions throughout the four years of this research. Outside the lab, I will remember unforgettable although sporadic social moments that we shared (handbag-stolen-night, wine-tastings, Balkenprobe, Superkondi, *etc.*). I want to thank my friends that I met

during my stay at ETH for smoothing my research time, making it more fun, or just being there to chat – Sabrina (co-editor of the corridor gradient and ETH-Grazie), Janne (lunch-companion and ETH-Grazie), Renata (BFF and Superkondi-teammate), Amaia and Daniela (Ladies-Breakfast). I am also grateful to Flurina Attinger Ochsner for administrative assistance, and to several individuals vital for the proper functioning of daily laboratory equipment, for their instant help, and always-knowing-a-solution: René Verel (NMR), Roland Walker (mechanical workshop), Max Wohlwend (electrical workshop), Andreas Dutly (lab safety), and Erol Dedeoglu (IT).

My heartfelt gratitude goes especially to my family and friends for their love, care, and friendship, and for their unconditional support in any decision that I made. My mum (Nike-Sabine), my confidant, for always believing in me, telling me that I could do whatever I set my mind to, and for whom I am the scientist among 10'000 others. My dad (Volker) for always putting his Industriechemiker back on the track of reality, and for valuing the education of my sister and me as the best-possible investment. My little Sis (Pia-Alina), greatest Nervensäge ever but most precious, for just being her true self and making me laugh when I needed it most. Grandpa Billi, whom I followed in his engineering footsteps, and who was my mentor. Grandpa, I made it! Ömchen for the continuous flow of letters (I won't need the jam anymore). Minischwuun for reliable transport to and from ETH (despite some undesired tickets). Augustin, my fiancé, for his reliability and constant support, who is always there for me to lean on and encouraged me even when I am a bit chiente.

Finally, pursuing my doctoral studies in this beautiful country has been stimulating, hard work, and a great experience. I have received most useful advice throughout the duration of my thesis, but all the faults that remain are obstinately my own.

Table of Contents

Acknowledgments	iii
Table of Contents	vii
Summary	ix
Zusammenfassung	xiii
1 Introduction	1
2 Scale-Up of Hierarchical ZSM-5 Zeolite into Technical Bodies	21
3 Visualizing Hierarchical ZSM-5 Zeolite Bodies from Macro to Nano Length Scales	35
4 Effects of Binders on the MTH Performance of Shaped Hierarchical ZSM-5 Zeolites	53
5 Structuring Zeolite Bodies for Enhanced Heat-Transfer Properties	77
6 Conclusions and Outlook	91
Bibliography	101
Appendix A Annexes	115
Appendix B List of Publications	133
Appendix C Presentations	135
Appendix D Cover Gallery	137
Appendix E Curriculum Vitae	143

Summary

Progress in heterogeneous catalysis has been, is, and will always be motivated by societal needs (*e.g.*, environment, energy, chemicals, fuels), with the ultimate aim of improving process efficiency on a technical scale. Technical catalysts are typically complex bodies comprising the active phase(s) and numerous additives, introduced to optimize a particular function, and ranging from tens of microns to several centimeters in size suitable for their commercial application. They can differ strongly in composition, structure, porosity, and performance from research catalysts, *i.e.*, laboratory-developed materials constituted by a single bulk or supported active phase in powder form, which are the predominant focus of academic investigations. However, despite the tremendous relevance, no clear fundamental guidelines exist for their technical manufacture, encompassing the up-scaled preparation, formulation, and structuring, which is often shrouded in secrecy.

In zeolite catalysis, which accounts for approximately 10–13% of the global catalyst market by value, only a handful of the 218 existing framework types have been commercialized. It is believed that an improved understanding of the scale-up process would facilitate the translation of novel zeolite materials to an industrial context. This century, developments in the synthesis of zeolite catalysts have increasingly focused on the attainment of hierarchically-structured materials, in which an auxiliary network of meso/macropores enhances the active site accessibility, leading to improved catalytic performance at laboratory scale. Taking this promising class of zeolites as a timely example, the first part of this thesis tackles the necessary steps to translate the preparation of hierarchical zeolites to the plant scale. The latter was achieved through a tight collaboration with Zeochem AG, an international manufacturer of molecular sieves and chromatography gels, who provided the existing infrastructure for the synthesis of conventional zeolites, and shared their expertise in the establishment of a versatile and cost-effective route for the large-scale manufacture, the selection of an appropriate catalyst formulation, and the shaping of powders with additives into suitable geometries. The resulting hierarchical zeolites are shown to preserve their catalytic benefits in technical form, confirming

the attainment of a novel product with clear prospects for its commercialization.

To optimize the assembly and function of technical catalysts in industrial reactors, it is essential to identify advanced strategies sensitive to their structural complexity. For the first time, this thesis presents an integrated approach combining dedicated specimen preparation with state-of-the-art optical, X-ray, and electron-based microscopic and tomographic techniques to visualize the hierarchical ZSM-5 extrudates and granules prepared at industrial scale, displaying a trimodal network of micro-, meso-, and macropores, from macro to nano length scales.

With the ultimate aim of developing fundamental principles in the scale-up of novel catalysts, an important transition is the ability to prepare, characterize, and evaluate zeolites in technical form directly at the laboratory scale, allowing the faster screening of potential zeolite-additive formulations in smaller quantities. Through the systematic comparison of physical, extruded, and milled admixtures of ZSM-5 zeolites with common silica, alumina, or clay binders, this thesis elucidates the cause and magnitude of property variations induced by shaping, which are currently difficult to predict, and relates them to the corresponding catalytic impacts in the conversion of methanol to valuable hydrocarbons. The results presented show that the combined chemical and physical effects of inexpensive binders can bring vast performance benefits in terms of lifetime extensions and enhancements in light olefin selectivity, matching or even exceeding those attained by explicit alterations of the active phase, such as the introduction of intracrystalline mesopores in zeolite crystals. Attapulgite clay is shown to uniquely promote the longevity and light-olefin selectivity of the zeolite, which is correlated with the reversible neutralization of the Brønsted acid sites by mobile Mg^{2+} species. Moreover, the scope of complementary techniques is exploited to pave a more rational way towards understanding physical and chemical zeolite-binder interactions, to elucidate their origin and determine their location, which has not been addressed prior to this thesis.

Sparked by the vast potential of additives to optimize specific properties of zeolite catalysts, this thesis explores novel strategies to complement the thermophysical characteristics of these multicomponent materials, which are typically insulating in nature. Using a transient hot-plate technique to decouple the distinct contributions of porosity, hydration, and temperature, the

impact of metallic, ceramic, and carbonaceous phases on the thermal conductivity of shaped zeolites at the body and packed-bed scales is quantified. The decisive role of the additive morphology, which largely dominates over the intrinsic conductivity, is corroborated through the 3D reconstruction of data acquired by focused ion beam-scanning electron microscopy and X-ray microtomography coupled with in situ thermographic studies. In particular, the order of magnitude improvement in the thermal conductivity evidenced on application of graphite sheets is found to stem from the extended paths of low thermal resistance created in the catalyst ensemble.

Overall, this thesis demonstrates that a rational correlation of the knowledge of the spatial organization gained by visualization, the physico-chemical properties, and the performance together with the formulation and structuring protocol will clearly facilitate the understanding and optimization of superior catalytic technologies. The identification of synthesis-property-function relationships will enable a more effective utilization of the mass- and heat-transfer properties of technical catalysts to enhance their performance in diverse catalytic applications. The results also expose the current challenges in the field, in particular, the vast complexity that technical zeolite catalysts still represent, despite the insights gained to date.

Zusammenfassung

Fortschritt in der heterogenen Katalyse war, ist und wird auch in Zukunft immer von gesellschaftlichen Bedürfnissen (*e.g.*, Umwelt, Energie, Chemikalien, Kraftstoffe) motiviert, mit dem Ziel die Prozesseffizienz im technischen Maßstab zu verbessern. Technische Katalysatoren sind üblicherweise komplexe Körper, bestehend aus aktiven Phasen sowie zahlreichen Zusatzstoffen, um eine bestimmte Funktion zu optimieren. Diese sind je nach kommerzieller Anwendung, zwischen zehn Mikrometern und mehreren Zentimetern groß. Sie können sich in ihrer Zusammensetzung, Struktur, Porosität, und Leistung stark von Forschungskatalysatoren, *i.e.*, laborentwickelte Materialien unterscheiden. Letztere bestehen aus einer einzelnen Bulk- oder getragenen Aktivphase in Pulverform, und bilden den überwiegenden Schwerpunkt der akademischen Forschung. Trotz der enormen Relevanz gibt es jedoch keine klaren Grundleitlinien für ihre technische Herstellung, was eine maßstabsgerechte Vorbereitung, Formulierung und Strukturierung umfasst, und die häufig der Geheimhaltung unterliegt.

In der Zeolithkatalyse, die schätzungsweise 10–13% des weltweiten Marktwertes von Katalysatoren ausmacht, wurde nur eine Handvoll der bestehenden 218 Rahmentypen kommerzialisiert. Es wird angenommen, dass ein verbessertes Verständnis des Scale-up-Prozesses die Übertragung von neuartigen Zeolithmaterialien in einen industriellen Kontext vereinfachen kann. Die Entwicklungen im Bereich der Synthese von Zeolithkatalysatoren haben sich zunehmend auf die Herstellung von hierarchisch strukturierten Materialien ausgerichtet, in denen ein Hilfsnetzwerk von Meso- und Makroporen die Zugänglichkeit zu den aktiven Zentren erhöht, was zu einer verbesserten katalytischen Leistung im Labormaßstab führt. Anhand dieser vielversprechenden Klasse von Zeolithen, welche hier als zeitgemäßes Beispiel dient, befasst sich der erste Teil dieser Arbeit mit den notwendigen Schritten zur industriellen Herstellung von hierarchischen Zeolithen. Dieses wurde in enger Zusammenarbeit mit Zeochem AG, einem internationalen Hersteller von Molekularsieben und Chromatographiegelen, erreicht. Er stellte die bestehende Infrastruktur für die Synthese von herkömmlichen Zeolithen zur Verfügung, und

teilte seine Erfahrung in der Errichtung einer vielseitigen und kostengünstigen Methode zur industriellen Fertigung, sowie der Auswahl einer geeigneten Formulierung der Katalysatoren, sowie des Formens von Pulvern mit Additiven in geeignete Geometrien. Die so entstandenen hierarchischen Zeolithe behalten ihre katalytischen Vorteile in technischer Form, wodurch ein neues Produkt mit klaren Perspektiven für seine Kommerzialisierung gewonnen werden kann.

Um die Anfertigung und die Funktion von technischen Katalysatoren in industriellen Reaktoren zu optimieren, ist es wichtig, strukturempfindliche Strategien zu identifizieren. Diese Dissertation präsentiert zum ersten Mal einen integrierten Ansatz, um die hierarchischen ZSM-5 Extrudate und Granulate, die in der Industrie hergestellt werden und ein trimodales Netzwerk von Mikro-, Meso-, und Makroporen besitzen, von der Makro- bis zur Nanolängenskala zu visualisieren. Dafür benötigt es eine Kombination aus aufwendiger Probenvorbereitung und hochmodernen optischen, Röntgenbasierten, sowie elektronenbasierten mikroskopischen und tomographischen Techniken.

Um die Grundprinzipien des Scale-up von neuen Katalysatoren weiterzuentwickeln, ist es wichtig, Zeolithe in technischer Form direkt im Labor herzustellen, sie zu charakterisieren und zu bewerten, um eine schnellere Selektion von potentiellen Zeolith-Additiv-Formulierungen in kleineren Mengen zu ermöglichen. Diese These verdeutlicht die Ursache und das Ausmaß der Eigenschaftsveränderungen, die durch das Strukturieren herbeigeführt werden, aber derzeit nur schwer vorherzusagen sind. Diese werden dann mit den entsprechenden katalytischen Auswirkungen in der Umwandlung von Methanol zu wertvollen Kohlenwasserstoffen in Beziehung gesetzt. Dabei werden physische, extrudierte und in der Kugelmühle bearbeitete Mischungen von ZSM-5 Zeolithen mit handelsüblicher Kieselerde, Aluminiumoxid, oder Tonerde als Bindemittel, systematisch verglichen. Die vorgestellten Ergebnisse zeigen, dass die gemeinsamen chemischen und physikalischen Effekte von kostengünstigen Bindemitteln, große Leistungsvorteile hinsichtlich der Laufzeitverlängerung und Verbesserungen von Olefinselektivität bringen können, die denjenigen gleich kommen oder diese sogar übersteigen, welche durch explizite Veränderung der aktiven Phase, wie zum Beispiel der Einführung von intrakristallinen Mesoporen in Zeolithkristalle, erreicht werden können. Die einzigartige Rolle von Attapulgit in der Förderung der Langlebigkeit und Olefinselektivität des

Zeolithkatalysators hängt mit der reversiblen Neutralisierung von Brønstedsäurezentren durch mobile Mg^{2+} Spezies zusammen. Zudem wird der Umfang der komplementären Techniken ausgenutzt, um einen rationelleren Weg zum Verständnis physikalischer und chemischer Zeolith-Bindemittel-Wechselwirkungen zu ebnen, ihren Ursprung zu erklären und ihren Standort festzustellen, was vor dieser Arbeit noch nicht untersucht wurde.

Ausgelöst durch das enorme Potential von Zusatzstoffen, um bestimmte Eigenschaften von Zeolithkatalysatoren zu optimieren, erforscht diese These neue Strategien, um die thermophysikalischen Eigenschaften dieser Mehrkomponentenmaterialien, die typischerweise isolierend wirken, zu steigern. Unter Verwendung einer instationären Heizplattentechnik, die die einzelnen Beiträge der Porosität, Hydratation und der Temperatur entkoppelt, wird die Wirkung von metallischen, keramischen und kohlenstoffhaltigen Phasen auf die Wärmeleitfähigkeit von geformten Zeolithen entweder als einzelner technischer Körper oder als Schüttung quantifiziert. Die entscheidende Rolle der Morphologie der Additive, die erheblich über deren Eigenleitfähigkeit dominiert, wird durch die 3D-Rekonstruktion von fokussierten Ionenstrahl-Rasterelektronenmikroskopie, Röntgenmikrotomografie und in situ Thermographiestudien bestätigt. Insbesondere die zehnfache Verbesserung der Wärmeleitfähigkeit von Zeolithen unter Beimischung von Graphit ergibt sich aus den ausgedehnten Pfaden des geringen Wärmewiderstands im Katalysatorenensemble.

Diese Dissertation zeigt, dass eine rationale Korrelation der Kenntnisse der räumlichen Organisation, gewonnen durch Visualisierungsmethoden, der physikalisch-chemischen Eigenschaften, und der Leistung zusammen mit der Formulierung und dem Strukturierungsprotokoll, das Verständnis und die Optimierung von überlegenen Katalysatorentechnologien deutlich erleichtern kann. Die Identifizierung von Synthese-Eigenschafts-Funktions-Beziehungen soll eine effektivere Nutzung der Stoff- und Wärmeaustauscheigenschaften von technischen Katalysatoren ermöglichen, um ihre Leistung in diversen katalytischen Anwendungen zu verbessern. Die Ergebnisse legen ebenfalls die aktuellen Herausforderungen in diesem Forschungsgebiet dar, insbesondere die enorme Komplexität, die technische Zeolithkatalysatoren immer noch ausmachen, trotz der bis dato gewonnenen Erkenntnisse.

Chapter 1

Introduction

1.1. Background

Catalysis is a discipline whose technological application preceded the construction of its scientific foundations. Nowadays its importance, in terms of both economy and the impact on quality of life, is unequivocal. Thought to contribute to greater than 35% of the global gross domestic product, it is estimated that around 90% of all chemical processes employ underlying catalytic steps.^[1,2] The catalyst market, which was valued at 29.5 billion USD in 2010,^[3] is expected to grow by an average of 6.6% in the energy and environmental sectors by 2015.^[4] Furthermore, catalysis is viewed as a key enabling technology, identified as one of the twelve principles of green chemistry.^[5]

With acquired mastery of the field, the design of heterogeneous catalysts has moved away from its purely empirical origins. Outstanding advancements have been witnessed, driven by mounting societal demands and enabled by the development of rational synthesis routes, powerful space- and time-resolved characterization techniques, and tools to assess the performance under relevant process conditions in an accelerated manner.^[6-15] The improved control and understanding has led to overwhelming wave of new catalytic materials in the scientific literature.^[16-19]

In relation to design, it is pertinent to distinguish between research and technical catalysts (Figure 1.1). Research catalysts normally comprise a single bulk or supported active phase in powder form. They constitute the library of materials consulted during the early stages of any catalyst development program and have been most significantly broadened by the mentioned progress. Following a traditional approach, the number of potential candidate materials is reduced during primary and secondary screening to a handful of potential leads. Technical catalysts should not only faithfully reproduce the performance of laboratory preparations, but must also have the required mechanical strength and chemical stability to ensure smooth

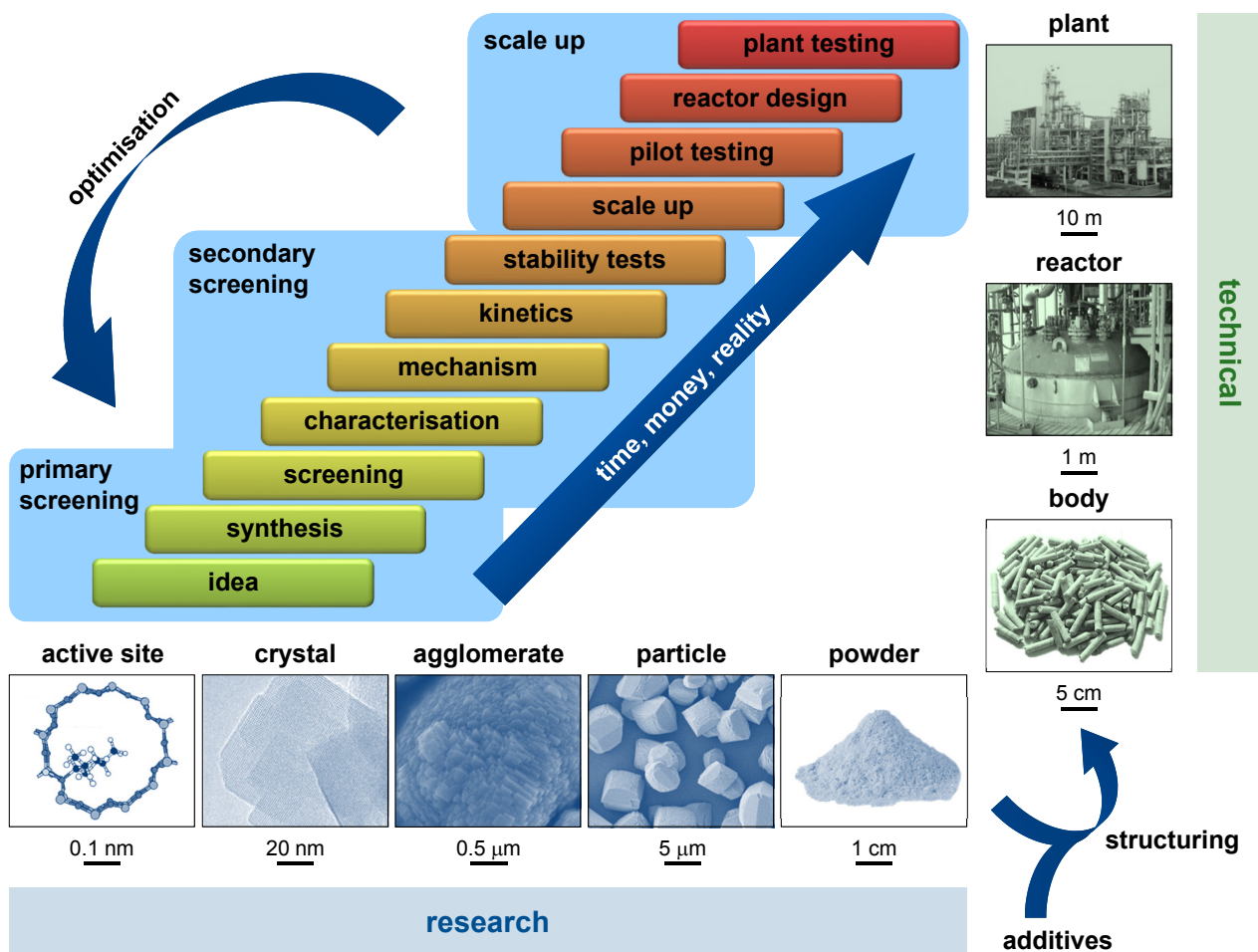


Figure 1.1. Typical sequence of interactive tasks in a catalyst development program. A key step is the translation of a promising research catalyst into a technical analogue involving the extrapolation of laboratory recipes to an industrial scale and the structuring of powders with additives into mm-sized bodies. Successfully implemented technologies are those which deliver recognizable performance benefits upon bridging the multiple length scales from the active site to the chemical plant.

operation and long lifetime when implemented in industrial reactors. Turning a promising candidate into an industrial catalyst implies (i) the adaption of laboratory protocols for its multi-ton manufacture, (ii) the selection of appropriate catalyst formulations (*i.e.*, type and proportion of component phases), and (iii) the shaping of powders into macroscopic forms. The resulting technical catalysts are multicomponent bodies ranging from hundreds of micrometers to several centimeters in dimensions.^[20–31] On average the time from idea to commercialization is in the order of a decade, with an approximately equal split between laboratory evaluation and scale-up.

Scale-up is a major hurdle in the successful implementation of new catalytic technologies. Besides the active phase, which is primary to the activity, the catalyst formulation

generally includes multiple additives to complement physical (mass or heat transfer), chemical (functionality), or mechanical (strength and attrition resistance) attributes (Figure 1.2a). Because of this, technical catalysts differ strongly in composition, structure, and porosity from research catalysts, and often exhibit a very different performance for better or for worse. A purely commercial aspect also acts in technical catalyst development: only those satisfying rigorous cost, performance, and safety constraints prevail. Implemented catalysts must be reproducibly manufactured, practical to handle and recover, avoid excessive pressure drops in industrial reactors, provide high mechanical, chemical, and thermal stability during long-term operation, and above all deliver recognizable performance benefits within an acceptable expenditure.^[20–31]

Although catalysis is now an intensively studied discipline in the open literature, knowledge about catalyst scale-up, the success of which ultimately determines the overall viability of a process, is scarce. Several aspects could contribute to the apparent disinterest in this topic. From an industrial perspective, recipes for the manufacture of heterogeneous catalysts are fiercely guarded.^[32] Undisclosed for proprietary reasons or described in the patent literature in the broadest sense, without detailed justification of the claims made, this secrecy provides a way for a company to maintain a competitive edge. A high degree of empiricism persists, which is accentuated by the fact that under time and cost pressures, catalyst manufacturers often avoid scale-up challenges altogether by opting for the use of commercially-available shaped catalyst carriers. Although these come with a wide range of tailored properties, compromises with respect to performance are inevitable.

On the other hand, the unduly low academic effort to understand the preparation of technical catalysts could be attributed to a number of factors, such as the absence of incentives and know-how due to a lack of awareness of industrial practices and the challenges faced; the practical needs to be able to safely prepare and handle larger material quantities and the availability of specific infrastructure including large machinery; and the complexity of understanding the interplay between interacting phases when shaped into workable geometries, which presents a huge intellectual challenge. In connection with the latter, the range of required expertise, combining different facets of chemistry, materials science, chemical and mechanical

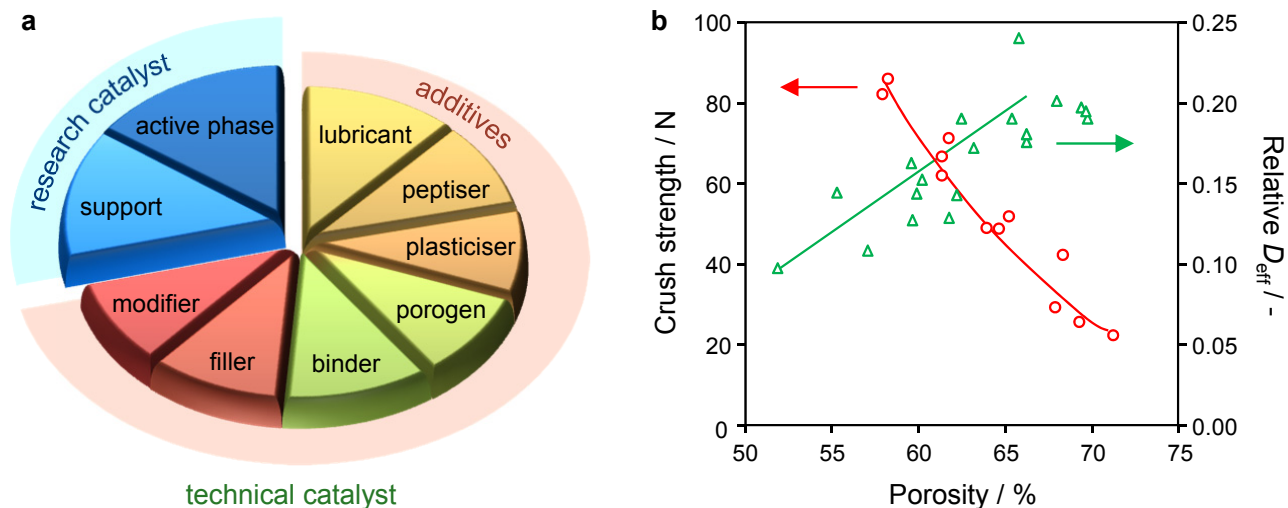


Figure 1.2. (a) Commonly applied components in catalyst formulation. Additives incorporated to facilitate the shaping or to enhance the properties of technical catalysts change the composition, structure, porosity, and performance with respect to research catalysts.^[20–31] (b) Compromise between pellet porosity, effective diffusivity, and crush strength observed in the preparation of $\text{Co}_2\text{AlO}_4/\text{CeO}_2$ catalysts with varying porogen content. Adapted from ref. [37].

engineering, calls for interdisciplinary teams. One can easily imagine that, in contrast to industry, academic groups increasingly focused on specialized topics cannot embrace the whole reach.

There is an urgent need for increased academic awareness of catalyst scale-up to fully comprehend catalytic processes from synthesis to mechanism. Current design strategies are often polarized towards the establishment of structure-property-function relationships for research catalysts. Advanced studies of the latter have been instrumental in attaining a molecular-level understanding of the active phase.^[33–36] However, since these works neglect a significant proportion of the ingredients of technical catalysts (Figure 1.2a), the extent to which the mechanistic information derived is representative of the actual performance data obtained in practice remains questionable. The only way to design improved catalysts is through understanding real catalytic systems, site engineering, crystal/particle engineering, and reactor engineering (Figure 1.1), and not oversimplified analogues.

1.2. Basics of Catalyst Formulation and Structuring

Towards the end of the last century making a catalyst moved away from being analogized with ‘black magic’ to being constructed as a scientific discipline. A facilitator in this shift was the

Table 1.1. Overview of the types, functions, and materials applied as additives in technical catalyst manufacture.

Additive	Function	Applicable materials	Prominent examples
Binder	Increase mechanical strength upon hardening of technical body	Inorganic oxide with refractory properties	Alumina, aluminum phosphate, silica, silica-alumina, natural clays (attapulgite, bentonite, kaolin, montmorillonite, sepiolite), titania, zirconia
Filler	Dilute active phase to optimize content in technical body	Low cost inorganic oxide with refractory properties	Natural clays (<i>e.g.</i> , kaolin), alumina
Lubricant	Reduce friction during mixing and shaping operations	Oil or other viscous liquid	Ethylene glycol, glycerin, graphite, mineral oil, propylene glycol, aluminum stearate
Modifier	Enhance performance of a technical catalyst	Promoter, selective poison, co-catalyst, coke or metal traps, passivators, thermal conductor	Metal or metal oxide precursor, clay, zeolite, ceramic (<i>e.g.</i> , SiC), carbonaceous materials (<i>e.g.</i> , graphite)
Peptizer	Disperse particles to improve feed homogeneity prior to/during shaping	Commonly a mineral or organic acid, but can also be a base	Acetic, citric, formic, hydrochloric, nitric or sulphuric, phosphoric acid
Plastiziser	Decrease viscosity of pre-mixtures to facilitate processing	Material dependent; typically containing polar and non-polar functionality	Hydroxyethyl cellulose, polyethylene glycol, starch, sugars, water
Porogen	Increase interparticle porosity in technical body	Cheap material which is removed, typically by thermal decomposition during hardening	Carbon black, flax, sawdust, starches of different size (corn, rice, potato)

deconstruction of catalyst preparation into a series of elementary steps, which were broadly classified according to the chemical and physical transformations implied, and the related methodology and operation variables.^[20-25] An essential task in their commercial manufacture is a unit operation known as ‘shaping’ in which powders are structured using a specific method into macroscopic bodies (Figure 1.1). Serving as a natural divide, a distinction can be made between treatments applied before and after shaping to modify the properties of the component powders and agglomerated bodies, respectively.

Industrial catalysts come in a wide variety of compositions and shapes. Formulating and structuring a technical catalyst entails the selection of component materials and how they are introduced, and the shaping method used. Often this involves orchestrating the behavior of complex mixtures of chemically distinct materials, including the active phase, support, and multiple additives (Figure 1.2a). The latter are typically classified according to their primary function (Table 1.1) and serve to facilitate processing or to enhance the properties of the technical catalyst, sometimes playing more than one role. Additives can form a large fraction of the technical catalyst, with values of up to 90% not uncommon, as will be seen for the specific fluid catalytic cracking catalysts in Section 1.3.

Most industrial shaping methods, *i.e.*, spray drying to form micrometer-sized, pelletization, extrusion, or granulation to prepare millimeter-sized, or extrusion to yield centimeter-sized bodies, rely on powder agglomeration.^[23] Powders can be compacted dry, characteristic of pelletization, or in the presence of a liquid to enable processing as pastes or as slurries. The quality of the resulting technical body is governed by achieving a uniform densification of the components, which is strongly influenced by the particle attributes (*i.e.*, size and morphology, surface chemistry, and bulk density), the rheological behavior of the feed, and the action of additive phases. Three elements are common to all structuring processes: (i) powdered raw materials must initially be refined to form a well-defined feed, (ii) the pre-mixtures must be agglomerated into ‘green’ bodies of the required shape, and (iii) the shaped bodies must be hardened to satisfy the mechanical demands.

Feed optimization, including the pre-conditioning of component properties and their mixing, is essential to ensure the highest degree of success during shaping. Highly-aggregated,

irregularly-shaped, or heterogeneously-sized raw materials frequently need to be broken down by physical or chemical means. The simple action of intensive mixing, kneading, or wet milling to homogenize the phase distribution prior to shaping may suffice to reduce the particle size.^[38] Alternatively, the division of particle agglomerates into their primary subunits may require a chemical treatment such as peptization, in which the dispersion is controlled by altering the properties of the dispersing medium.^[39] Peptization is widely reported in the processing of boehmite and aluminas prior to shaping. The exact processes involved, *i.e.*, porosity and particle size evolution, still remain the subject of considerable misunderstanding.^[39–41] Shaping methods can also be applied in series to improve feed homogenization, one of the most common examples being the use of spray drying to attain flowable powders prior to pelleting.^[37] Throughout all of these steps, the sequence of component addition should reflect the stability of each material under the conditions applied. Additives such as lubricants and plasticizers can be exploited to minimize the risk of structural damage during mechanical processing. A working knowledge of the component properties such as how the surface chemistry varies as a function of the pH and/or the concentration of adsorbed ions, and how they impact the water content and rheological properties of the pastes and slurries formed is highly beneficial.^[41–43]

To transform pre-mixtures into green bodies, particles need to be brought into intimate contact. How this is accomplished depends on the shaping method, *i.e.*, compacting a powder, entrapment in a shrinking slurry droplet, forcing a paste through a die, *etc.* Similar types of interparticle interactions (*e.g.*, electrostatic, hydrophobic, liquid bridges, van der Waals), the extent of which depends on the materials present and the interfacial contact area, are reported to occur in all cases.^[44,45] Stronger adhesion is typically favored during wet processing, through capillary forces due to the formation of liquid bridges between particles. However, in the latter case the risk of compositional changes is elevated as the liquid may solubilize certain species, thereby increasing their mobility and the probability of redistribution. The application of organic additives to act as temporary binding aids and stabilize the green body prior to hardening is frequently reported.^[46,47]

After shaping, strong interparticle interactions must be developed to improve the mechanical stability, which for most catalysts is achieved by thermal treatment. Many of

the underlying mechanistic principles describing the changes in chemical bonding, *i.e.*, by condensation of terminal hydroxyl groups on neighboring particles to form oxide or hydroxide bridges or by more extensive solid-state sintering, stem from ceramic and powder metallurgy.^[44] Several processes may occur simultaneously with differing rates, depending on the catalyst formulation, but as yet an atomic level understanding of the changes at the interfaces, in particular in relation to the possible implications in catalysis, has not been gathered. It is not uncommon for one or more inorganic phase to undergo an irreversible structural transformation, often as a result of decomposition (such as dehydration) during thermal treatment. Extensive interactions are favored by an intimate contact between the components, which is facilitated through the application of colloidal-sized particles such as those attainable by sol-gel type routes.^[48,49] For materials which exhibit poor self-binding properties (*e.g.*, zeolites), the inclusion of binders is indispensable to attain durable bodies.

Binders deserve close consideration as they are ubiquitously used and can form, along with fillers, large portions of the technical catalyst. The distinction between binders and fillers, the latter introduced to moderate the activity or reduce the catalyst cost, is often not straightforward. In fact, binders are also considered as fillers if introduced in quantities larger than those required for the purposes of mechanical strength. Materials of similar types are used for both purposes, of which aluminas, silicas, natural clay-derived materials and mixtures thereof are pervasive due to their refractory properties, high earth abundance, non-toxicity, and relative low cost. Organic binders (*e.g.*, polymers) are less common in catalysis due to their lower threshold to withstand high operating and regeneration temperatures.^[50] While naturally-sourced materials are typically cheaper, synthetic analogues may be preferred due to their higher purity and the improved control over the particle attributes. Ideally they can enhance the catalytic performance, *e.g.*, by contributing to a well-defined internal pore structure, exhibiting co-catalytic activity, improving the thermal stability, protecting the catalytic phase from impurities, *etc.* It is noteworthy that the materials applied are also widely used catalyst supports.

Organic additives are typically removed under the conditions of thermal treatment, generating pores within the structure.^[46,47] Porogens can be specifically added to increase the

porosity, which can be moderated through the appropriate choice and amount of the porogen applied, directly enhancing the mass transfer within shaped catalysts. However, improvements in the effective diffusion often suffer the penalty of a reduced mechanical strength for which a compromise must be found (Figure 1.2b).^[37]

Additional treatments, such as impregnation, reduction, wash-coating, ion exchange, or steaming, are frequently exploited to adjust the properties of technical bodies. Modifications applied after shaping have the advantage of facilitated handling and recovery on a large scale with respect to powders. The possibility of incorporating components at this point offers greater flexibility for materials which may otherwise be unstable under the conditions of previous shaping steps, *e.g.*, metals prone to sintering during hardening.^[51–53] Caution is required as the treatment of composite macroscopic bodies can have very different results from those observed when applied to research catalysts. During metal deposition, for example, it is necessary to ensure that any additives present do not detrimentally impact the dispersion. Impairment of the mechanical integrity of the technical form should obviously be avoided.

1.3. Understanding Scale-up of Zeolite Catalysts

Zeolite catalysis, which owing to their unique properties blossomed into a global enterprise during the second half of the 20th century,^[54–57] provides an excellent playground to study the implications of scale-up. To the best of our knowledge virtually all current industrial applications require some form of structuring with inorganic binders, which can form a major part (*i.e.*, 90%) of the final catalyst. Of the 200 distinct crystalline framework types identified to date, only around 10% have so far become commercially viable. It is expected that a better understanding of the scale-up will prove invaluable in enabling the technical application of more of these materials.^[58–60] The far from inert nature of binders in many zeolite systems was highlighted by a recent perspective.^[61] In addition to their primary role in improving the mechanical stability, binders can impact the performance by other physical and chemical means.^[61]

1.3.1. A Classic Case: FCC Catalysts

The contrast between a research and a technical catalyst can be likened to the difference between a solo instrumentalist and an orchestra. As opposed to the pure sound of a single instrument, in the latter case an ensemble of musicians in woodwind, strings, percussion, or brass sections, have to be harmonized to ensure a good performance, which is akin to coordinating the distinct functions of the multiple constituent phases in industrial catalysts. This is well illustrated by the case of FCC catalysts, in which the active faujasite-type Y zeolite (*i.e.*, the research catalyst) may comprise as little as 10% by weight.^[61–68] Catalyst manufacturers are acutely conscious of the fact that developing an FCC catalyst is more than only a matter of considering the active phase.^[64–68] The additional components, present either in the attrition resistant amorphous matrix, which binds the microspheroidal zeolite granules (60–200 μm) or as distinct solid or liquid additives, tackle different activity, selectivity, stability, and cost-related effects (Figure 1.3a). The resulting complexity provides infinite possibilities of innovating the formulation, *e.g.*, to target an increased feed flexibility or a particular product slate, which accounts for the continued growth in patent publications reporting new or improved catalyst preparations (Figure 1.3b), despite the fact that FCC is viewed as a mature process.^[68]

Since their introduction in the 1960s, Y zeolites, typically applied in ultrastabilized (USY) or rare earth-exchanged forms (REY), have governed the cracking activity and selectivity in FCC catalysts, and their synthesis and post-synthetic modification to modify the acidity and improve the (hydro-)thermal stability of the framework have been widely studied.^[65,68–70] While the dominant role of the active zeolite phase remains to be surpassed, the overall formulation has evolved significantly according to changes in feedstock composition, unit design, market prices, environmental legislation, and desired product quality.^[65–70]

Comprising the major fraction of FCC catalysts, the composition of the matrix is a crucial aspect in determining the performance. The incorporation of a wide range of chemically-distinct materials has been investigated to optimize specific properties, in addition to its binding role.^[64–72] Of these a synthetic silica, alumina, or silica-alumina colloidal gel and/or larger particles derived from natural clays (typically kaolin or montmorillonite) generally form the main part.^[64–67] Acidic aluminas or silica-aluminas are exploited to pre-crack bulky hydrocarbon

substrates,^[70,71] whereas silicas are preferred if an inert diffusion medium is required to dilute the zeolite activity or to avoid unselective cracking.^[73,74] Significant attention has been focused on optimizing the matrix porosity to ensure the effective transport of reactants and products to and from the active zeolite phase.^[75–78] Macroporosity can be increased by applying higher contents of kaolin^[77] or by controlling the synthesis conditions of the synthetic component, *e.g.*, by the addition of porogens or pH modifiers.

In the heat-balanced FCC unit, coke deposition must be carefully moderated to ensure sufficient heat generation during oxidative regeneration to catalyze the endothermic cracking reaction.^[63,66] Since coke formation and distribution is highly interrelated with the properties of the matrix, the composition of the latter requires careful adjustment to synchronize the rate of deactivation with that of the zeolite phase.^[66,79] Herein, the nature of the hydrocarbon feed, the process parameters, and the targeted product distribution must be considered to ensure an adequate lifetime and minimize unselective bottom cracking.

A landmark change in the formulation of FCC catalysts followed the realization that the addition of an MFI-type zeolite (ZSM-5) could improve the octane rating of primary gasoline products.^[80,81] The technical hurdles faced by Mobil when ZSM-5 was first trialed in FCC catalysts during the course of its commercialization in the 1980s nicely illustrate the types of challenges which can arise during scale-up.^[80] The synthesis of ZSM-5, which requires a template, had to be brought down in price. Additionally, the higher stability of the ZSM-5

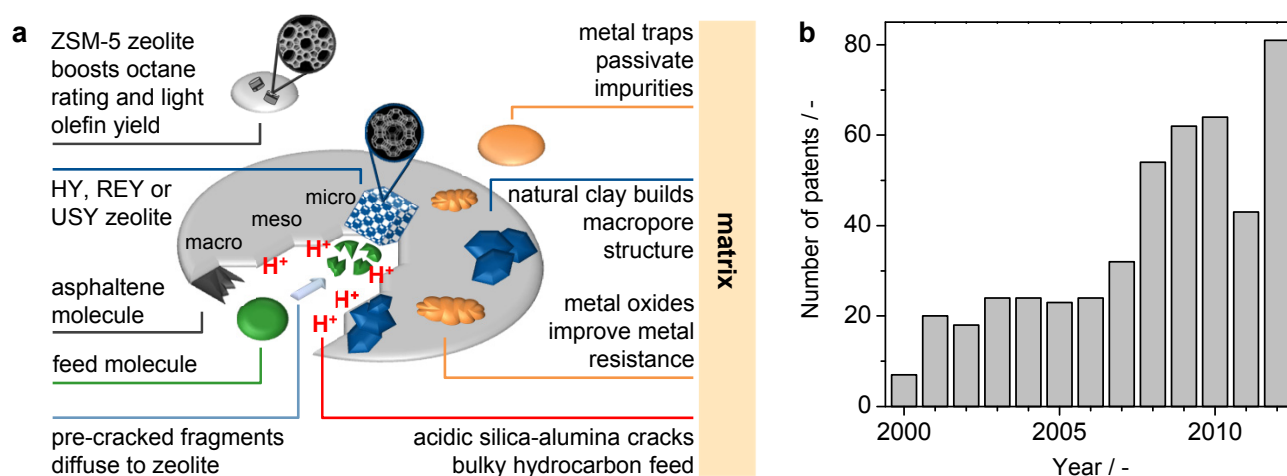


Figure 1.3. (a) Schematic diagram of the composition of a spray-dried FCC catalyst microsphere, each component accomplishing a defined function. Adapted from ref. [62]. (b) Annual number of patents reporting a new and/or improved preparation of an FCC catalyst this millennium.

framework resulted in a slower deactivation in the reactor compared with the Y zeolites used, leading to unwanted selectivity variations. Although initial attempts tried to incorporate the two zeolites into single agglomerates, nowadays it is customary to shape the ZSM-5 as separate particles, which are applied as-needed in order to maintain a constant activity relationship between the two zeolites. With an increased demand for light olefins, especially propene, focus on the usage of ZSM-5 additives has shifted toward the production of propene at the expense of gasoline.^[82]

Adaptions in the formulation have also been motivated by a need for improved metal tolerance.^[83-86] Contaminant metals (*e.g.*, Ni, V, Fe, Na), prevalent in residual oils, are continuously deposited in the catalyst during cracking and can result in undesired selectivity and irreversible deactivation. Strategies to minimize these adverse effects include the incorporation of metal traps and/or passivators to preferentially interact and/or react to sequestrate these species (*e.g.*, the addition of antimony, bismuth, or tin compounds to passivate nickel).^[83,84] Such additives can be incorporated directly into the zeolite Y containing microspheres or are separately blended into the FCC unit, providing greater flexibility to respond to performance needs without detriment to the function of the active phase. The impact of different metal species is also dependent on the matrix composition, opening possibilities to reduce their deleterious effects by strategic formulation.^[85,86] For example, oxidized vanadium species supported on alumina showed a much lower dehydrogenation and dehydrocyclization activity than when supported on silica.^[85] Acid-leached kaolin clay was also reported to exhibit improved resistance due to the ability of lattice vacancies to host metal impurities and form inert compounds such as nickel silicates.^[86]

Other well-established additives comprise (mixed) metal oxides such as magnesia-alumina or ceria-spinel introduced to moderate the emission of sulfur oxide and the incorporation of platinum- or palladium-based promoters to prevent uncontrolled CO oxidation in the dilute matrix phase by maximizing the oxidation of CO to CO₂ in the regenerator.^[65] Finally, it is noteworthy that the matrix composition is commonly linked with various important thermal effects in the composite FCC catalyst, for example, enhancing the (hydro-)thermal stability, modifying the heat capacity and/or the conductivity and related heat transfer, and acting as a

heat sink. While the basis of some of these effects, such as the reduced occurrence of hotspots upon dilution of the active phase or the retarded loss of zeolite crystallinity in the presence of certain additives, has been studied in depth (the origins of the improved hydrothermal stability in the presence of silica will be discussed in the next section), the cause of many others remains ambiguous, lacking direct evidence and without being specifically correlated with a given component.

1.3.2. Divergent Effects in Zeolite Catalysis

During the scale-up of research catalysts, the choice of formulation and structuring method can both positively or negatively affect the performance. The case of FCC catalysts highlighted several beneficial functions that additives can exert, among others by providing a co-catalytic function, diluting the activity, improving the mass transfer, controlling the rate of coking, and enhancing the thermal stability and the resistance to impurities of the active phase (Figure 1.4). Due to the overall success of this catalyst, the reported effects related to improvements in the function. However, since the changes in formulation have been predominantly grounded on trial and error approaches, the observations made have not all been rationalized. The lack of fundamental understanding, complicated by the fact that individual component phases can be associated with multiple and often interrelated roles which are challenging to decouple, make it difficult to assess the general applicability of the conclusions drawn to other processes. This section examines the broader implications of additives and shaping in acid-catalyzed zeolite applications.

A widely expected consequence upon agglomeration is a diminished activity due to the increased diffusion path to reach active sites, which can be buried deeply within the shaped body.^[87-89] However, the effects of additional resistances to transport with respect to research catalysts may not be immediately obvious as they are not always manifested in catalytic tests, depending on the conditions applied and the relative impacts of other (*e.g.*, compositional) changes.^[89] Appropriate design of porous properties is clearly essential to optimize zeolite utilization in diffusion-limited reactions in which the effects of longer trajectories will be more pronounced. The careful calibration of binder porosity to facilitate the transport of feed molecules, for example, was reportedly a critical factor in the development of competitive

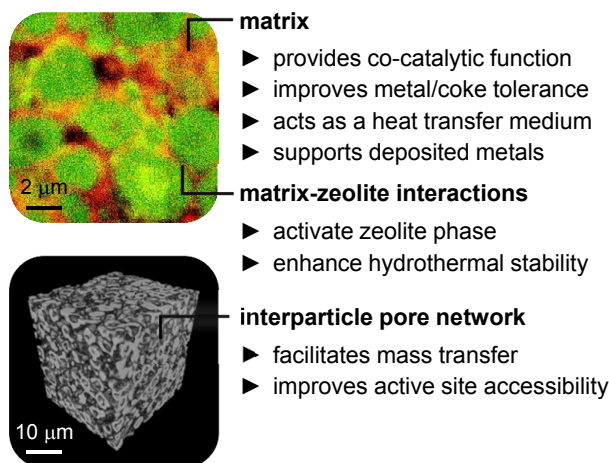


Figure 1.4. Energy-dispersive X-ray (EDX) spectroscopy map of Si (green) and Al (red) of a cross-section of a kaolin-bound hierarchical ZSM-5 extrudate (top), and an X-ray computed tomographic representation of the interparticle pore network (bottom) illustrate the distinct composition and porosity of the agglomerated catalyst. Benefits of optimizing the formulation of the matrix are summarized.

zeolite catalysts for slurry-phase applications.^[90] As is often the case where catalyst porosity is correlated with performance through improved mass transfer, direct evidence of the latter was not reported preventing the general rationalization of these effects.

In addition to increasing the diffusion path length, powder agglomeration also impacts the accessibility of active sites. Micropore blockage upon application of small inorganic sol binders, a phenomenon sometimes called ‘binder-blinding’, is commonly cited as a potential adverse impact of zeolite shaping.^[91,92] To date the extent and implications of the physical effects of zeolite-matrix interactions in catalysis are not well understood. The obstruction of micropores is frequently discounted on the basis of gas adsorption measurements. For many zeolites, however, a large fraction of pore mouths could be (partially) blocked without observing a significant drop in the micropore volume determined by N₂ or Ar adsorption. It is expected that kinetic measurements of the adsorption of hydrocarbon probe molecules will provide fundamental insight in this regard.

Another important distinction between powders and mm-sized catalyst bodies is the increased participation of the extracrystalline surface, which can alter the shape selective properties of a zeolite.^[93,94] Insightful work by researchers at Shell highlighted the impact of macroscopic structuring on the performance of ZSM-5 catalysts in the dehydration of

1-phenyl-ethanol to styrene, a reaction only catalyzed by the outer surface of the zeolite.^[93] By comparing the performance, they observed higher conversion and styrene selectivity over sieve fractions of the crushed catalyst than over the silica-bound ZSM-5 extrudates (Figure 1.5a). The distinct behavior was completely rationalized in terms of the strong internal diffusion limitations within the extruded catalyst, which reduced mass transport and favored consecutive oligomerization of the styrene intermediate.

The introduction of chemically distinct species in the matrix alters the type, amount, and distribution of active sites within the catalyst. Non-zeolitic components, such as binders, are typically less acidic than the zeolite of interest and, unless they react with the zeolite phase (*vide infra*), their presence results in an overall reduction in acidity. Such dilution of the zeolite activity is reportedly favorable in certain shape selective reactions, such as in the isomerization of *m*-xylene over silica-bound H-ZSM-5 catalysts,^[95] by reducing the occurrence of reactions at the external surface of the zeolite. Similar enhancements were achieved in the shape selective formation of *p*-diethylbenzene over alumina-bound ZSM-5 extrudates following silylation of the active matrix by chemical vapor deposition.^[95]

Interactions between multiple phases can result in the formation of sites and defects, which do not exist in the separate components, giving rise to a variety of distinct morphological, chemical, and electronic properties in real catalysts.^[96] Almost 30 years ago scientists at Mobil highlighted the possibility of modifying the composition of a zeolite through interaction with a binder during shaping. These findings referred to the migration of aluminum species from alumina (35–50 wt.% alpha-alumina monohydrate) into high silica ZSM-5 (Si/Al > 1600) upon wet extrusion. This type of reaction resulted in an improved ion exchange capacity and activity in acid-catalyzed reactions requiring strong zeolitic acidity (*i.e.*, *n*-hexane cracking, propene oligomerization, lube oil dewaxing, and methanol-to-olefins).^[97] Since the alumina binder was itself not active, the enhanced catalytic performance was attributed to the insertion of aluminum into the zeolite framework, which was confirmed by ²⁷Al MAS NMR and IR spectroscopy (Figure 1.5b). The migration of aluminum and subsequent insertion into the framework occurred preferentially in the presence of water, and could be considerably increased by steam treatment. Later work, investigating the stability of boron substituted ZSM-5, revealed that

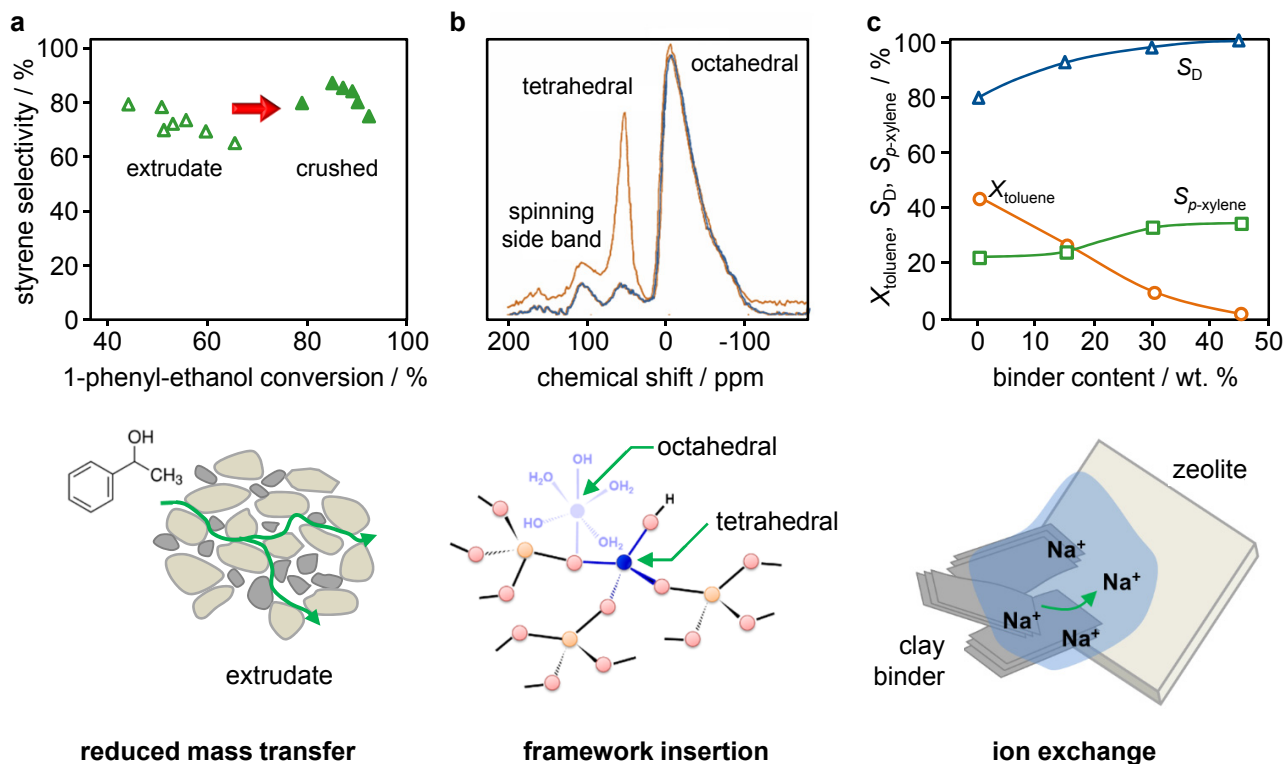


Figure 1.5. Three commonly cited impacts of structuring in zeolite catalysis: (a) the comparative conversion of 1-phenyl-ethanol and selectivity to styrene over silica-bound (60 wt.%) ZSM-5 extrudates and crushed analogues evidences a reduced mass transfer in technical form (reprinted from ref. [93], copyright 2001, with permission of Elsevier), (b) ^{27}Al MAS NMR spectra confirm the formation of tetrahedral aluminum species upon hydrothermal activation of high-silica ZSM-5 extruded with alumina (adapted from ref. [98]), (c) variation in the toluene conversion (X_{toluene}), selectivity to disproportionation (S_D) and p-xylene ($S_{p\text{-xylene}}$) over an H-ZSM-5 catalyst pelleted with different contents of Na-containing montmorillonite binder attributed to the neutralization of acid sites due to migration of sodium ions from the binder (reprinted from ref. [102], copyright 1991, with permission of Elsevier). The latter effect could be completely reversed by ion exchange.

the insertion of Al could be facilitated by the presence of a readily hydrolyzable heteroatom in the framework.^[98,99] As well as increasing the acidity, the presence of an alumina binder was also reported to stabilize colloidal zeolite beta nanocrystals, preventing dealumination during calcination.^[100] Binding with alumina does not always lead to activation. In contrast to the previous cases a partial neutralization of Brønsted sites was reported upon shaping ZSM-5 zeolites with a peptized boehmite.^[101]

Opposite to the case of alumina, a reduction in strong zeolitic acidity has been claimed upon application of low-acidity binders (*i.e.*, SiO_2 , TiO_2 , ZrO_2) to shape Al-rich zeolites (MFI, FAU, and BEA framework types), which was linked to dealumination of and/or the

insertion of silicon into the framework.^[103,104] Reaction of extraframework aluminum present in USY with a silica matrix under hydrothermal conditions reportedly led to the formation of catalytically active silica-alumina species at the matrix-zeolite interface.^[105] The replacement of aluminum expelled from the framework of RE-Y and offretite zeolites upon hydrothermal treatment with silicon from the matrix is believed to be responsible for the markedly improved stability, which is exploited in FCC catalysts.^[106] The migration and insertion of silicon into the zeolite framework was demonstrated by isotopic labeling.^[107] It is worth remarking that depending on the stability of the zeolite framework, demetallation can also result during hardening due to hydrothermal treatment, an effect which is more likely in the presence of additives which undergo dehydroxylation at high temperatures, such as kaolin, leading to elevated concentrations of water vapor.^[108]

Apart from framework modifications, the acidity of zeolites can also be altered by ion exchange with extraframework metals. This type of reaction has been frequently observed in relation to the application of clay binders containing exchangeable alkali metals and, in contrast to reductions in acidity due to demetallation, should be reversible.^[102,109,110] Extraframework modifications also have varying catalytic effects. Early work by Uguina *et al.*^[102] showed large differences in the performance of H-ZSM-5 catalysts in the disproportionation of toluene when bound with different contents of a sodium montmorillonite binder (Figure 1.5c). Greater acid site neutralization reduced the toluene conversion, but increased the disproportionation selectivity and shape selectivity to *p*-xylene. The properties of the pure zeolite phase were almost completely restored following reactivation of the catalyst by acid treatment. Despite numerous qualitative reports, zeolite-binder interactions remain far from being fully understood, and the relative importance of composition, treatment conditions has not been evaluated.

In summary, it is evident that the catalytic function of research and technical catalysts is not identical. The superimposed macrostructure contains chemically distinct phases which, if properly understood, can serve to complement and preserve the active ingredient.

1.4. Aim of the Thesis

The primary goal of this thesis is to gain an improved understanding of the implications of scale-up, including the industrial-scale manufacture, the choice of catalyst formulation, and structuring of powders into practically-relevant forms, in the development of improved zeolite technologies. With this in mind, the ultimate aim is to establish rational approaches to attain zeolites catalysts with enhanced functionality. In particular, this necessitates the critical assessment of the scalability and amenability of individual preparative steps, which become necessary at large-scale, as well as the identification of suitable advanced characterization tools to evaluate the additional complexity of technical catalysts. Attention will be placed on technically-preferred routes and commercially-available materials. The need to learn how to shape zeolite catalysts is necessary to elucidate the causes of property variations, and the related impact on the catalytic performance. While emphasizing the vast potential, improved rationalization and the earlier consideration of scale-up will enable the optimized development of novel zeolite catalysts, promoting the overall process sustainability.

1.5. Outline of the Thesis

The results of this thesis are presented in four chapters (**Chapter 2-5**), followed by the conclusions and outlook of the challenges ahead (**Chapter 6**). The research embodied in this thesis has been undertaken in the frame of a Swiss National Science Foundation grant titled "A fundamental approach to the scale-up of hierarchical zeolite catalysts" (project no. 200021-134572).

The scale-up of zeolite catalysts from powder to industrially-relevant shapes is widely neglected in fundamental research because of the added preparative and analytical complexity. **Chapter 2** addresses this lack of knowledge for the novel class of hierarchical ZSM-5 prepared by desilication, which to date has been confined to the laboratory scale undertaken in gram quantities under precisely controlled conditions. Aiming towards their practical realization, this is approached by the large-scale manufacture, assessing the amenability of existing protocols to scale-up, and shaping the resulting powders with binders into technical bodies. To gain fundamental knowledge on an otherwise heavily-dominated industrial operation, the

collaboration with Zeochem AG (Dr. N. Marti and Mr. G. Fenoggio) provides the necessary large-scale infrastructure, as well as expertise on structuring and understanding industrial needs/concerns. Extrapolation of the superior properties of hierarchical zeolites is proven by the remarkable similarity between industrial and laboratory scale results.

To better understand and optimize catalyst assembly and function in industrial reactors, advanced characterization tools are essential to build a detailed understanding of the structural organization of technical catalysts with respect to their powder analogues. While quantifying pore volumes and approximate pore sizes, standard gas sorption and porosimetry methods provide no information about the distribution of phases and related connectivity and topology of the inter- and intraparticle pore networks within the technical bodies. Thus, in **Chapter 3**, the scope of an arsenal of imaging techniques is assessed to provide complementary and corroborative insight into the complex spatial organization of the zeolite and binder particles and the corresponding different porosity length scales of the macroscopic bodies. Integrative visualization approaches, capable of connecting atomic-scale features of the active surface with the macroscopic properties of shaped catalysts, are discussed in relation to their advantages and practical limitations, in terms of intrinsic resolving power, the desired field of view, and the specific sample preparation. In addition, it is revealed for the first time that the catalytic benefits observed over hierarchical zeolites are preserved upon structuring in technical form.

To begin to rationalize the scale-up, an essential transition is the ability to prepare zeolites in technical form at the bench-scale. Based on the knowledge gained in **Chapter 2** and after suitably equipping the laboratory, the next step encompasses understanding the impact of binders and related structuring steps. **Chapter 4** elucidates the origin and extent of shaping-induced variations in the porosity and acidity of MFI catalysts, shaped with commercial silica, alumina, kaolin, and attapulgite clay binders, by systematic characterization of the individual components and of zeolite-binder admixtures prepared by physical mixing, extrusion, or ball milling. Subsequent evaluation in the conversion of methanol to olefins or gasoline-range hydrocarbons confirms the corresponding catalytic impacts. It is shown that binder effects can, without optimization, match or even exceed those of hierarchically structuring the porosity of the MFI crystals. Based on growing comprehension, methods to understand zeolite-binder

interactions are sought to identify the driving force (*e.g.*, solvent-assisted, mechanochemical, or solvo-/thermal) and extent (*e.g.*, acidity variations due to dealumination or ion exchange) as well as pinpointing their exact nature (*e.g.*, ion migration).

In comparison to mass transfer, for which the tailoring of porous materials has become customary practice (**Chapter 2-4**), strategies to enable improved thermal control by engineering the thermophysical properties of heterogeneous catalysts, which are mostly insulating in nature, have received much less attention. For example, the possibility to directly integrate highly thermally-conductive additives to enhance the heat transfer of technical zeolite catalysts remains limited. In **Chapter 5**, by using a transient hot-plate technique to decouple the distinct contributions of porosity, hydration, and temperature, the impact of metallic, ceramic, and carbonaceous phases on the thermal conductivity of shaped zeolites at the body and packed-bed scales is quantified. Visualization of the spatial integration of the additive through state-of-the-art visualization and in situ thermography demonstrates the decisive role of phase connectivity in the up to one-order-of-magnitude enhancements achieved in the thermal conductivity of zeolite catalyst bodies containing graphite sheets.

Chapter 6 summarizes the key results of the research introduced throughout this thesis, elaborates on fundamental strategies for the preparation, characterization, and evaluation of zeolite catalysts in shaped form with superior functionality, and identifies challenges ahead.

Each chapter of this thesis was written based on one publication and can be read independently. Accordingly, some overlap between the chapter introductions occurs.

Chapter 2

Scale-Up of Hierarchical ZSM-5 Zeolite into Technical Bodies

2.1. Introduction

In recent years, we have witnessed remarkable progress in the preparation, characterization, and application of hierarchical (mesoporous) zeolites.^[111–119] This wave of research originated because conventional (purely microporous) zeolites, despite having truly unique properties, underperform in many relevant reactions as a result of access and diffusion constraints. The introduction of auxiliary mesoporosity in zeolite crystals improves micropore accessibility and molecular transport.^[120–123] This enhances the activity, selectivity, and lifetime in a large number of heterogeneously-catalyzed reactions.^[124–128] Besides catalytic benefits, mesoporous zeolites exhibit improved performance in adsorption and ion exchange processes.^[129–131]

To date, the preparation of mesoporous zeolites has been confined to the laboratory scale, undertaken in gram quantities under precisely controllable conditions. Many of the routes developed are cost-prohibitive and currently unthinkable for large-scale production. Often, advanced porous materials do not make it to real life processes due to the difficulties encountered in extrapolating encouraging laboratory results to an industrial context. Therefore, to truly ascertain future perspectives for mesoporous zeolites as technical catalysts, it is of urgent necessity to demonstrate (i) their large-scale preparation and (ii) the preservation of their enhanced properties upon shaping into a workable form. The former need requires the identification of economically-viable preparation methods, whereas the latter constitutes the formation of a hierarchical material in the broadest dimension, integrating the micro-, meso-, and macroporosity levels in bound zeolite bodies. Herein, the first large-scale preparation of such hierarchically-structured zeolite catalysts is reported.

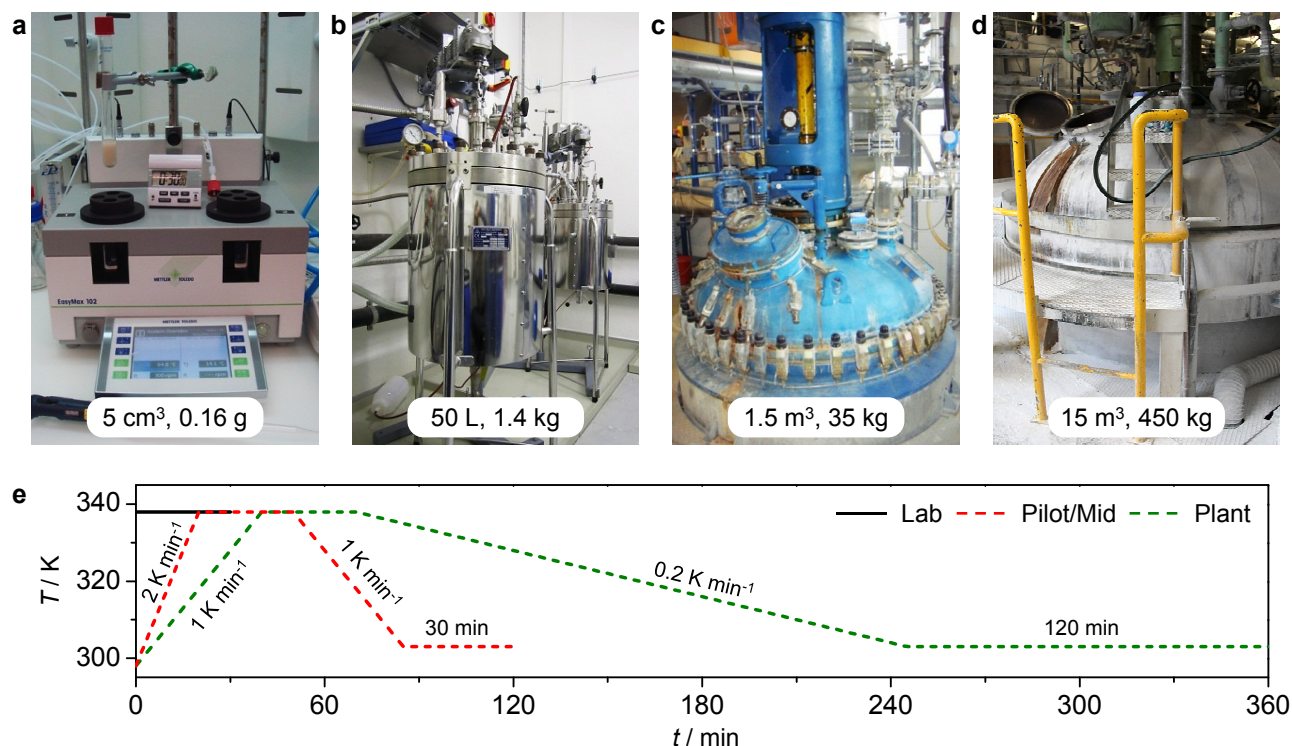


Figure 2.1. (a) Laboratory-, (b) mid-, (c) pilot-, and (d) plant-scale set-ups used for zeolite desilication. The volumes of alkaline solution and amounts of ZSM-5 treated are given. (e) Different temperature profiles during the treatments.

2.2. Experimental

2.2.1. Zeolite Synthesis and Desilication

A ZSM-5 zeolite with a nominal Si/Al ratio = 40 was synthesized hydrothermally at 1 MPa in an industrial 1.5 m³ autoclave. The reactor was charged stepwise with water, colloidal silica, sodium aluminate, tetrapropyl ammonium bromide (TPABr), and sodium hydroxide. The final gel, containing SiO₂ (82.23 mol), Al₂O₃ (1.00 mol), Na₂O (5.56 mol), TPABr (2.36 mol), and H₂O (1373.50 mol), was homogenized and heated to 423 K at 0.83 K min⁻¹. After 24 h, the reactor was cooled, and the zeolite was filtered (Fundabac, DrM), washed with distilled water, and dried at 333 K for 12 h in a Nabertherm furnace by using air convection. Template removal was achieved in the same furnace by calcination in flowing anhydrous air at 753 K for 3 h. The amount of conventional zeolite product (coded cz40) was 170 kg. Desilication of the calcined ZSM-5 in aqueous 0.2 M NaOH was performed in batch reactors with a volume of 5 cm³ (Easymax 102, Mettler Toledo), 50 L (Juchheim), and 1.5 m³ (homemade, Figure 2.1a-c, respectively). The liquid-to-solid ratio was fixed at 30 cm³ of alkaline solution per gram of

zeolite. On the laboratory scale, the zeolite was treated isothermally at 338 K for 30 min by using magnetic stirring, followed by quenching in ice water.^[132] Up-scale treatments were conducted under mechanical stirring and incorporated ramped heating and cooling (Figure 2.1). The alkaline-treated (mesoporous) zeolites were filtered, washed, converted to the ammonium form (0.1 M NH_4NO_3 , 6 h), and calcined at 823 K for 5 h (5 K min^{-1}). The resulting hierarchical ZSM-5 zeolites produced at laboratory, mid, and pilot scale were coded hz40_{lab} , hz40_{mid} , and $\text{hz40}_{\text{pilot}}$, respectively.

2.2.2. Industrial Manufacture of Hierarchical ZSM-5

A conventional ZSM-5 with a nominal Si/Al ratio = 50 (PZ-2/100, Zeochem, coded cz50) was desilicated (0.15 M NaOH) in a plant-scale reactor of 15 m^3 (Figure 2.1d) under mechanical stirring and following a specific temperature program (Figure 2.1e). The resulting alkaline-treated ZSM-5 (coded $\text{hz50}_{\text{plant}}$) was post-treated like its pilot-scale analogue, but using aqueous NH_4Cl for the ion exchange step. 450 kg of the final hierarchical zeolite powder was obtained.

2.2.3. Structuring into Technical Forms

The conventional and mesoporous zeolite powders in ammonium form were structured into mm-sized granules (intensive pan mixer, Eirich) or extrudates (single-screw extruder, Collins). Attapulgitic or kaolin clay, supplied by Zeochem AG, was used as the respective binder (zeolite:binder dry mass ratio of 4:1, accounting for the weight loss upon calcination to 873 K). First, the dry powder (2 kg), comprising the hierarchical ZSM-5 and binder, was intensively mixed to achieve phase homogenization. Wet granulation was undertaken by the stepwise addition of small quantities of distilled water (*ca.* 1.5 L in total) to the physical mixture of attapulgitic/ $\text{hz40}_{\text{pilot}}$, followed by continuous mixing. Extrusion was achieved by first forming a paste of desired consistency by addition of *ca.* 1 L of distilled water to the kaolin-hierarchical zeolite admix, followed by feeding the paste into the extruder using a die with circular holes of 4 mm diameter. The conventional zeolite powder, serving as a reference material, was structured in a similar way, but utilizing *ca.* 30% less water in total. Finally, the bodies were dried (393 K, 12 h) and then calcined (873 K, 3 h, 2 K min^{-1}) in a Nabertherm furnace under air flow. All samples were characterized in the protonic form resulting subsequent to calcination.

2.2.4. Characterization Techniques

The Si and Al concentrations in the solids were determined by atomic absorption spectroscopy (AAS) by using a Varian SpectrAA 220 FS instrument, or by X-ray fluorescence spectrometry (XRF) with an Orbis Micro XRF analyzer (EDAX) operated with a Rh source at 30 kV. N₂ adsorption was measured at 77 K with a Quantachrome Quadrasorb-SI gas adsorption analyzer. Prior to the measurement, the samples were evacuated at 573 K for 12 h. Mercury intrusion porosimetry experiments of the granules were performed by using a Micromeritics Autopore IV 9510, which operated in the pressure range from vacuum to 400 MPa. Degassing was undertaken in situ. Temperature-programmed desorption of ammonia (NH₃-TPD) was carried out in a Thermo TPDRO 1100 unit equipped with a thermal conductivity detector. The sample (0.100 g) was pre-treated at 823 K in He (20 cm³ min⁻¹) for 2 h, followed by three consecutive cycles of NH₃ adsorption (10% in 20 cm³ min⁻¹ He, 473 K, 30 min) and He purging (20 cm³ min⁻¹ He, 473 K, 1 h). Desorption of NH₃ (20 cm³ min⁻¹ He) was monitored in the range of 473–1173 K using a ramp rate of 10 K min⁻¹. Fourier transform infrared spectra (FTIR) were recorded in nitrogen atmosphere at 473 K using a Thermo Nicolet 5700 spectrometer using a SpectraTech Collector II diffuse reflectance accessory and equipped with a high-temperature cell. Prior to the measurement, the sample was dried at 573 K in N₂ flow (100 cm³ min⁻¹) for 1 h. Spectra were recorded in the range of 650–4000 cm⁻¹ with a nominal resolution of 4 cm⁻¹ and co-addition of 100 scans. ²⁷Al magic angle nuclear magnetic resonance spectroscopy (²⁷Al MAS NMR) was performed at a spinning speed of 10 kHz on a Bruker Avance 400 NMR spectrometer equipped with a 4 mm probe head and 4 mm ZrO₂ rotors. ²⁷Al spectra were recorded using 2048 accumulations, 90° pulses with a pulse length of 1 μs, a recycle delay of 1 s, and NH₄Al(SO₄)₂·12H₂O as the reference. Transmission electron microscopy (TEM) was performed by using a Phillips CM12 instrument operated at 100 kV. High-resolution transmission electron microscopy (HRTEM), high-angle annular dark field scanning transmission electron microscopy (HAADF-STEM), selected area electron diffraction (SAED), and energy-dispersive X-ray spectroscopy (EDX) measurements were performed by using a FEI Tecnai F30 microscope operated at 300 kV. SEM images of a resin-embedded granule were obtained by using a Zeiss Gemini 1530 FEG microscope operated at 1 kV. Standard

Table 2.1. Zeolite composition and porosity data.

Sample	Code	Si/Al ^a	V_{pore}^b	V_{micro}^c	S_{meso}^c	S_{BET}^d
		[mol mol ⁻¹]	[cm ³ g ⁻¹]	[cm ³ g ⁻¹]	[m ² g ⁻¹]	[m ² g ⁻¹]
Conventional	cz40	39	0.25	0.15	71	431
Conventional granule	cz40-G	32	0.32	0.13	91	394
Conventional extrudate	cz40-E	31	0.23	0.13	71	344
Hierarchical lab	hz40 _{lab}	28	0.60	0.11	255	537
Hierarchical mid	hz40 _{mid}	28	0.66	0.12	245	541
Hierarchical pilot	hz40 _{pilot}	28	0.56	0.12	256	544
Hierarchical granule	hz40-G	23	0.65	0.10	197	428
Hierarchical extrudate	hz40-E	23	0.41	0.13	142	355

^a Molar ratio in solid, determined by AAS; ^b Volume of N₂ adsorbed at a relative pressure (p/p_0) of 0.99; ^c t -plot method^[133]; ^d BET method^[134].

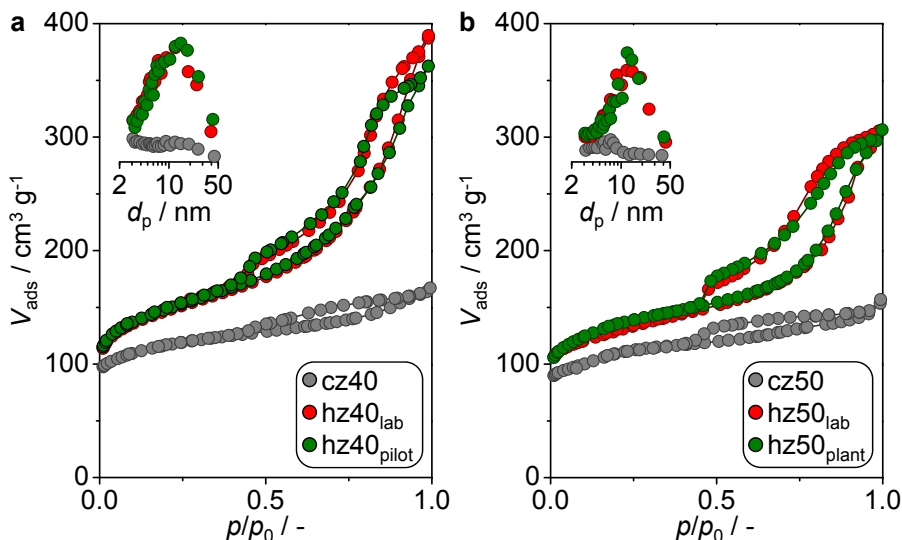


Figure 2.2. N₂ isotherms of the zeolites for (a) pilot- and (b) plant-scale preparation. Inset: Corresponding Barrett-Joyner-Halenda (BJH) pore size distributions calculated from the adsorption branch.^[135] d_p = pore diameter.

procedures were conducted to characterize the mechanical strength, including measurement of the lateral force required to crush the granule (crush strength) by using a hydraulic piston, and of the weight loss of fine particles generated during vibrational sieving in the presence of steel balls (attrition test).

2.3. Scale-up of Desilication Treatment

A primary objective of the scale-up was to reproducibly introduce intracrystalline mesoporosity into a ZSM-5 zeolite. For this purpose, controlled silicon extraction in alkaline medium (desilication)^[132,136–138] was performed on a zeolite at laboratory, mid, and pilot scales (Figures 2.1a-c, respectively, and Table 2.1). The conventional zeolite (cz40) with a ratio of Si/Al = 39 exhibited a single-phase MFI structure (Figure A.1) and the type-I N₂ isotherm (Figure 2.2a), characteristic of a purely microporous material. Its morphology is typical of a commercial zeolite, consisting of particles in the range 0.5–4 μm. Each particle (see the example in Figure 2.3a) comprises an aggregate of individual crystals of well-defined cubic shape (Figure 2.3b). Laboratory-scale alkaline treatment (0.2 M NaOH, 338 K, 30 min) led to a zeolite (hz40_{lab}, Table 2.1), which possessed a mesoporous surface area (S_{meso}) 3.5-times larger than the conventional zeolite and presented a slightly reduced micropore volume (V_{micro}). The combined type-I and type-IV behavior observed in the N₂ isotherm is a typical fingerprint of mesoporosity development upon controlled silicon extraction with pores centered at approximately 10 nm (Figure 2.2a).

Practical aspects associated with the mid- and pilot-scale preparation of mesoporous zeolites invoked certain modification of the laboratory-scale treatment procedure. Most notably, the temperature program was adjusted to conform to restrictions imposed with respect to handling and manipulation of the materials (Figure 2.1d). Treatment of 35 kg of conventional zeolite in a 1.5 m³ reactor produced a hierarchical zeolite (hz40_{pilot}) with nearly identical composition and porous properties as hz40_{lab}. Intermediate experiments in a 50 L reactor reaffirmed the reproducibility of desilication for mesoporosity generation (hz40_{mid}). Monitoring the textural changes during alkaline treatment in this reactor revealed that the principal increase in S_{meso} occurred rapidly during the initial reactor heating and reached a maximum value of about 250 m² g⁻¹. This remained constant throughout further treatment (Figure A.2).

TEM measurements reveal the higher beam transparency of hz40_{pilot} (Figure 2.3c) compared to cz40 (Figure 2.3a), owing to its increased mesoporosity. However, the size of the crystal aggregates does not change significantly. This aspect is advantageous for the next formation step because a method similar to that for conventional zeolites can be applied to the mesoporous

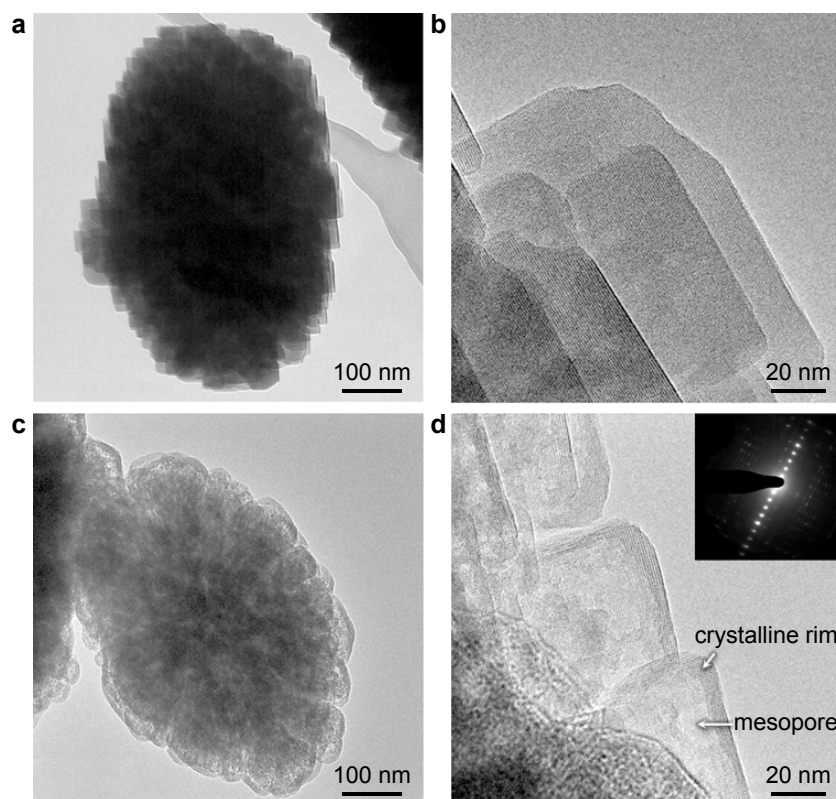


Figure 2.3. TEM images of (a,b) the conventional zeolite (cz40) and (c,d) the pilot alkaline-treated zeolite (hz40_{pilot}). (e) The inset shows the selected-area electron diffraction pattern of the crystal rim.

counterpart. Detailed examination of hz40_{pilot} by using high-resolution TEM demonstrated that the well-defined morphology of the conventional zeolite (Figure 2.3b) is mostly retained in the alkaline-treated analogue (Figure 2.3d). Although crystallites of cz40 exhibit a uniform contrast, areas of lighter contrast in hz40_{pilot} are associated with the presence of intracrystalline mesopores. The homogeneous distribution of mesopores throughout the zeolite crystal aggregate is clearly observable by dark-field scanning tunneling electron microscopy (Figure A.3). A very narrow crystalline rim, approximately 10 nm in width, remains intact around the edge of the mesoporous zeolite crystallites (Figure 2.3d). The presence of this rim in the desilicated samples may be related to Al enrichment at the surface of the conventional zeolite crystals.^[139,140] The crystallinity of the alkaline-treated zeolite was confirmed by the observation of lattice fringes and of sharp diffraction patterns when analyzed by using selected area electron diffraction (Figure 2.3e). The long-range order, as measured by using powder XRD, was also preserved (Figure A.1). Additional characterization of cz40, hz40_{lab}, and hz40_{pilot} samples, by using IR and ²⁷Al magic angle spinning (MAS) NMR spectroscopies and NH₃ temperature-programmed desorption, provided results typical of conventional and alkaline-treated ZSM-5

Table 2.2. Porous and acidic characteristics of zeolites prepared at industrial scale.

Sample	Code	Si/Al ^a [mol mol ⁻¹]	V _{micro} ^b [cm ³ g ⁻¹]	S _{meso} ^b [m ² g ⁻¹]	c _B ^c [μmol g ⁻¹]	c _L ^c [μmol g ⁻¹]
Conventional	cz50	49	0.14	69	99	36
Hierarchical plant	hz50 _{plant}	37	0.14	162	125	53

^a Determined by XRF; ^b *t*-plot method^[133]; ^c Concentration of Brønsted (*c*_B) and Lewis (*c*_L) acid sites determined by the infrared study of adsorbed pyridine.

(Figure A.4), further stressing the equivalent properties of the mesoporous zeolites prepared on laboratory and pilot scales.

2.4. Industrial Manufacture of Hierarchical ZSM-5 Zeolites

Culminating the previous section, the industrial manufacture of hierarchical ZSM-5 was undertaken at the production site of Zeochem AG (Uetikon, Switzerland) using a conventional ZSM-5 (Si/Al ratio = 50, coded cz50) produced by the company. Herein, due to the additional limitations imposed by the larger dimensions of the industrial reactor (15 m³) used for the batch treatment, the heating and, in particular, the cooling ramp had to be considerably lowered (Figure 2.1e), extending the total duration of the desilication treatment to approximately 6 h. Moreover, in order to comply with the standard procedure of ion exchange at the industrial scale, NH₄NO₃ had to be replaced by NH₄Cl as ion exchange agent when converting Na-ZSM-5 to NH₄-ZSM-5.

A series of validation experiments were conducted prior to the manufacture at industrial scale to assess the impacts of the extended treatment duration and of the replacement of the ion exchange agent on the mesopore quality and product yield. For the former case, to obtain a hierarchical ZSM-5 of high mesoporosity while maintaining a technically-viable treatment yield, the effects of shortening the isothermal step (5 *vs.* 30 min) and of reducing the alkalinity (0.1–0.2 M NaOH) of the solution were evaluated (Figure A.5a). Variation of the length of the isothermal step did not majorly alter the porous properties of the resulting hierarchical zeolite, when considering the duration of the heating and cooling steps. Comparatively, lowering the NaOH concentration to 0.15 M resulted in a zeolite with a reasonable compromise between a large external surface area of 166 m² g⁻¹ and an acceptable yield of 65%. Indeed, monitoring

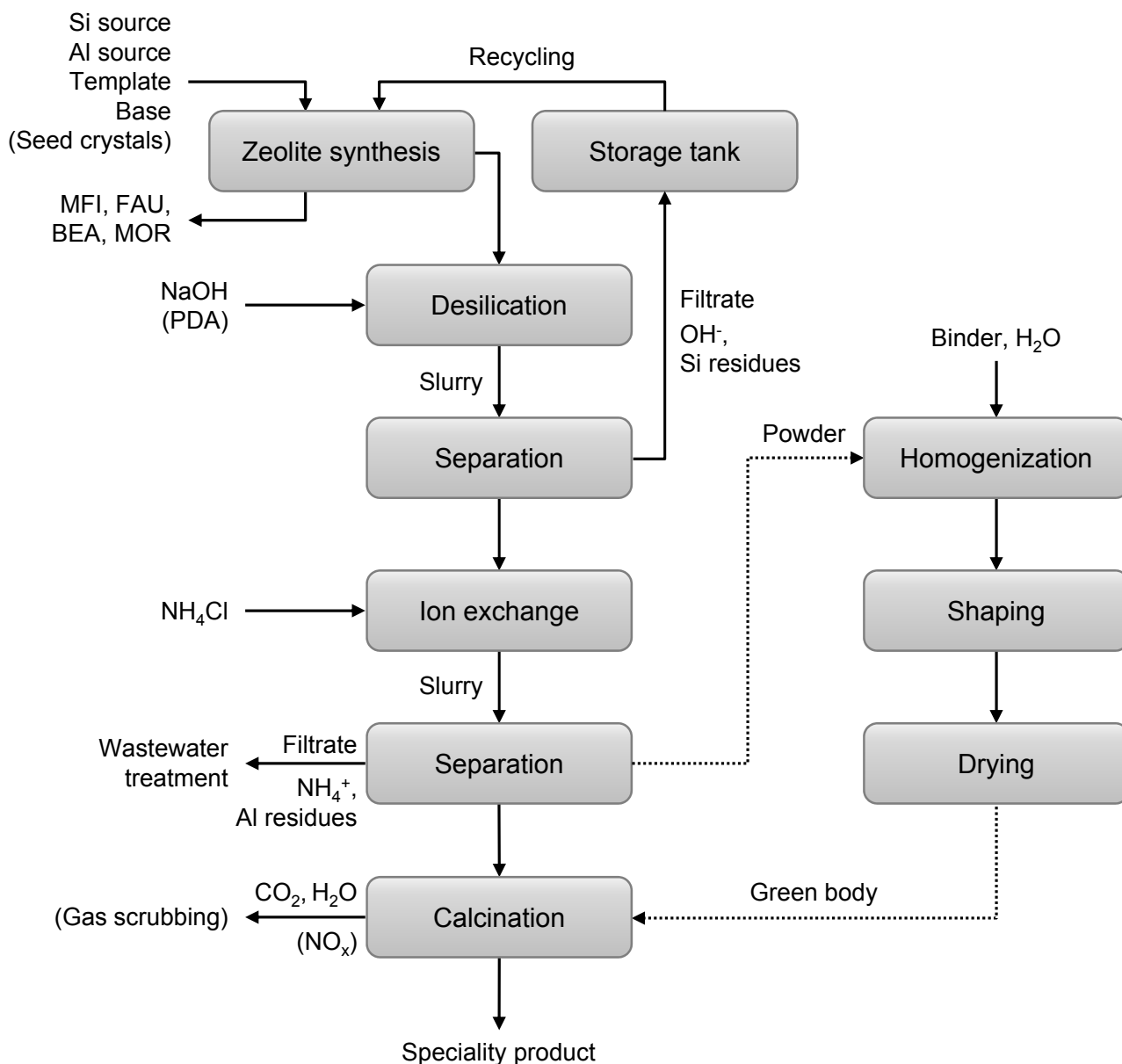


Figure 2.4. Envisaged unit operations to integrate the industrial manufacture of hierarchical zeolites, including the large-scale desilication treatment and the structuring into technical form, into the production facilities of a zeolite manufacturer.

the evolution of the porous properties during alkaline treatment at the plant-scale revealed that in this case the majority of the mesoporosity is formed after the heating step. The different observations from the mid-scale treatment could reflect the varying sensitivity of the conventional zeolites (cz40 and cz50) to the alkaline treatment, the difference in alkalinity, as well as in the more than 3-times different overall treatment duration (Figure A.5b). Assessment of the effect of the ion exchange procedure revealed that both NH₄NO₃ and NH₄Cl led to equivalent porous and acidic properties. Taking into consideration these modifications, 450 kg

of hierarchical zeolite (hz40_{plant}) was produced in a 15 m³ reactor, having nearly identical composition and porous properties as its analogue produced at lab scale (hz50_{lab}, Figure 2.2).

In terms of future production, several considerations to ensure its ecological and economic viability should be taken into account prior to the implementation of the desilication process into an existing zeolite manufacturing facility (Figure 2.4). Despite hierarchical zeolites being the superior catalysts, the sustainability of their preparation is still considered inferior to that of conventional zeolites. For example, while bottom-up protocols involve either the use of rare ingredients (*e.g.*, Ge) or complex organic templates, or low yields and/or poorly filtrable materials (*e.g.*, nanosized crystals), top-down approaches, like desilication, have been criticized for the leaching and thus loss of costly zeolite, and for the production of additional wastewater streams. Nevertheless, among the large variety of synthetic routes available to prepare hierarchical zeolites, no approach other than demetallation has been translated to the industrial scale. To make the manufacture of hierarchical zeolites more industrially-relevant, the recycling and treatment of wastewater streams as well as increasing the reactor productivity need to be considered. To reduce the amount of water utilized overall, the zeolite content (and concomitantly the alkalinity) of the desilication step could be increased, thereby raising the reactor productivity per liter of water.^[141] The Si-rich filtrate, consequent of the base leaching of the conventional zeolite, could then be recycled and reused as feed in a new zeolite synthesis.

Clearly, where local watercourses are used as the sink of waste streams, the latter must be extensively purified to preserve the drinking-water quality of the ecosystems. Accordingly, aluminum species leached into the liquid phase during acidic treatments, as the ion exchange procedure, as well as residual ammonium species present in the wastewater effluent of the second separation step following the ion exchange would need to be removed, and the salinity and pH adjusted. The Al residues could be flocculated, and subsequently the entire effluent could undergo reverse osmosis, an efficient but costly and time-consuming process. It is therefore of high economical and ecological interest to minimize waste streams.

The primary reason for the substitution of the ion exchange agent to NH₄Cl becomes evident at the final calcination step, where the contribution of the exhaust of nitrous gas species from NH₄NO₃ and the otherwise necessary and costly NO_x scrubbing can be prevented. However,

gas scrubbing cannot be completely avoided due to the combustion of ammonium species when converting $\text{NH}_4\text{-ZSM-5}$ to H-ZSM-5. In this regard, the use of diluted mineral acids, such as HCl, as ion exchange agent could be an alternative, to avoid the presence of ammonium cations. It is worth mentioning that although for ZSM-5 the use of NaOH suffices to desilicate, high-silica zeolites or those with more fragile frameworks (*e.g.*, USY) require the application of pore-directing agent. The use of organic cations, as tetrapropylammonium or diethylamine, would in turn entail their removal by combustion and thus gas scrubbing.

Finally, the use of more efficient reactor technology could be envisaged to improve reactor productivity and limit wastewater effluents. Switching from batch to continuous-mode operation could be one solution, employing smaller-sized reactors with improved heat/cooling efficiency. While the integration a continuous modus operandi for the production of hierarchical zeolites may be limited by the existing infrastrucutre of the production site and the enormous capital investment a new plant would entail, a detailed techno-economic assessment would be required to determine the optimum solution on an individual basis.

2.5. Shaping Hierarchical MFI Zeolite into Technical Bodies

Having found a reliable and cost-effective preparation method, the next step was to consider how the desilicated zeolite could be formed into practical shapes. Without clear fundamental guidelines on how to shape the powders obtained, a convenient starting point was to use equivalent structuring methods as applied for conventional zeolite.^[38] Following an industrial protocol (indicated by dashed lines in Figure 2.4), the mesoporous ZSM-5 zeolite was shaped into granules (Figure 2.5a, 2–3 mm diameter) or extrudates (Figure 2.5d, 4×10 mm) using a high-purity clay, attapulgite or kaolin, respectively, as binder. In contrast to previous work,^[142] we opted for the structuring of desilicated zeolite powders, instead of alkaline treatment of conventional zeolite bodies. The latter led to the disintegration of the bodies most likely associated with the weakening of interparticle interactions due to hydrolysis of the alkaline solution rather than leaching of the binder.^[38] Moreover, mesoporosity introduction was also less effective, and hence this option was rejected after preliminary trials.

The binder plays an important role in determining the properties of the resulting zeolite

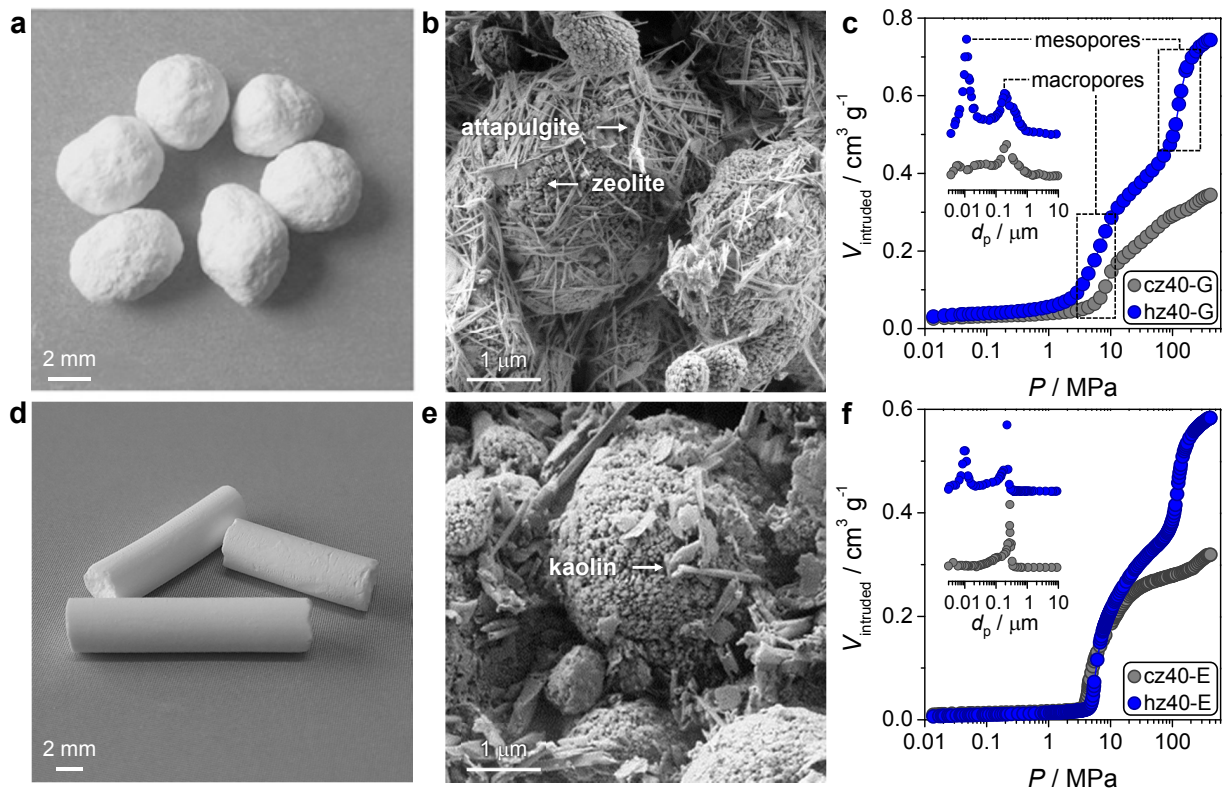


Figure 2.5. (a,d) Mesoporous zeolite granules, hz40-G, and extrudates, hz40-E. (b,e) SEM images of the bodies showing the distribution of binder in the agglomerates of mesoporous ZSM-5 crystals. (c,f) Mercury intrusion curves and derived pore-size distributions (inset) of the granules and extrudates of conventional and hierarchical ZSM-5.

bodies. During shaping the 'nests' of aggregated binder particles were dispersed and covered the surface of the zeolite particles (Figure 2.5b,e). In the case of attapulgite, the distinctive needle-like particle morphology of the binder facilitated phase identification during microscopic studies. N_2 adsorption confirmed that the mesoporous surface area was not blocked by the binder because the hierarchical zeolite granules and extrudates possess a S_{meso} of 197 and 142 $\text{m}^2 \text{g}^{-1}$, respectively, in agreement with those calculated based on the proportional contributions of the calcined zeolite and binder phases (Table 2.1 and Figure A.6). The small reduction in N_2 uptake arose from the inclusion of the binder, which has a lower porosity (Table A.1). No significant morphological alterations were observed in either of the component phases after forming. Mercury porosimetry (Figure 2.5c,f) provided additional information on the porous structure of the shaped bodies. In addition to the network of intracrystalline mesopores of approximately 10 nm, a macroporous network centered at *ca.* 200 nm coexisted (inset of Figure 2.5c,f). The latter mostly arose from interparticle spaces between the binder particles,

which were highly dispersed during shaping. As expected, the granules and extrudates of the conventional zeolite did not show a contribution in the mesoporous region. The mechanical properties of the conventional and mesoporous zeolite bodies were equivalent based on crush strength and attrition tests.

2.6. Conclusions

In conclusion, we successfully demonstrated the large-scale preparation of hierarchical zeolites. The robustness of the desilication route is clearly established by the identical properties of the mesoporous zeolites prepared from the laboratory to the industrial scale, despite the necessary adaption of the procedure. Finally, in a fundamental step, the formation of hierarchically-structured zeolite granules and extrudates was also reported. This paves the way for future research in the subsequent key steps in the design of mesoporous zeolites for various applications. In subsequent studies, structure-performance relationships of the hierarchical zeolite bodies in catalytic and adsorption processes will be addressed.

Visualizing Hierarchical ZSM-5 Zeolite Bodies from Macro to Nano Length Scales

3.1. Introduction

Processes that incorporate porous solids, often as catalysts or sorbents, are typified by their multidimensionality (Figure 1.1). Bridging these length scales is the main challenge for technology development.^[143] Materials' properties can be optimized and diversified by controlling the nanostructure.^[54,144–146] However, to profit from the resulting scientific advancements, they have to be put into a practical context. A critical task is the scale-up of laboratory leads into technical materials, which involves the translation of preparative routes from gram-to-tonne scale, with the derived powders then formed with the aid of binders and other additives into mechanically-stable macroscopic bodies.^[22,147] Advanced characterization methods for the study of porous solids in technical forms, in particular for their integrated visualization, are essential for understanding the assembly of such solids in large-scale manufacture and subsequent function in industrial reactors. Such insight will obviously increase the odds of successfully implementing improved technologies. Predominantly left to the realm of industry, fundamental knowledge is scarce regarding the scale-up and, correspondingly, the characterization of shaped bodies. Two major challenges are linking findings at different length scales and accounting for the co-existence of several interacting component species, such as the active phase and the binder.

A variety of techniques, including Raman, UV-vis-NIR and infrared microspectroscopies, magnetic resonance imaging, and X-ray absorption and diffraction microtomography (micro-CT) have been applied by de Jong, Weckhuysen and colleagues to investigate the evolution of metal species during the preparation and reaction of impregnated Al_2O_3 extrudates.^[148–152] However, visualization was limited to micrometer resolutions in most cases,

rendering these techniques powerless to access nanostructural details of the external and internal architecture, which are of crucial importance for the design of porous materials. Moreover, the imaging techniques were often used on an individual basis. Solving the complex structure of a technical porous material from macro- to nanoscale requires full integration of state-of-the-art methods, a challenge that to date remains unfulfilled.

Hierarchically-structured zeolites, like those introduced in Chapter 2, are currently attracting substantial attention on a laboratory scale because of their huge technological potential in catalytic, adsorption, and ion exchange processes.^[116] This class of crystalline aluminosilicates, which integrate networks of interconnected micro-, meso- and macropores, was developed in response to the inefficient utilization of conventional (purely microporous) zeolites in transport-based applications due to the constrained access and diffusion of bulky molecules.^[116,125,127,153,154] The large-scale preparation of hierarchical ZSM-5 zeolites has been achieved by alkaline treatment of commercial specimens, presented in Chapter 2.^[155] With a view to industrial implementation, the powders obtained have been subsequently shaped with conventional binders (for example, natural clays such as attapulgite or kaolin) into millimeter-sized granules and extrudates.

To refine scale-up principles, it is vital to establish the arrangement and interaction of individual constituents within macroscopic bodies, as well as the location and interconnectivity of the associated pore network. Although valuable, standard techniques for porosity assessment (gas sorption and mercury porosimetry^[156]) provide insufficient insight to correlate the textural properties of complex systems with their structural origins and can fail to account for inaccessible pores.^[157] The present study focuses on unraveling the complex organization of the hierarchically-structured ZSM-5 zeolites in technical form. For this purpose, optical, X-ray, and electron microscopic and tomographic techniques have been appropriately integrated to tackle a complex material with high potential to revolutionize zeolite catalysis. We stress that, although it has been used prevalently for the characterization of hierarchical zeolites, transmission electron microscopic (TEM) methods have so far only been applied to pure zeolite powders,^[139,158] which are not fully illustrative of their technical counterparts. Here, a concerted effort is made to ensure that our representative visualization specifically focuses on

non-invasive imaging modes and dedicated preparation methods to minimize alteration of the sampled volume. For the first time, we also demonstrate the outstanding performance of the scaled-up hierarchical ZSM-5 bodies in the conversion of methanol to light olefins.

3.2. Experimental

3.2.1. Zeolite Preparation and Shaping

The preparation of conventional and hierarchical zeolite technical bodies (*i.e.*, granules and extrudates) was described in Chapter 2.

3.2.2. Characterization Techniques

Argon adsorption at 87 K was measured in a Micromeritics ASAP 2020 system. Mercury intrusion was measured in a Micromeritics Autopore IV 9510 instrument. Fourier-transform infrared spectroscopy (FTIR) was conducted under nitrogen at 473 K using a Thermo Nicolet 5700 spectrometer equipped with a SpectraTech Collector II diffuse reflectance accessory and a high-temperature cell. Spectra were acquired in the range 4000–650 cm^{-1} with a nominal resolution of 4 cm^{-1} and the co-addition of 200 scans. The silicon and aluminum contents in the solid were determined by atomic absorption spectroscopy (AAS) using a Varian SpectrAA 220 FS spectrometer.

3.2.3. Visualization Techniques

Digital reflected light microscopy images of the zeolite granules were obtained with a Leica DVM 5000 microscope equipped with a 2.11 megapixel charge-coupled device (CCD) camera and a tungsten halogen lamp. Composite montage images were recorded with a $\times 35$ objective over a z-stack. Three-dimensional surface models were obtained using a $\times 2500$ objective by combining the montage image with the depth map.

Confocal fluorescence microscopy was undertaken using a Zeiss LSM 510 META laser scanning microscope with a Plan-Apochromat $\times 100/1.4$ oil objective lens. Detection ranges of 500–550 nm and 660–737 nm were used to record stimulated fluorescence, following illumination by monochromatic lasers of 488 nm and 633 nm, respectively. Sample preparation included

heating the granules for 15 min to 373 K, followed by addition of thiophene (Merck Chemicals), and quenching after 10 s of reaction. Nile blue (85%, Sigma Aldrich) dissolved in ethanol was subsequently added to the granules at ambient temperature.

Micro-CT was undertaken by scanning granules stepwise (0.4°) through 360° , using a Skyscan 1172 system operated at 100 kV and 100 μA .

SRXTM was performed using the TOMCAT beamline (2.9 T superbend photon source, critical energy 11.1 keV) at the Swiss Light Source (SLS), PSI, Villigen. Whole zeolite granules were studied in the standard (full-field) configuration. Nanocolumns etched from the zeolite granules by FIB were analyzed using the nanoscope set-up operated in Zernike phase contrast mode. Equiangular projections (3000 in full-field mode, 450 with the nanoscope) were acquired over 180° , using X-ray radiation optimized for maximum contrast at 15 keV. X-rays were converted into visible light by a cerium-doped LAG scintillator screen, magnified by $\times 20$, and digitized by a high-resolution CCD camera (PCO2000) using an exposure time of 200 ms (full-field) or 1 s (nanoscope). The images were post-processed online, rearranged into flat and dark-field corrected sinograms, and reconstructed using an optimized Fourier-based routine. Reconstructed images (16-bit) had a final voxel side length of 370 nm (full-field) or 84 nm (nanoscope). Three-dimensional reconstructions were generated using Amira software.

A Phillips CM12 instrument operated at 100 kV was used for standard TEM. Dimpled cross-sections of resin-embedded granules (G1 epoxy, Gatan) were prepared by mechanical cutting (Diamond Wire Saw 5237), dimple grinding (Fischione Model 200) and ion polishing (Gatan Model 691) to obtain a final sample thickness of 10–20 nm. HRTEM, HAADF-STEM and SAED measurements were undertaken using an FEI Tecnai F30 FEG microscope (300 kV). Precision-cut cross-sections with a thickness of *ca.* 10 nm were prepared with the microtome and analyzed by TEM using an FEI Morgani 268 microscope (100 kV).

Secondary electron micrographs of the uncoated samples were acquired using a Zeiss Gemini 1530 FEG SEM operated at 1 kV. FIB-prepared cross-sections were images in SEM mode (2 kV) using a Zeiss NVision 40 instrument equipped with an ESB (energy-selective backscattered) electron detector. Granules were resin-embedded (HM-20 low viscosity epoxy, Gurit) and trimmed using an ultracut microtome. Protective coatings of gold and carbon were applied. For

EDX analysis, small fields on the microtome trimmed surface were FIB-polished and coated with carbon (10 nm). Elemental mapping was obtained by SEM (FEI Quanta 200FEG) equipped with a silicon drift detector (Ametek EDAX Apollo X).

3.2.4. Catalytic Testing

The conventional and hierarchical H-ZSM-5 extrudates were tested in the conversion of methanol to hydrocarbons (0.8 g diluted with 23 g of silicon carbide). Methanol (99.9%) was evaporated, mixed with nitrogen gas (75 vol.% methanol with 25 vol.% N₂), and converted to dimethyl ether in a heated prereactor (548 K) charged with alumina. The vapor phase was introduced at the desired weight hourly space velocity (14.8 h⁻¹ with respect to methanol) into a fixed-bed continuous-flow reactor maintained at 723 K, and the gaseous product mixture was analyzed by on-line gas chromatography.

3.3. Porosity of Zeolite Bodies

High-resolution low-pressure argon adsorption and mercury porosimetry are widely applied methods in the determination of porosity in solids.^[156] The application of these techniques and appropriate models to hierarchically-structured zeolite granules (3–5 mm in diameter, prepared with 20 wt.% attapulgite binder) and extrudates (4 mm in diameter, prepared with 20 wt.% kaolin binder) confirmed the presence of a trimodal pore size distribution (Figure 3.1, symbols), centered at 0.5 nm (ZSM-5 micropore opening), 10 nm (intracrystalline mesopores created

Table 3.1. Porosity of the ZSM-5 bodies.

Sample	V_{micro}^a [cm ³ g ⁻¹]	S_{meso}^b [m ² g ⁻¹]	V_{meso}^c [m ² g ⁻¹]	V_{macro}^d [m ² g ⁻¹]
cz40-G	0.13	91	0.13	0.27
hz40-G	0.10	197	0.37	0.32
cz40-E	0.13	71	0.07	0.24
hz40-E	0.13	142	0.29	0.28

^a Micropore volume and ^b mesoporous surface area determined from argon sorption; ^c Volume of mesopores (3.7–50 nm) ^d and of macropores (>50 nm) determined from mercury porosimetry.

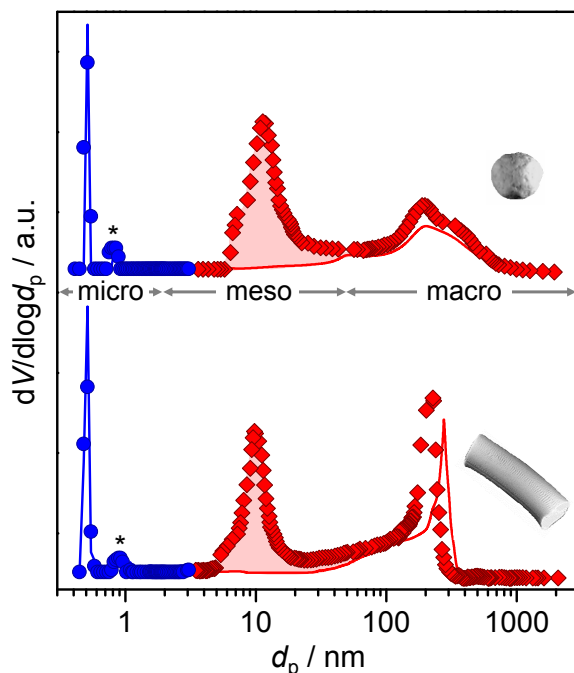


Figure 3.1. Pore size distributions determined by argon sorption and mercury porosimetry of the conventional and hierarchical ZSM-5 granules (top) and extrudates (bottom). The peak at 1 nm (indicated by an asterisk) is an artifact arising from the fluid-to-crystalline-like phase transition of the adsorbed phase in the MFI micropores.^[156] V is the volume of Ar adsorbed or the volume of Hg intruded, respectively; d_p is the pore diameter.

by controlled desilication) and 200–300 nm (macropores originating from the interparticle space between zeolite and binder particles). In contrast, equivalently prepared conventional ZSM-5 granules and extrudates exhibit a bimodal pore size distribution, without the mesopore contribution at 10 nm (Figure 3.1, lines).

The increased volume and surface area, arising from the extra level of mesoporosity in the hierarchical ZSM-5 bodies when compared to conventional samples, is quantified in Table 3.1. These differences are clearly visible in the argon isotherms and mercury intrusion curves in Figure A.7. Although revealing the size distribution, surface areas, and volumes associated with the pore structure, the above techniques are essentially blind to the structural features giving rise to these textural properties and are reliant on pore accessibility. With respect to the characterization of technical zeolites, important questions regarding the spatial distribution of the zeolite and binder particles and the topology of the heterogeneous inter- and intraparticle pore systems cannot be established from the obtained data. Direct visualization of the micro-, meso- and macropore networks by a combination of powerful microscopic and tomographic

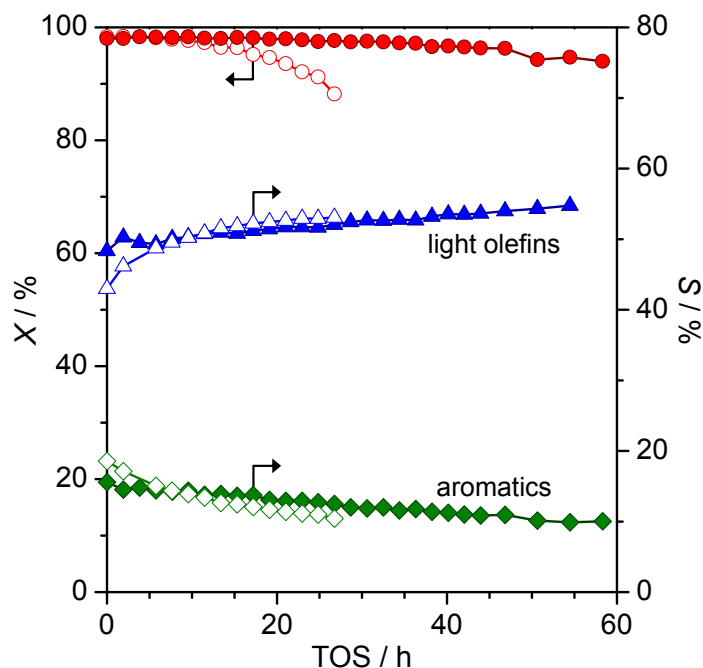


Figure 3.2. Catalytic performance of ZSM-5 bodies in the conversion of methanol to olefins (MTO). The superiority of the hierarchical zeolite (solid symbols) over the conventional zeolite (open symbols) is reflected by the more than three-times longer lifetime and moderately higher average selectivity to light olefins.

techniques is necessary to precisely elaborate on the above characteristics and to assess the procedural suitability of the scale-up of these advanced materials into technically-relevant geometries.

3.4. Catalytic Benefits of Shaped Hierarchical Zeolites

Before describing the visualization of the hierarchical ZSM-5 bodies, the superior catalytic performance of the zeolite extrudates in comparison with equivalently prepared extrudates of off-the-shelf conventional ZSM-5 for the conversion of methanol to hydrocarbons are illustrated in Figure 3.2. It has been demonstrated that the performance of conventional ZSM-5 zeolites is suboptimal because of fast deactivation by coking and that, by using hierarchical ZSM-5 powders, the lifetime can be extended as a result of the increased external surface area.^[159,160] However, the evaluation of hierarchical zeolites in technical form and the impact on product selectivity have not been reported. As shown by Figure 3.2, the hierarchical zeolite exhibits a cycle time of 50 h, compared to the 15 h of the conventional zeolite. A cycle is defined by the time at which the methanol conversion exceeds 95%. The similar distributions of light

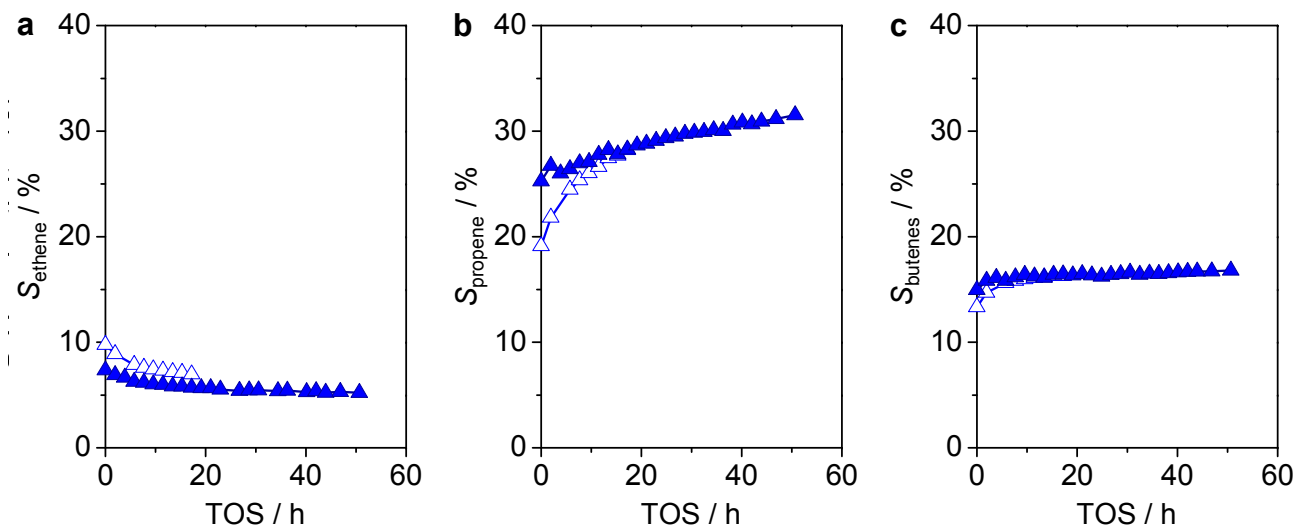


Figure 3.3. Selectivity to (a) ethene, (b) propene, and (c) butenes over conventional (open symbols) and hierarchical (solid symbols) ZSM-5 extrudates.

olefins observed for hierarchical and conventional ZSM-5 prove that the active sites leading to these species are not affected during modification of zeolite porosity. The relative selectivity to light olefins follows the trend propene > butenes > ethene throughout the catalytic cycle (Figure 3.3). Advantageously, the hierarchical zeolite exhibited a nearly constant selectivity profile during the whole cycle. This sample presents a higher average selectivity to C_{2-4}^{\equiv} olefins (52%) than the conventional zeolite (48%). In particular, it should be noted that the selectivity to propene (often the most desirable olefin in MTO) is higher in the hierarchical zeolite than in its conventional counterpart during the cycle (Figure 3.3b). The more than three-fold longer lifetime and the increased selectivity to olefins in the hierarchical sample results in a three-times higher yield of C_{2-4}^{\equiv} olefins per cycle (four times higher yield of propylene). This improved performance is mostly attributed to the presence of intracrystalline mesopores in the hierarchical zeolite bodies, which have largely preserved acidity properties (Figure A.8). Hence, enhancements in transport properties brought about by engineering the zeolite porosity have a decisive influence on both the stability and selectivity of the technical catalyst.

3.5. Visualization of Macroscopic Zeolite Bodies

Driven by the irrefutable impact of pore structure, the next challenge was to visualize the complex organization within the hierarchical ZSM-5 bodies that gives rise to their superior performance. A complete overview of the procedure adopted is illustrated here for hierarchical ZSM-5 granules. The battery of applied techniques is summarized in Figure 3.4. It should be emphasized that each visualization technique was systematically conducted at least twice over randomly selected particles with the same shaped body (granule or extrudate) to verify the representativeness and reproducibility of the preparation. The essentially identical nature of each type of shaped body examined proves demonstratively that the resulting information is integrative. The structural homogeneity of the shaped forms throughout the entire batch confirms the success of scale-up in terms of product uniformity and reproducibility, stressing the practical value of these materials.

The three-dimensional macrostructure of the hierarchically structured zeolite granule can be imaged by digital reflected light microscopy, without dedicated specimen preparation (Figure 3.4a). Using an automated z-stack at higher magnification, surface profiles of the hierarchical zeolite granules show a relatively uniform roughness, with the possibility of resolving the closely aggregated component particles (Figure 3.4c). An important design parameter is the distribution of zeolite particles within the technical bodies. Fluorescence microscopy has revolutionized optical microscopic techniques, offering the capacity to visualize chemical reactivity at the nanoscale.^[161–163] Confocal laser scanning microscopy (CLSM) was recently used to identify the active Y zeolite phase within appropriately stained fluid catalytic cracking catalyst.^[163] Products formed by the reaction of thiophene with zeolitic Brønsted acid sites at 373 K produce green fluorescence upon illumination with a 488 nm laser. Zeolite particles are easily recognizable in the external surface region of hierarchical zeolite granules and have varying size (Figure 3.4d). In comparison, Nile blue is too bulky to enter the micropores and covers the external surface of the zeolite and binder particles. The red fluorescence, observed when illuminated by a 633 nm laser, is less distinct and appears evenly across the image. This is consistent with the relative proportion of the binding (20 wt.%) and zeolite phases and demonstrates a homogeneous dispersion within the field of view. Overall,

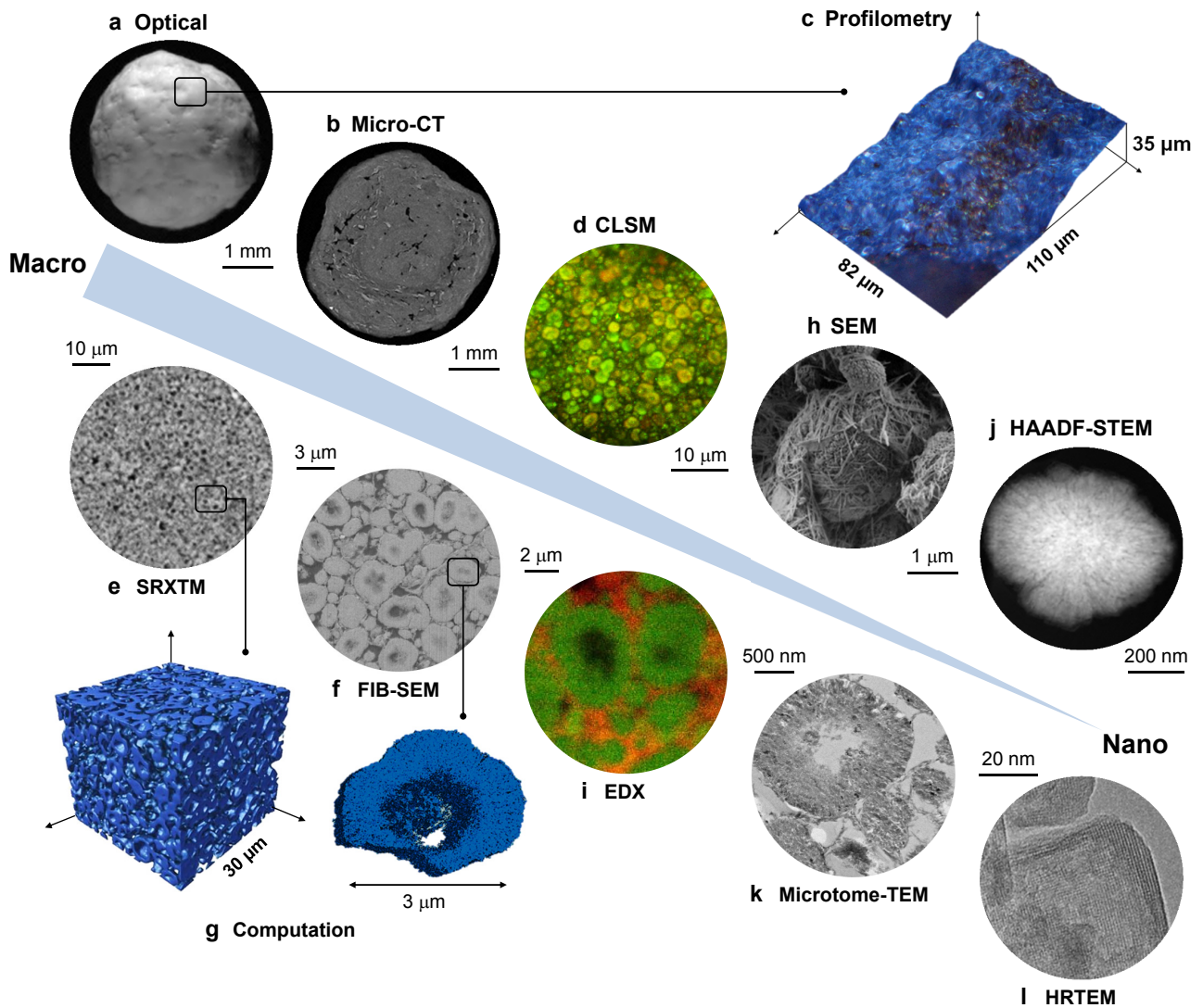


Figure 3.4. Integrated approach to the visualization of a hierarchical zeolite body from macro to nano length scales. (a) The macroscopic structure of a hierarchical zeolite granule is observed by optical microscopy, and (b) the internal structure is revealed by X-ray micro-CT, providing insight into the agglomeration behavior within the shaped body. The structure of the external surface is further examined by (c) profilometry and (d) CLSM. (e) SRXTM and (f) FIB-SEM reveal the homogeneous internal distribution of zeolite and binder phases and permit visualization and (g) computation of the macro- and mesopore structures. (h) The arrangement of binder particles at the external surface of zeolite particles is seen by SEM, and (i) elemental maps of silicon (green) and aluminum (red) are obtained by EDX. (j) A HAADF-STEM image confirms the uniform distribution of intracrystalline mesopores within individual zeolite aggregates. Nanostructural insights are gained through (k) TEM study of microtome cross-sections and ultimately by (l) HRTEM.

the maximum structural resolution achieved is limited to the distinction of zeolite particles. Interestingly, darker regions are identified in the centers of large hierarchical zeolite particles. Although unclear from CLSM alone, the origin of this effect was uncovered during investigation using complementary techniques (Figure 3.5).

3.6. Visualization of the Interior Structure

To fully contextualize components within macroscopic zeolite granules, it is necessary to study beneath the surface. X-ray tomographic techniques are powerful tools for the non-destructive analysis of the internal structural organization of bodies, such as Ni/Al₂O₃ catalysts^[152] and fuel-cell electrodes^[164,165]. In absorption-based studies, the X-ray beam is attenuated by the sample according to its internal structure and composition, with a strong dependence on atomic number. With laboratory sources, the virtual cross-sectional slices computed from micro-CT can be used to model the three-dimensional macrostructure of the hierarchical granules and to assess the agglomeration behavior (for example, homogeneity of phase distribution and the presence of internal voids, cracks, impurities and so on), with optimal resolutions of *ca.* 1 μm (Figure 3.4b).^[152] The application of high-flux synchrotron radiation in the hard X-ray range gives improved time and spatial resolution, permitting the visualization of features down to the submicrometer level.^[166] The uniform long-range structural order of hierarchical zeolite granules is visible from the homogeneous appearance of the two-dimensional virtual slices computed from standard synchrotron radiation X-ray tomographic microscopy (SRXTM) measurements of whole zeolite granules (Figure 3.4e). Pores appear as black regions, while the denser and therefore more adsorbing zeolite and binder particles appear as areas of lighter contrast, uniformly spread throughout the entire granule.

In this study, the contrast of the zeolite and binder phases is similar because of their comparable density, which results in similar attenuation of the X-ray beam. Owing to the narrower field of view, samples that are *ca.* 40 μm in size are ideally suited for high-resolution SRXTM studies using a nanoscope set-up.^[167] To ensure the accurate portrayal of the internal granule structure, individual nanocolumns were cut using a focused ion beam (FIB), transferred and tightly secured to stainless-steel needle sample holders, with no visible damage to the sampled volume (Figure 3.5a-c). Embedding the sample in standard resins to improve the mechanical stability would have resulted in an undesirable reduction of the phase contrast between pores and particles. The similar appearance of the images computed from the nanoscope and full-field SRXTM studies confirm that no structural alteration occurs during nanocolumn preparation. A virtual two-dimensional slice from the nanoscope data is shown

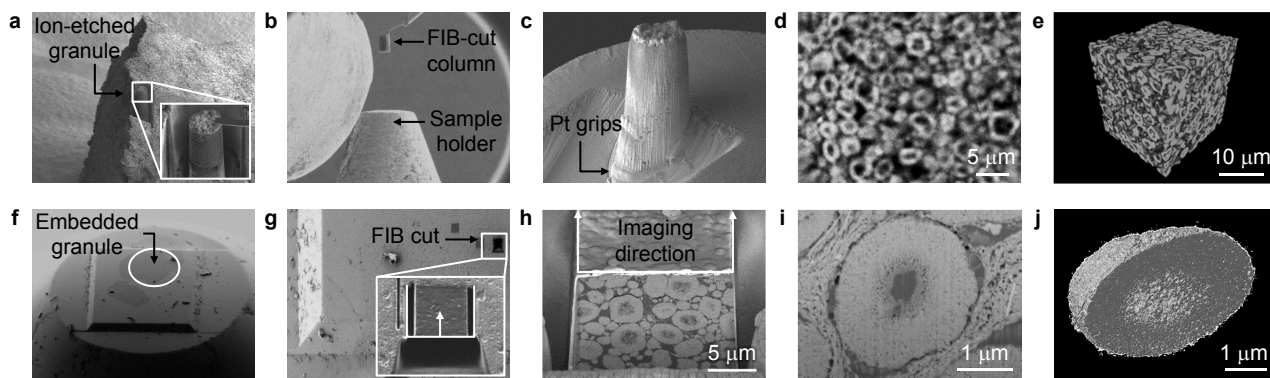


Figure 3.5. Internal structure of a hierarchical zeolite body by high-resolution SRXTM and FIB-SEM. (a-c) For SRXTM analysis, nanocolumns prepared by FIB-etching of a granule are transferred to the sample holder and fixed tightly by platinum deposition. (d,e) Two-dimensional virtual slices obtained through three-dimensional SRXTM can be used for quantitative study of the macropore structure within a defined volume. (f-h) For FIB-SEM analysis, resin-embedded granules are prepared using a FIB cutting technique to expose an area of *ca.* $20 \times 20 \mu\text{m}^2$ of the sample. (i) A dual-beam FIB-SEM method is used to image sequential slices, (j) allowing three-dimensional visualization of individual hierarchical zeolite particles.

in Figure 3.5d. The resolution is evidently higher than that of the standard experiments. Ring-like structures are observed, with diameters of 3–5 μm and porous centers, surrounded by smaller solid particles and macropores of varying dimensions. Based on our knowledge of the components, these features are assigned to zeolite particles, but identification of binder particles is not possible from the data collected. The macropore connectivity within the granules was examined by generating an isosurface from the tomographic data by enclosing voxels with the weakest intensity (black, 0–5%). Three-dimensional reconstructions demonstrate the spheroidal shape of the circular features, enclosing macropores that are isolated from the surrounding interparticle macropore network. The latter consists of interconnected macropores of varying size and orientation, which extend throughout the granule interior. When computed over a fixed volume, the macropore structure can be observed and quantified (Figures 3.4g and 3.5e).

3.7. Visualization to the Nanoscale

The application of electron microscopic techniques permits more detailed study of the structural organization in hierarchical zeolite granules, bridging the meso- and nanoscales. Herein, it is important to consider that as the resolution increases, the field of view invariably decreases, requiring a careful assessment of how representative the measured images are. Moreover,

advanced specimen preparation is crucial to ensure that the structure of the technical body does not change, and can be extremely demanding. Focused ion beam-scanning electron microscopy (FIB-SEM) can be applied to perform microscopic and subsequent tomographic studies of the internal microstructure over large areas (for example, *ca.* $20 \times 20 \mu\text{m}^2$) with resolutions down to the nanometre level,^[168] irrespective of the specimen size and thickness.

In this work, resin-embedded granules (Figure 3.5f) were observed on planar section cuts during sequential slicing by FIB (Figure 3.5g,h). The differing morphologies of the component phases are clearly distinguishable in a typical backscattered electron image (Figure 3.5i). The high degree of complementarity between FIB-SEM and SRXTM (Figure 3.5d) observations confirms that the granule structure is not modified by sequential etching with the FIB. A single hollow zeolite crystal aggregate with a diameter of 2–3 μm is observed to be enshrouded in the web-like matrix of the binder. A clear distinction of individual binder particles, which appear to form a fairly continuous network, is not possible. Interparticle macropores are present within the binding matrix and between the matrix and the nanostructured zeolite particles. The center of the zeolite particle is completely filled with resin, demonstrating its interconnectivity with the external surface. The formation of hollow centres upon desilication of large single crystals is known to arise from aluminum zoning in the conventional zeolite.^[159] The distinct compositions of the binder and zeolite phases (molar Si/Al = 28) are clearly differentiable in the images obtained by energy-dispersive X-ray (EDX) spectroscopy (Figure 3.4i). A typical sequence of images obtained by FIB-SEM analysis shows the improved visibility of the zeolite and binder particles. The higher level of detail facilitated computational reconstruction of this data set (Figures 3.4g and 3.5j). The three-dimensional outward appearance and cavernous interior can be computed for individual zeolite particles.

Having the potential to reach atomic-level resolution,^[169–171] TEM is highly relevant for the study of nanostructured materials. TEM tomography has attracted significant attention in the imaging of pore structure and the characterization of the distribution of active metal nanoparticles within porous inorganic supports in powder form.^[158,172] A method to quantify textural properties using TEM-based electron tomography was recently demonstrated for steamed and acid-leached zeolite Y in conventional powder form,^[173] allowing the detection

of porosity not probed by conventional methods such as gas adsorption and porosimetry. However, a major drawback is the requirement for beam transmission, which restricts the range of applicable sample thicknesses. TEM observations of resin-embedded, dimpled, and argon-etched cross-sections (Figure 3.6a) demonstrates features similar to those obtained from FIB-SEM. However, owing to the relative thickness of these cross-sections, the predominantly intact zeolite particles appear opaque. In contrast, the binder particles surrounding the zeolite phase are relatively transparent and are not easily distinguishable. Greater beam transparency in the center of larger particles suggests their lower density. A unique glimpse of the structure within large zeolite particles is obtained from the study of precision-cut cross-sections prepared from resin-embedded granules (Figures 3.4k and 3.6b). The overall particle structure is similar to that

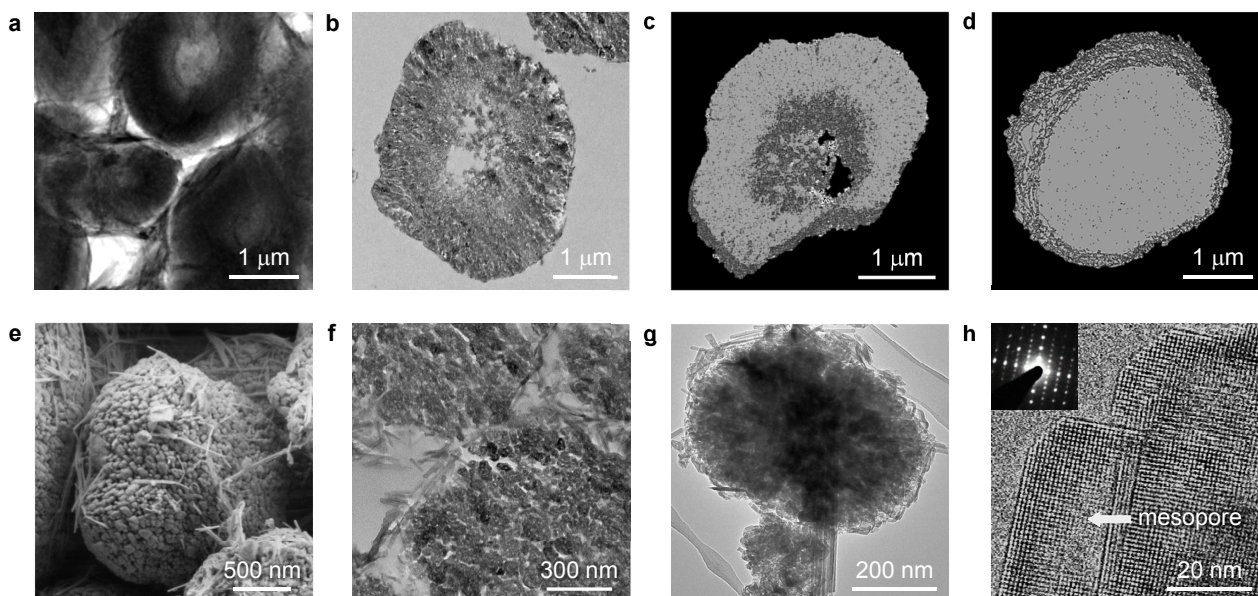


Figure 3.6. Detailed analysis of the zeolite phase. (a) TEM examination of dimpled samples confirms the densely packed arrangement within hierarchical zeolite granules, but detailed visualization is limited by the sample thickness. (b) The study of microtome-cut cross-sections of an embedded granule permits visualization of the large transport pores (meso-macropore range) within individual zeolite particles. A direct correspondence is seen with the results of FIB-SEM tomography. The more open structure of (c) the hierarchical ZSM-5 with respect to (d) the conventional ZSM-5 is strikingly evident on comparison of cross-sectional slices (thickness of 200 nm) computed through the zeolite particles. (e) The binder-covered zeolite crystal aggregate imaged by SEM reflects the close association between the two phases, which is evidenced in TEM images of the (f) microtome-cut and (g) crushed samples. (h) Examination by HRTEM provides a detailed characterization of the complex distribution of intracrystalline mesopores in the zeolite phase of the hierarchical material. The clear observation of lattice fringes and of sharp SAED patterns (inset) confirms the preserved crystallinity of the microporous zeolite phase. Mesopores within the individual zeolite crystals are also imaged.

observed by FIB-SEM (Figure 3.5i), but with a higher contrast between the porous and solid regions. Macropores and large mesopores are seen to radiate into the crystal aggregate from the external surface (Figure 3.6b). The hollow core of the pictured zeolite particle appears cavern-like, containing protrusions of undissolved zeolite crystals. Smaller interconnected mesopores within individual zeolite crystals are observed at higher magnifications. A remarkably close correspondence is seen with the observations of cross-sections of individual zeolite particles computed by FIB-SEM tomography (Figure 3.6c), indicating the high resolution obtainable from these techniques. In comparison with the hierarchical ZSM-5, the conventional ZSM-5 particles show virtually no presence of large internal macro- or mesopores (Figure 3.6d).

The tightly aggregated polycrystalline (individual crystallite size *ca.* 50–70 nm) nature of the zeolite particles (Figure 3.4h and 3.6e) was clearly demonstrated in high-resolution SEM studies of dimpled cross-sections at low working voltages (1 kV). Individual binder particles, which have a needle-like morphology (*ca.* 10–20 nm width and 0.5–1 μm length), appear wrapped around the zeolite phase. The presence of hollow centers is not obvious from the exterior surface of the zeolite particles. The local arrangement of binder particles is observed in the TEM images of the microtome-cut cross-sections (Figure 3.6f) and crushed bodies (Figure 3.6g), where they are seen to be wedged between the zeolite particles. The presence of intracrystalline mesopores, introduced in the zeolite by alkaline treatment, is evident upon analysis of crushed samples. Small zeolite particles exhibit a uniform mesopore distribution in the 10 nm range throughout the crystal aggregate, with no evidence of hollow centers (Figure 3.6g). Similar conclusions are drawn from analysis using high-angle annular dark-field scanning TEM (HAADF-STEM; Figure 3.4j), where the contrast between porous and solid regions is reversed. The intracrystalline mesopores and crystallinity of the microporous zeolite structure are clearly uncovered by combined high-resolution TEM (HRTEM) and selected-area electron diffraction (SAED) analysis (Figure 3.6h), reaching nanoscale resolution.

3.8. Applicability to Other Geometries

Comparative visualization of hierarchical zeolite extrudates has demonstrated that the alkaline-treated ZSM-5 powders can be shaped into different technical forms (Figure 3.7). Herein, the

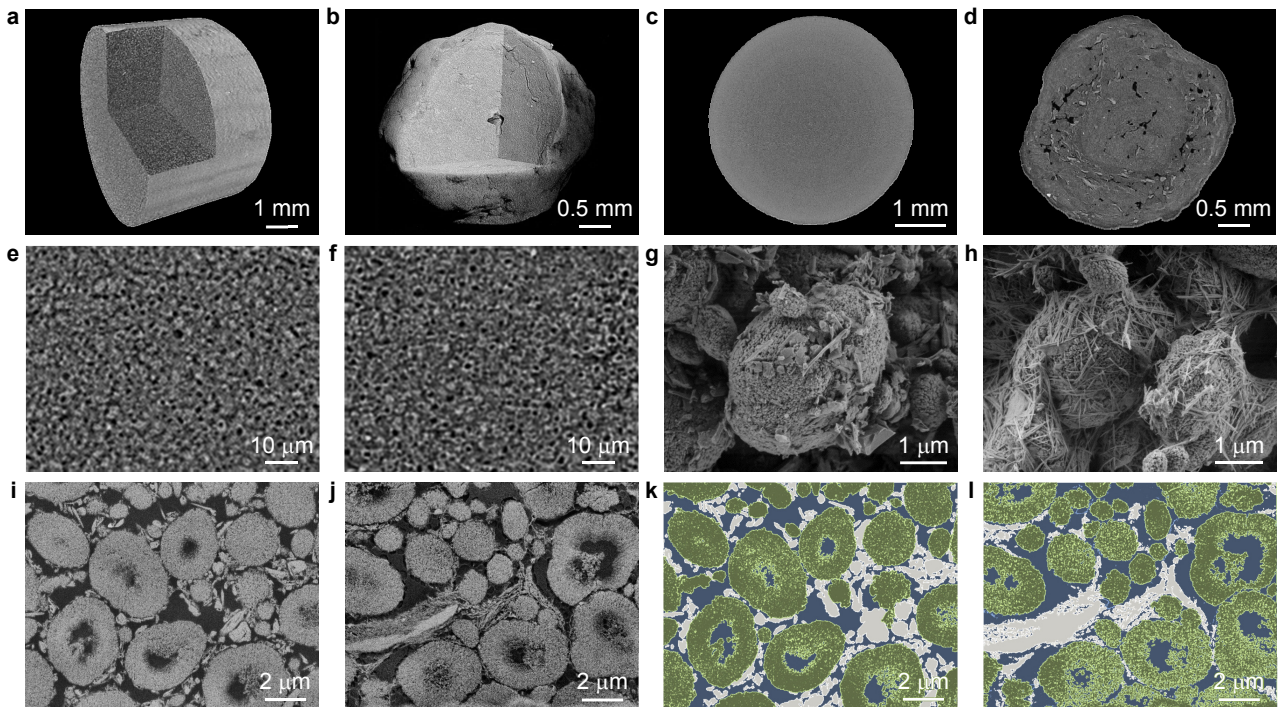


Figure 3.7. The successful comparison of hierarchical ZSM-5 confirmed the general applicability of the visualization approach and emphasized the different structural insights gained by each technique. Images a, c, e, g, i, and k belong to the extrudates, and b, d, f, h, j, and l belong to the granules. Comparison of (a,b) volume-rendered three-dimensional structures and (c,d) representative cross-sectional slices evidenced the absence of agglomeration defects in extrudates with respect to granules, in which voids and cracks are clearly detected. (e,f) The uniform internal packing of zeolite and binder particles within extrudates and granules is illustrated by SRXTM. (g,h) The binder morphology is most clearly distinguished by high-resolution SEM. (i,j) FIB-SEM images reveal differences in the organization of component species, visualized by examination of computer generated (k,l) color maps, highlighting the dispersion of binder (grey) and zeolites particles (green) and the interstitial macropores (blue). The different arrangements directly influence the structure and connectivity of the inter-particle macropore network, which can be quantified by further image processing.

improved macroscale uniformity of the extruded form in comparison with the granulated form is clearly distinguished. The latter observation is attributed to the different conditions (that is, pressure, temperature, and water content) and related agglomeration mechanisms acting during extrusion and granulation. The different pore topologies present in the granules and extrudates (despite exhibiting similar macropore volumes, Table 3.1) due to the distinct morphologies and arrangements of the binder particles (clearly visible by high-resolution SEM and FIB-SEM) is also evidenced. The structural insight gained from study of the different geometrically shaped bodies confirmed the generality of the visualization approach, demonstrating its potential utility for the quality assessment of technical catalysts.

3.9. Conclusions

For the first time, it was demonstrated that hierarchically-structured zeolite bodies prepared by demetallation preserve their outstanding catalytic performance upon structuring into different geometries, exhibiting superior lifetime and selectivity in the production of light olefins from methanol when compared to conventional analogues. An integrated visualization methodology, combining optical, X-ray, and electron-based microscopic and tomographic techniques, comprises a unique approach to imaging, at multiple length scales, the different porosities and connectivities in hierarchical bodies. Digital optical microscopy was used to analyze the topography of the studied hierarchical granules and extrudates, while CLSM, with appropriate staining, was used to identify the zeolite phase distribution at the surface level. Micro-CT and SRXTM enabled non-destructive analysis of the interior structure, although the resolution was insufficient to distinguish individual binder particles. FIB-SEM complemented by EDX proved the most informative technique, providing a broad field of view with sufficient resolution to assess the distribution and composition of the binder and zeolite phases. High-resolution SEM gave detailed insight into the local zeolite-binder interaction. TEM examination in different modes captured key nanostructural aspects of the zeolite phase.

The structural information accumulated by applying the package of imaging techniques has clear implications for advancing the scale-up and functional understanding of novel porous solids in diverse industrial applications. Knowledge regarding the local interaction and long-range arrangement of zeolite and binder particles, and the related levels and connectivity of porosity within millimeter-sized bodies, is essential in confirming the structural homogeneity, and thereby demonstrate the success of scale-up. In catalyzed reactions, efficient mass transfer is highly correlated to these parameters. A method to assess the structural hierarchy within shaped bodies is indispensable in beginning to understand and thereafter improve zeolite utilization in technical form (for example, by studying the influence of the shaping method, the identity and proportion of the hierarchical zeolite, and the choice of binder). Going beyond this, the use of similar visualization strategies can be generally envisaged for the determination of structure/performance relationships for technical catalysts.

Effects of Binders on the MTH Performance of Shaped Hierarchical ZSM-5 Zeolites

4.1. Introduction

The development of industrial catalysts implies the identification of practically and economically scalable recipes to obtain high performance materials in macroscopic forms suitable for their large-scale implementation.^[22,147] Although the approach to scale-up, including the choice of formulation and shaping method, can profoundly impact the properties of the resulting catalysts, few academic studies have been devoted to rationalizing the possible effects. The need for a better understanding was recently highlighted in the vibrant area of zeolite catalysis, revealing that interactions with binders, which are vital components for their technical application, could result in multiple effects of both chemical and physical origin.^[60,174]

An important zeolite-catalyzed reaction, in which binders have been reported influential, is the conversion of methanol to hydrocarbons (MTH).^[50,97,101,175–180] Significant advancement in the mechanistic understanding of the interplay between the properties, the process conditions, and the performance has been gained over a wide variety of zeolite framework types, including those of the commercially applied ZSM-5 (MFI-type) and SAPO-34 (CHA-type) catalysts.^[181–186] However, since the vast majority of this knowledge was derived over pure zeolite powders, the impact of shaping remains intangible.

The potential relevance of zeolite-binder interactions can be clearly illustrated in the case of ZSM-5 catalysts, which exhibit a broad product distribution.^[182] Consequently, the zeolite properties must be carefully tuned to optimize the selectivity to the desired product slate. For example, when targeting olefins, the density or strength of the Brønsted acid sites is known to be crucial.^[182,183] Moderation of the latter by direct synthesis (*e.g.*, by adjusting the Si/Al ratio^[183,187]), through post-synthetic modification (*e.g.*, by impregnation with diverse species

such as P, Ga, B, Ca, Mg, *etc.*^[188–192]), or by dealumination^[193] or silylation^[194] treatments are all strategies to enhance the performance. Nonetheless, because it is well known that acid sites can be created or lost as a result of the intimate contact between the zeolite and binder phases in shaped catalysts,^[97,101,102] an improved understanding and control over binder effects would be advantageous.

Another critical consideration in the design of MTH catalysts is how to abate the progressive loss of activity due to fouling with time on stream, which determines the reactor downtime in the fixed-bed process. A significant advance was the recognition that the coke tolerance can be improved through hierarchically-structuring the zeolite porosity.^[159,160,195,196] This can be achieved either through the introduction of intracrystalline mesopores (*e.g.*, by carbon templating^[160] or demetalation^[159,180,195]), or through the synthesis of nanosized zeolites (*e.g.*, by organic co-templating^[160]), or by seeded synthesis in fluoride media.^[196] Although in Chapter 3 it was demonstrated that a superior lifetime could be preserved in technical form,^[180] the impact of shaping, either as a result of the change in macroscopic structure or the potential reaction with the binder, on the performance of the hierarchical zeolite was not decoupled.

Having succeeded in shaping hierarchical zeolites at the industrial scale (Chapter 2), it is essential to translate that knowledge to the laboratory scale to enable the screening of potential formulations and structuring protocols in smaller quantities at an accelerated manner. Accordingly, to provide further insight into binder effects, this chapter studies the influence of shaping with commercial silica, alumina, kaolin, and attapulgite clay binders on the properties of conventional and hierarchical ZSM-5 zeolite catalysts of different framework compositions at the bench-scale. The origin and extent of shaping-induced variations in the porosity and acidity of the catalysts are elucidated by systematic characterization of the individual components and of zeolite-binder admixtures prepared by physical mixing, extrusion, or ball milling. The impact on the activity, selectivity, lifetime, and coking behavior of the composite catalysts in the MTH reaction is subsequently quantified at different temperature and weight-hourly space velocity. The beneficial application of ball milling as a parallel lab-scale tool through which to simulate the intimate phase contact experienced during extrusion is demonstrated.

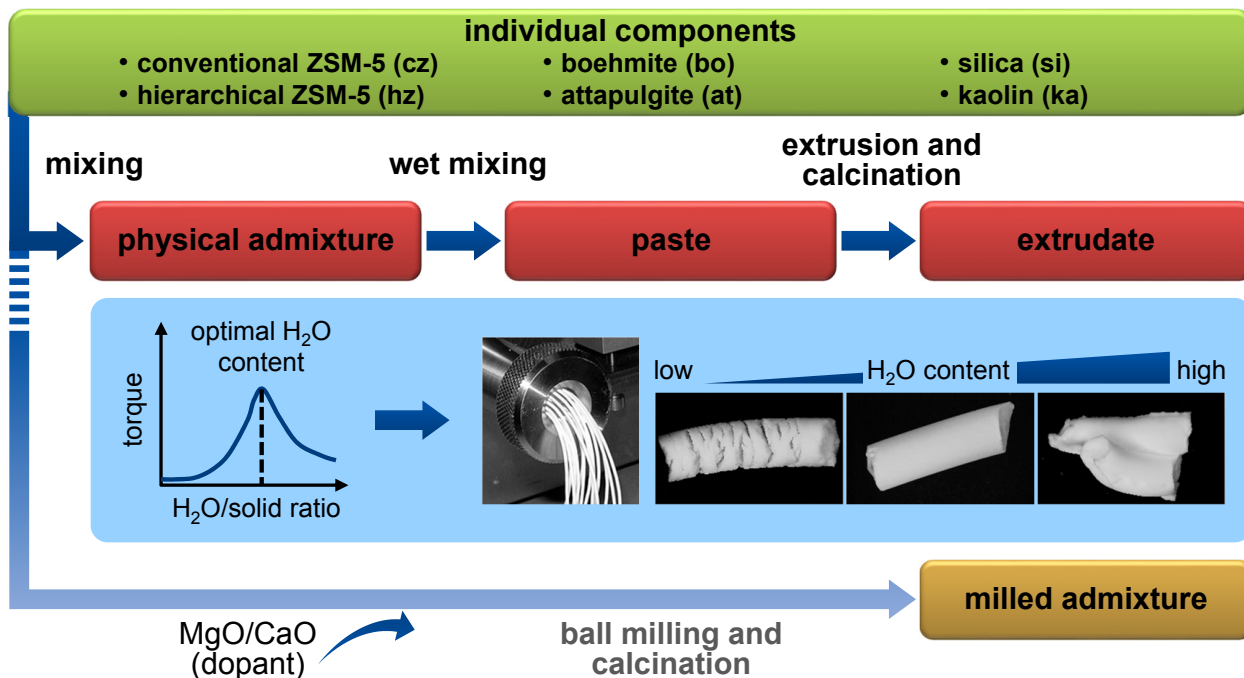


Figure 4.1. Principal stages in the preparation of zeolite extrudates with various binders. Ball milling provides a parallel route by which to maximize zeolite-binder interactions.

4.2. Experimental

4.2.1. Catalyst Preparation

The hydrothermal synthesis and pilot-scale desilication of the conventional ZSM-5 zeolite ($\text{Si}/\text{Al} = 39$, coded cz40) to obtain the hierarchical analogue (coded hz40) is elaborated in Chapter 2. The binders investigated in this study included silica (Sipernat 320D, Evonik, coded si), acid-dispersed boehmite (0.3 M HNO_3 , $3.3 \text{ cm}^3 \text{ g}_{\text{binder}}^{-1}$, Dispersal, Sasol, coded bo), and two natural clays, kaolin (Sigma Aldrich, coded ka) and attapulgite (Sigma Aldrich, coded at). Acid-treated attapulgite (coded at_{HCl}) was obtained by treating the as-received clay in aqueous HCl (1 M , $30 \text{ cm}^3 \text{ g}_{\text{binder}}^{-1}$) at 298 K for 1 h , followed by filtration and washing.

The principal steps in the laboratory-scale extrusion of the conventional or hierarchical zeolites are shown in Figure 4.1. The zeolite and binder ($1:1$ dry mass ratio, accounting for the weight loss upon calcination to 873 K) were homogenized in a speed mixer (SpeedMixer, FlackTek Inc.), first as dry powders and then in the presence of a pre-determined amount of water to form pastes that could be subsequently shaped using a Mini Screw Extruder (Caleva). A mixer torque rheometer (MTR3, Caleva) was used to optimize the solid-to-liquid ratio. The

resulting extrudates were dried in a convection oven for 12 h at 393 K prior to calcination at 873 K for 3 h (2 K min^{-1}) in flowing air ($60 \text{ cm}^3 \text{ min}^{-1}$) in a tubular furnace (Carbolite GHA).

Physical admixtures were obtained by directly mixing the calcined (873 K, 3 h, 2 K min^{-1} , $60 \text{ cm}^3 \text{ min}^{-1}$ flowing air) zeolite and binder powders (1:1 mass ratio). Milled zeolite-binder admixtures were prepared by treatment in the presence of water (20 vol.% more than the amount required for extrusion) using a planetary ball mill (60 min, 500 rpm, Retsch), and were dried and calcined equivalently to the extrudates. In some cases, the zeolite-binder admixtures were doped with MgO (2.5 wt.%, Strem Chemicals, coded *e.g.*, ka_{Mg}).

To verify the impact of the framework composition, two additional commercial ZSM-5 zeolites with nominal Si/Al ratios of 15 and 140 (CBV 28014 and CBV 3024E from Zeolyst, both NH₄-form, coded cz15 and cz140, respectively) were compared as reference materials. In this case, the hierarchical ZSM-5 counterparts (coded hz15 and hz140) were obtained by alkaline treatment (338 K, 30 min, $30 \text{ cm}^3 \text{ g}_{\text{zeolite}}^{-1}$) in an aqueous solution of 0.6 M NaOH or 0.3 M NaOH + 0.05 M TPABr for hz15 and hz140, respectively, followed by quenching in ice-water, filtration, and washing. The isolated solids were converted to the protonic form by ion exchange with aqueous NH₄NO₃ (0.1 M, 298 K, $100 \text{ cm}^3 \text{ g}_{\text{zeolite}}^{-1}$) in three consecutive steps for 12 h and subsequent calcination (873 K, 3 h, 2 K min^{-1} , $60 \text{ cm}^3 \text{ min}^{-1}$ air flow).

4.2.2. Catalyst Characterization

X-ray diffraction (XRD) was measured with a PANalytical X'Pert Pro diffractometer using Ni-filtered Cu K α radiation ($\lambda = 0.1541 \text{ nm}$). Solid-state ²⁷Al magic angle spinning nuclear magnetic resonance (MAS NMR) spectra, referenced to NH₄Al(SO₄)₂·12H₂O, were acquired on a Bruker Avance 400 MHz spectrometer using a spinning speed of 10 kHz, 2048 accumulations, and 90 pulses (2 μs length, 0.25 s recycle decay). X-ray fluorescence spectrometry (XRF) was conducted with an Orbis Micro XRF analyzer (EDAX) operated with a Rh source at 30 kV. Nitrogen sorption at 77 K was measured in a Quantachrome Quadrasorb SI analyzer after evacuation of the samples at 573 K for 6 h. Mercury intrusion was carried out in a Micromeritics Autopore IV 9510 instrument (contact angle = 140°, pressure equilibration time = 10 s). Temperature-programmed desorption of NH₃ was carried out in a Micromeritics AutoChem II 2920 (473–873 K, 10 K min^{-1}). Prior to analysis, the samples were degassed

(873 K, 3 h, 20 cm³ min⁻¹ He), and ammonia was adsorbed in three consecutive saturation (10 vol.% NH₃ in 20 cm³ min⁻¹ He, 30 min) and purging (20 cm³ min⁻¹ He, 1 h) steps at 473 K. Fourier transform infrared spectroscopy of adsorbed pyridine was conducted using a Bruker IFS 66 spectrometer. After evacuation at 673 K for 4 h, wafers of pressed sample were saturated with pyridine vapor, and further evacuated at 473 K for 30 min. Spectra were acquired in the range of 4000–650 cm⁻¹ with a nominal resolution of 4 cm⁻¹ and the coaddition of 31 scans. The concentrations of Brønsted (c_B) and Lewis (c_L) acid sites were determined from the bands at 1545 and 1445 cm⁻¹, respectively, using extinction coefficients of 1.67 and 2.94 cm μmol⁻¹, respectively.^[197] Thermal gravimetric analysis was performed in a Mettler Toledo TGA/SDTA851e microbalance. Focused ion beam-scanning electron microscopy (FIB-SEM) of resin-embedded extrudates was performed with a Zeiss NVision 40 instrument using energy-selective backscattered electron detection (2 kV). SEM and TEM images were taken with a Zeiss Gemini 1530 FEG microscope (5 kV) and a FEI Tecnai F30 microscope (300 kV), respectively. Confocal fluorescence microscopy was undertaken using a Zeiss LSM 510 META laser scanning microscope with a Plan-Apochromat ×63/1.4 oil objective lens. Detection ranges of 500–550 nm and 660–737 nm were used to record stimulated fluorescence, following illumination by monochromatic lasers of 488 nm and 633 nm, respectively. Sample preparation included heating the extrudates for 15 min to 373 K, followed by addition of thiophene (Merck Chemicals), and quenching after 10 s of reaction. Nile blue (85%, Sigma Aldrich) dissolved in ethanol was subsequently added to the extrudates at ambient temperature. Finally, the dry extrudates were then resin-embedded (LR White) and cut with a microtome to obtain a flat surface.

4.2.3. Diffusion Studies

The adsorption of 2,2-dimethylbutane (>99%, ABCR) was studied in an Intelligent Gravimetric Analyzer (IGA 002, Hiden Isochema). Prior to analysis, the powder or extrudate (30 mg) was outgassed in situ (573 K, 4 h, 10⁻⁵ bar). At a desired temperature (358 K), the sample was subjected to a pressure step (0.1 mbar) of 2,2-dimethylbutane vapor, and the weight change was continuously recorded until equilibrium was reached.

4.2.4. Methanol-to-Hydrocarbons Testing

The conversion of methanol over the powder (200–400 μm sieve fraction) and extrudate (2 mm in diameter, 4 mm in length) catalysts was evaluated in a Microactivity-Reference unit (PID Eng&Tech) at 623 or 723 K and ambient pressure. The catalysts (0.5 g with respect to the zeolite mass, mixed with 1.5 g SiC of 400–600 μm diameter) were loaded in a fixed-bed, continuous-flow reactor (13.5 mm i.d.) and heated for 1 h at 773 K under a N_2 flow prior to reaction. The temperature was recorded with a thermocouple coaxially positioned in the center of the reactor in contact with the catalyst. Methanol (99.9%, Sigma Aldrich) was introduced via an HPLC pump (307 5-SC-type piston pump, Gilson) using N_2 as the carrier gas to attain the desired weight-hourly space velocity with respect to the zeolite content ($9.5 \text{ g}_{\text{methanol}} \text{ g}_{\text{zeolite}}^{-1} \text{ h}^{-1}$ unless otherwise specified). The dependence of conversion, defined as the fraction of light oxygenates (methanol and dimethyl ether) consumed during the reaction on a carbon mole basis (C mol.%), on the WHSV was assessed by varying the mass of the catalyst. The product mixture was analyzed by online gas chromatography (GC 7890A, Agilent Technologies) using a HP PLOT Q capillary column and a flame ionization detector. Individual products were identified and lumped together according to retention times established by comparison with pure standards, and carbon balances of between 96 and 99% were usually achieved. Catalyst regeneration was accomplished by flowing air ($50 \text{ cm}^3 \text{ min}^{-1}$) at 823 K for 3 h over the extrudate bed.

4.3. Results and Discussion

4.3.1. Characterization of Technical ZSM-5 Catalysts

Figure 4.1 illustrates the protocol used to shape conventional (cz40) and hierarchical ZSM-5 (hz40) powders with one of four commercial binders: (i) an acid-dispersible boehmite (bo) with a nominal particle size of 80 nm, (ii) a hydrophilic precipitated silica (si) with a nominal agglomerate size of 7.5 μm , (iii) a high-quality attapulgite clay (at) with an agglomerate size (as-received) of 30 μm , and (iv) a high-quality kaolin clay (ka) of 20 μm particle size. Herein, the greater compositional complexity of the natural clays is noteworthy:

Table 4.1. Characterization and performance data of the pure powder and extruded zeolite catalysts.

Sample	Form ^a	V_{micro}^b [cm ³ g ⁻¹]	S_{meso}^b [m ² g ⁻¹]	V_{meso}^c [cm ³ g ⁻¹]	V_{macro}^e [cm ³ g ⁻¹]	c_B^f [μmol g ⁻¹]	c_L^f [μmol g ⁻¹]	Lifetime ^g [h]	$S(C_{2-4})^g$ [Cmol.%]	$S(C_{6-8})^g$ [Cmol.%]
cz40	P	0.14	82	0.13 (0.04) ^d	na	174	35	20	39	15
hz40	P	0.12	183	0.49 (0.33)	na	212	52	41	40	10
hz40-si	E	0.07	144	0.49 (0.76)	0.15	50	52	12	33	12
hz40-bo	E	0.06	180	0.49 (0.40)	0.10	96	161	21	27	12
hz40-ka	E	0.07	94	0.27 (0.25)	0.29	190	70	52	42	10
hz40-at	E	0.06	159	0.48 (0.44)	0.19	113	185	71	51	5
hz40-at	E ^h	0.06	155	0.46 (0.44)	0.19	93	160	73	51	4

^a Powder (P) and extrudate (E), zeolite-binder admixtures comprise 1:1 dry mass ratio; ^b t -plot method; ^c $V_{\text{meso}} = V_{\text{pore}} - V_{\text{micro}}$; ^d In parenthesis, volume of Hg intruded into pores of 3.7–50 nm diameter; ^e Volume of Hg intruded into pores >50 nm in diameter ^f Concentration of Brønsted (c_B) or Lewis (c_L) acid sites derived from the IR study of adsorbed pyridine; ^g MTH reaction studied at $T = 723$ K, $P = 1$ bar, and $\text{WHSV} = 9.5 \text{ g}_{\text{methanol}} \text{ g}_{\text{zeolite}}^{-1} \text{ h}^{-1}$; ^h Sample regenerated following deactivation to 70% in the MTH reaction.

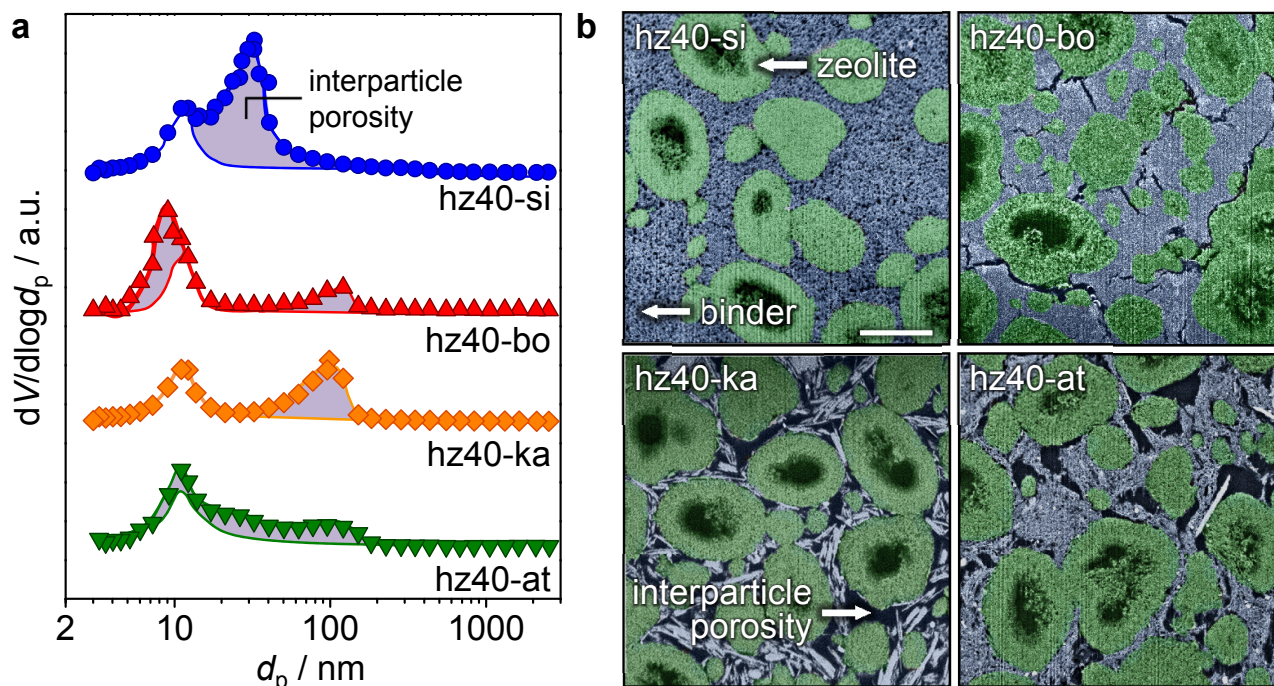


Figure 4.2. (a) Pore size distributions derived by Hg intrusion of physical (lines) and extruded (symbols) admixtures of the binder and hierarchical ZSM-5. (b) Colored backscattered electron micrographs of FIB-prepared cross-sections of the binder-containing hierarchical ZSM-5 extrudates. The scale bar represents 2 μm and applies to all images.

semiquantitative analysis by X-ray fluorescence spectroscopy revealed a composition of 17.9 Al_2O_3 /53.9 SiO_2 /14.2 MgO /3.7 P_2O_5 /1.1 K_2O /2.6 CaO /0.4 TiO_2 / 6.1 Fe_2O_3 for attapulgite and 49.1 Al_2O_3 /50.3 SiO_2 /0.1 TiO_2 /0.5 Fe_2O_3 for kaolin, respectively. Detailed characterization of the thermal stability of the binders and of their crystallinity, porosity, acidity, and MTH activity after calcination at 873 K is provided in Table A.1 and Figure A.9. The porous and acidic properties of the conventional and hierarchical ZSM-5 zeolites applied in this study are reported in Table 4.1. Pertinently, alkaline treatment of cz40 more than doubled the mesopore surface area in hz40 and led to an 8-fold increase in the accessible mesopore volume determined by Hg intrusion. On the other hand, the hierarchical sample displayed a slightly enhanced concentration of Brønsted and Lewis acid sites.

The organization of zeolite and binder particles upon agglomeration by extrusion defines an additional interparticle meso-macropore network, which can be quantitatively assessed by mercury intrusion (Figure 4.2 and Table 4.1) and visualized by focused ion beam-scanning electron microscopy (Figure 4.2), as demonstrated in Chapter 3.^[180] Densely packed structures, exhibiting the lowest macropore volume and smallest average interparticle pore diameter,

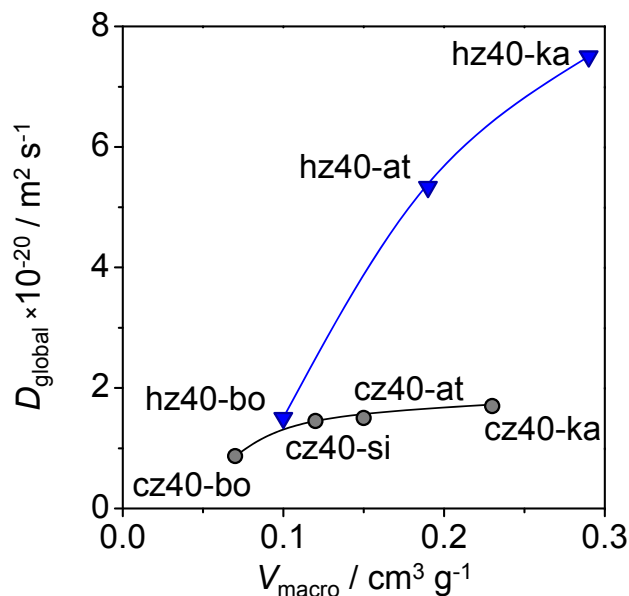


Figure 4.3. Global diffusion coefficients (D_{global}) of 2,2-dimethylbutane in binder-containing conventional (circles) and hierarchical (triangles) ZSM-5 extrudates as a function of macropore volume at 358 K and 0.1 mbar. The trend lines are drawn for guidance only.

resulted upon shaping the hierarchical ZSM-5 with the binders of the smallest particle size, for example, the dispersed boehmite. In contrast, structuring with the larger platelike particles of kaolin led to the most open arrangement. Extrusion can induce significant morphological changes in the binders, as can be seen by comparison with the electron micrographs of the single phase powders (Figure A.9.e). For example, the large spherical agglomerates (30 μm in diameter) observed in the as-received attapulgite powder were dispersed into needle-like nanoparticles wrapped around the zeolite particles in the extrudate. The likelihood of such dispersion could be assessed by laser diffraction analysis of the particle size distribution before and after ultrasonic treatment in water (Figure A.10).

The adsorption properties of the shaped zeolite catalysts were characterized by measuring the transient uptake curves of 2,2-dimethylbutane at varying temperatures, adopting a methodology recently developed by our group.^[198] This probe molecule is ideal for ZSM-5 zeolites because it exhibits a kinetic diameter (0.61 nm) similar to the diameter of an MFI micropore (0.56 nm), decreasing the rate of uptake. In that study, an almost four-times higher global diffusivity (D_{global}) was evidenced over the hierarchical with respect to the conventional ZSM-5 powder at 358 K and 0.1 mbar, which was correlated with the additional intracrystalline mesoporosity. Consistent with the proportional contribution of the component phases, a

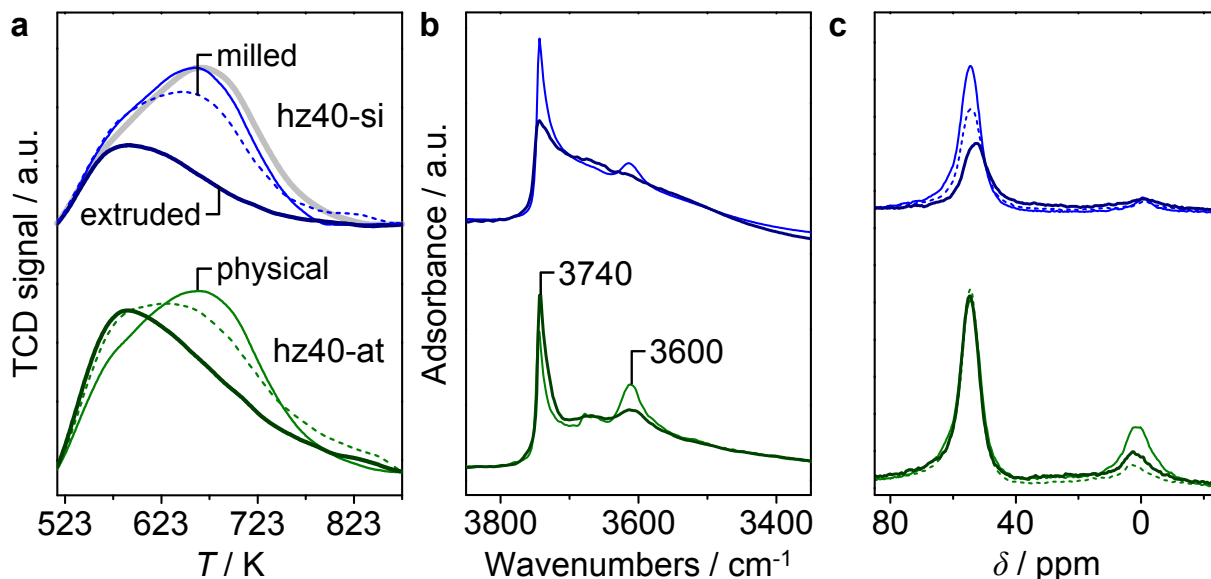


Figure 4.4. (a) NH_3 -TPD profiles, (b) FTIR spectra in the OH-stretching region, and (c) ^{27}Al MAS NMR spectra of physical (thin line), extruded (thick line), and milled (dashed line) hz40-si (top) and hz40-at (bottom) admixtures normalized to the zeolite content. The thick gray line in part a indicates the NH_3 -TPD profile of the single-phase hz40 powder.

50% reduction in D_{global} was observed in the physical mixture, resulting upon inclusion of an attapulgite binder hz40-at. Moreover, the further drop in the adsorption kinetics from 7.5×10^{20} to $5.3 \times 10^{20} \text{ m}^2 \text{ s}^{-1}$ evidenced upon extrusion is consistent with the longer path length of diffusion within the shaped body. It is known that the mass transfer within shaped zeolite bodies can be dominated by diffusion in the macropores, representing up to 80% of the global mass transfer, particularly at high temperature.^[198,199] In fact, a clear dependence on V_{macro} was observed on comparison of the D_{global} determined at 358 K and 0.1 mbar for the conventional and hierarchical ZSM-5 extrudates prepared with different binders (Figure 4.3). Interestingly, a much larger variation in the adsorption kinetics was observed for the hierarchical zeolite catalysts, suggesting that the effectiveness of the intracrystalline mesopores at enhancing molecular transport is limited by densely packed structures, displaying interparticle porosity in the mesopore range.

Finally, evaluation of the acidic properties by the IR study of adsorbed pyridine evidenced reduced concentrations of Brønsted acid sites per gram of zeolite (c_{B}) in all of the shaped hierarchical ZSM-5 catalysts (Table 4.1), with hz40-ka > hz40-at > hz40-bo > hz40-si. Such losses could arise from either (i) the removal of Brønsted acid sites due to dealumination of the zeolite framework or (ii) their partial neutralization due to the ion exchange with mobile species.

For example, the latter has been previously reported in the case of sodium montmorillonite^[102] or kaolin clays.^[108] To further understand the variation in Brønsted acidity, the samples were further characterized by NH₃-TPD, FTIR, and ²⁷Al MAS NMR, as shown for selected samples in Figure 4.4. The most prominent drop in c_B , to less than 1/3 of that expected based on the proportional contribution of the zeolite and binder phases, was observed over the silica-bound zeolites. Herein, the decline in the contribution above 700 K in the NH₃-TPD profile, the disappearance of the band at 3600 cm⁻¹ in the IR spectrum, and the reduction in the peak intensity associated with tetrahedrally coordinated Al species (54 ppm) in the ²⁷Al MAS NMR spectrum indicated that the loss of Brønsted sites occurred as a result of dealumination of the zeolite framework. Nonetheless, the cause of this effect remains unclear, and few studies have addressed variations in the acidity of zeolite catalysts when shaped with silica binders.^[101] No such impact was observed in the physical mixture of these silica and zeolite phases prepared as a reference. Determination of the origin of the reduced c_B was more complex for hz40-bo because of the presence of aluminum in the binder. Previously, this has been linked to the partial neutralization of the Brønsted acid site as a result of the migration of aluminum species from the binder.^[101]

Comparatively, the clay binders interacted distinctly with the zeolite. In the case of kaolin, no evidence of a chemical interaction was observed; the acidic properties of hz40-ka closely matched those expected on the basis of the characteristics of the pure components. On the other hand, the extruded hz40-at exhibited a lower c_B , mirrored by a decrease in the high temperature contribution in its NH₃-TPD profile and the disappearance of the Brønsted hydroxyl stretch (3600 cm⁻¹) in the FTIR spectra (Figure 4.4a-b). However, no evidence of dealumination was observed on comparison of the shaped catalyst with respect to the physical mixture of the pure components by ²⁷Al MAS NMR (Figure 4.4c), suggesting that this loss was due to partial neutralization of the acid sites.

Moreover, to obtain a greater spatially-resolved insight into the distribution of acid sites within the technical body, confocal laser scanning microscopy (CLSM) coupled with selective staining methods was studied as a complementary tool by which to characterize acidity changes in zeolite catalysts.^[180] The value of this technique was recently demonstrated to visualize the

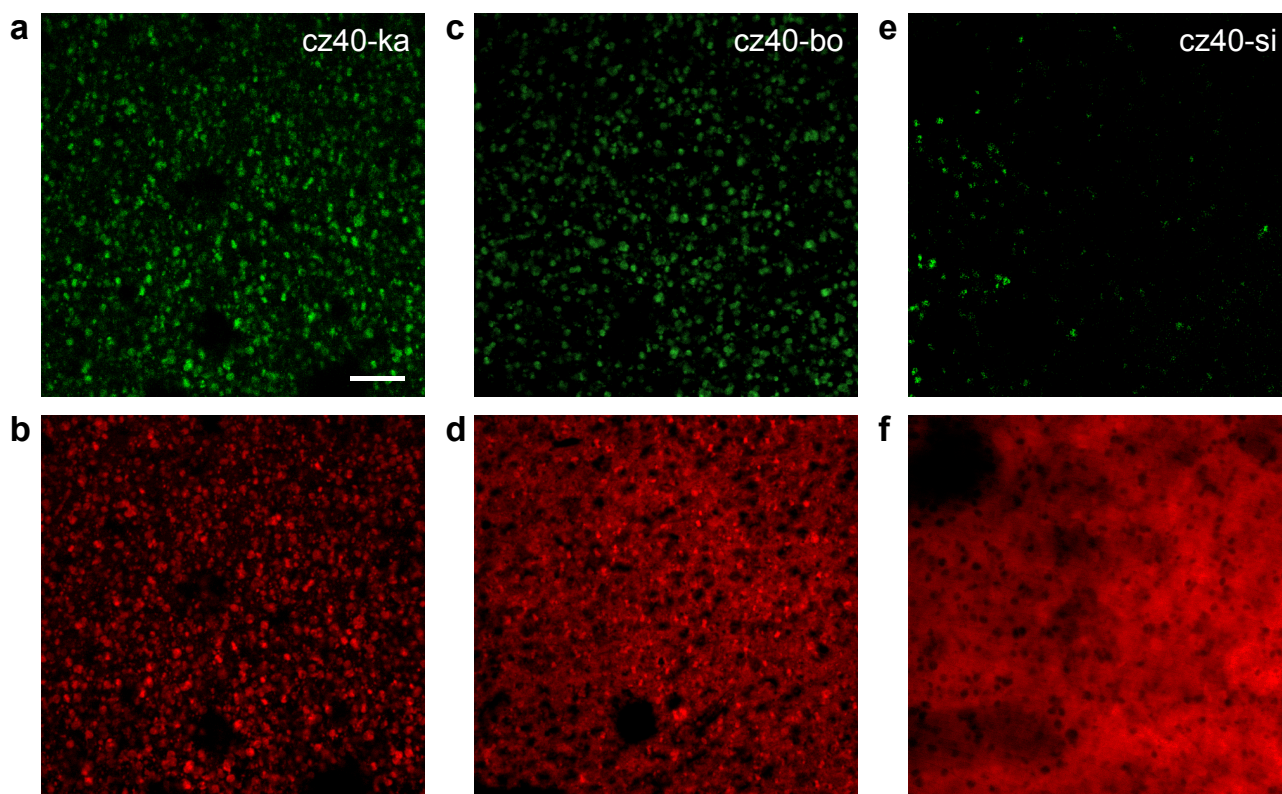


Figure 4.5. Confocal laser scanning microscopy images of embedded cross-sections of conventional ZSM-5 extrudates bound by (a,b) kaolin, (c,d) boehmite, or (e,f) silica after reaction with thiophene at 373 K (top row, $\lambda_{\text{excitation}} = 488$ nm, detection 500–550 nm) and staining with Nile-Blue (bottom row, $\lambda_{\text{excitation}} = 633$ nm, detection 662–737 nm). The scale bar represents 20 μm and applies to all images.

activity of individual FCC catalyst particles monitored at different life stages of deactivation.^[163] Herein, the conventional ZSM-5 bodies bound with kaolin, silica, or boehmite (1:4 zeolite-binder ratio) were first stained with thiophene, a molecule that reacts upon interaction with Brønsted acid sites to form green fluorescent products, and subsequently with Nile Blue. The latter is too bulky to enter the micropores and fluoresces red when illuminated, thus enabling the discrimination of the external surface of the zeolite and binder particles (Figure 4.5). Here, it is noteworthy that the zeolite content in the technical bodies was reduced to enhance the spatial resolution between the individual zeolite particles. An overall decrease in the more intense green fluorescent domains of the zeolite particles from $\text{cz40-ka} > \text{cz40-bo} > \text{cz40-si}$ was evidenced, which could be correlated with a reduced concentration of Brønsted acid sites following interaction between the zeolite and binder (*vide supra*). Moreover, the differences in the particle packing in the technical body, reflecting the distinct binders, is clearly evident, in agreement with the observations made by FIB-SEM.

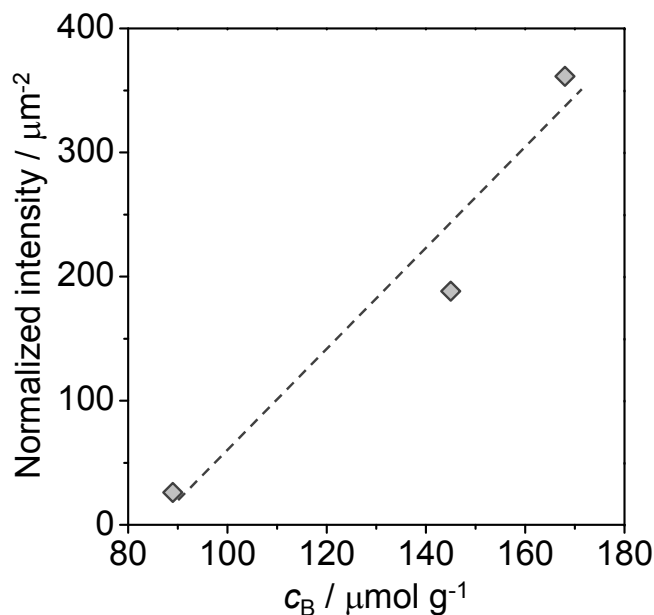


Figure 4.6. Correlation between the average fluorescence intensity normalized per unit area obtained by CLSM of embedded cz40-ka, cz40-bo, and cz40-si (zeolite-binder ratio 1:4) and the amount of Brønsted acid sites determined by IR study of adsorbed pyridine.

A more quantitative insight into the fluorescence intensities was acquired by calculation of the average fluorescence intensity of the zeolite particles normalized per unit area. By first setting an intensity threshold to remove the fluorescent signal from the background and from zeolite particles in close proximity (residual fluorescence), the average fluorescence intensity of a sample was determined. Due to variation in the zeolite particle distribution within the shaped body, the intensity was normalized to the corresponding area of zeolitic particles. Accordingly, the normalized intensity was found to correlate almost linearly with c_B (Figure 4.6), confirming the validity of our approach.

4.3.2. MTH Performance of Technical Zeolite Catalysts

The performance of the zeolite extrudates relative to that of the pure powders was evaluated in the conversion of methanol to hydrocarbons at 723 K (Figure 4.7a) and 623 K (Figure 4.7b). The mass of the composite catalyst was doubled compared with that of the single phase materials to achieve an equivalent weight hourly-space velocity with respect to the amount of zeolite during initial tests ($\text{WHSV} = 9.5 \text{ g}_{\text{methanol}} \text{ g}_{\text{zeolite}}^{-1} \text{ h}^{-1}$). The catalyst lifetime, defined as the time for which the conversion of oxygenates (methanol and dimethyl ether) exceeded 90%, and the selectivity to $\text{C}_{2-4}^{\text{=}}$ olefins ($S(\text{C}_{2-4}^{\text{=}})$) and C_{6-8} aromatics ($S(\text{C}_{6-8})$) exhibited at

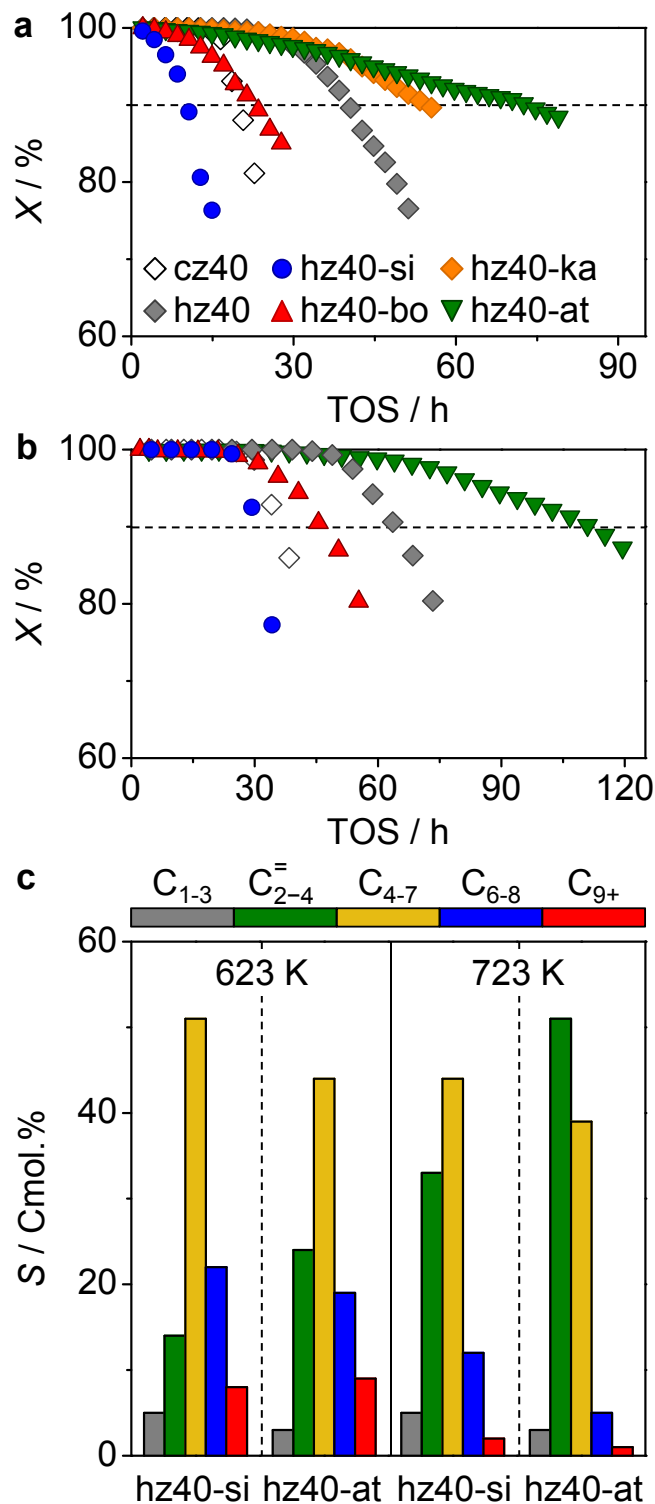


Figure 4.7. Methanol conversion *vs.* time-on-stream measured at (a) 723 and (b) 623 K, and (c) corresponding product selectivities over extruded admixtures of hierarchical ZSM-5 and silica, boehmite, or clay binders. The single-phase conventional (open diamond) and hierarchical (solid diamond) zeolite powders are shown as reference. The dashed line indicates the degree of conversion at which a cycle time was defined. Other conditions: $P = 1$ bar and $\text{WHSV} = 9.5 \text{ g}_{\text{methanol}} \text{ g}_{\text{zeolite}}^{-1} \text{ h}^{-1}$.

723 K are summarized in Table 4.1, and a detailed breakdown of the product distribution is provided in Table A.2.

Typical of the extensions previously reported over desilicated zeolites,^[159,160,180,195] the hierarchical ZSM-5 powder exhibited a lifetime double that of the conventional zeolite at both temperatures (41 with respect to 20 h, respectively, at 723 K), and only minor differences in selectivity were noted. In comparison, wide variations in both the catalyst lifetime and selectivity were observed over the hierarchical ZSM-5 zeolite upon shaping with different binders, which could not be directly correlated with the porous or acidic properties determined in Section 4.3.1. Extrusion with silica or boehmite adversely affected both the catalyst lifetime and selectivity to light olefins, while promoting the formation of C₅₋₇ hydrocarbons. In the case of hz40-bo, a slightly increased production of light gases was consistent with the individual activity of the binder, which catalyzed the formation of CH₄ (Table A.1). Both the densely packed structures and the sharply reduced Brønsted acidity evidenced in these extrudates could be responsible for these inhibiting effects.

Comparatively, extrusion with kaolin, which induced the smallest deviation in the acidic properties and led to the most open pore structure, did not markedly alter the performance of the hierarchical zeolite. In stark contrast, despite also resulting in a largely reduced Brønsted acidity, the most promising result emerged upon shaping with attapulgite, which led to a 70% increased cycle time and a 25% higher light olefin selectivity (particularly to propene and butenes, Table A.2) with respect to the pure zeolite. As expected, the main impact of decreasing the temperature was to shift the selectivity from light olefinic to gasoline-range products (Figure 4.7c), and slower rates of deactivation were also evidenced over all samples. Nonetheless, the binders studied were found to have similar promoting or inhibiting effects at both reaction temperatures. Thus, despite exhibiting the greatest longevity, the hz40-at sample retained the highest C₂₋₄ selectivity (>20%) at 623 K.

Further insight into the differing impacts of the binders was obtained by analysis of the intrinsic activity (Figure 4.8) and the coking behavior (Figure A.11) of the hierarchical zeolite catalysts. Although a similar gradual decrease in the initial conversion was evidenced over the pure cz40 and hz40 powders with increasing methanol loading, a much steeper drop was seen

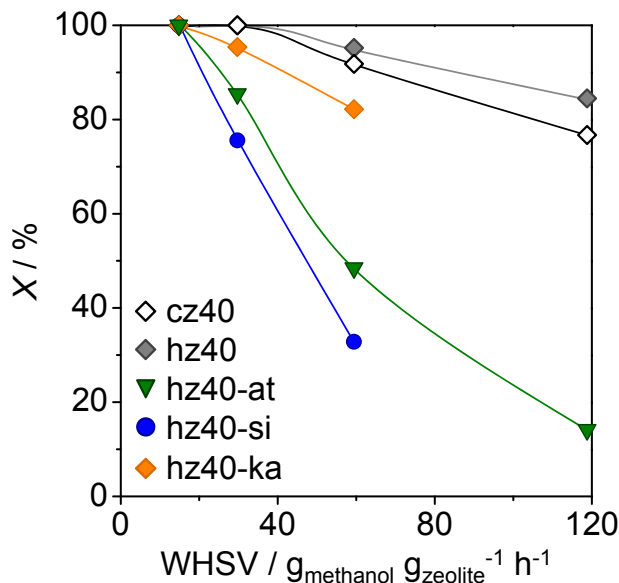


Figure 4.8. Methanol conversion *vs.* weight hourly-space velocity over conventional and hierarchical ZSM-5 powders and crushed extrudates of hz40 bound with attapulgite or silica. Conditions: $T = 723$ K, and $P = 1$ bar.

over the crushed silica and attapulgite bound extrudates. This observation is consistent with the lower c_B displayed by these samples and confirms that the 7-times difference in lifetime between hz40-si and hz40-at cannot be ascribed to a distinct intrinsic activity. Quantification of the coke content of the catalysts after use for a specific time in the MTH reaction revealed that higher amounts were deposited in the samples exhibiting shorter lifetimes. However, the interdependence between coke formation and the lifetime could also not be directly linked to the Brønsted acid site density and corresponding intrinsic activity of the zeolite catalysts. As suggested in section 4.3.1, this could reflect a different character of acid sites in the binder-containing samples, which may have differing strengths and accessibilities. For example, although Lewis acid sites generated on application of the boehmite binder catalyzed the formation of methane (and coke), which apparently adversely affects the performance of zeolite alumina composites, no such impact is expected due to the sites that catalyze the dehydration of methanol over the clay binders. Furthermore, the coking behavior is likely to depend on the interplay between multiple parameters. It is known that binders can also be influential during the high temperature regeneration of shaped zeolites.^[105] The reusability of the attapulgite-hierarchical ZSM-5 extrudate was confirmed, following oxidative regeneration in air (823 K, 3 h), by the equivalent performance exhibited in the second cycle to the fresh analogue (Table 4.1).

Table 4.2. Characterization and performance data of reference binder-containing hierarchical ZSM-5 admixtures.

Sample	Form ^a	c_B^b [$\mu\text{mol g}^{-1}$]	c_L^b [$\mu\text{mol g}^{-1}$]	Lifetime ^c [h]	$S(\text{C}_{2-4})^c$ [Cmol.%]	$S(\text{C}_{6-8})^c$ [Cmol.%]
hz40 _{Mg}	M	80	150	65	50	4
hz40-at	M	139	174	80	53	5
hz40-at _{HCl}	M	161	142	57	45	5
hz40-at _{HCl}	PM	195	70	51	41	11
hz40-at _{IE}	M	149	158	70	48	5
hz40-ka	M	145	75	48	41	10
hz40-ka _{Mg}	M	85	189	99	56	4

^a Milled (M) and physical (PM) zeolite binder admixtures; ^b Concentration of Brønsted (c_B) or Lewis (c_L) acid sites derived from the IR study of adsorbed pyridine; ^c MTH reaction studied at $T = 723$ K, $P = 1$ bar, and $\text{WHSV} = 9.5 \text{ g}_{\text{methanol}} \text{ g}_{\text{zeolite}}^{-1} \text{ h}^{-1}$.

4.3.3. Zeolite-Binder Interactions

Several additional steps were taken to distinguish the possible origins (physical or chemical) of the promoting effects evidenced over the MFI catalysts upon shaping with attapulgite. First, the performance of a differently treated hz40 at admixture was evaluated to determine under which conditions the property variation occurred (Table 4.2). Compared with the large extension evidenced over the extruded sample, only a slightly increased cycle time was observed over an hz40-at physical mixture with respect to that of the hz40 powder (50 with respect to 41 h, respectively). In contrast, if the hz40-at wet paste applied during extrusion was instead ball milled, a cycle time similar to that of the shaped sample (80 h) resulted. Milling did not adversely impact the crystallinity or the porosity of the zeolite phase. Consistent with the variation observed in the hz40-at extrudates, the milled sample exhibited a reduced number of Brønsted coupled with an increased number of Lewis acid sites. The comparable behavior of the milled (powder) and extruded samples demonstrates that the promoting effect of the attapulgite binder derives from a chemical interaction with the zeolite, and is not significantly impacted by mass transfer effects due to the physical agglomeration of the component phases within the shaped body. In this regard, the application of water or mechanical force (or both) is necessary to induce the property alteration.

Table 4.3. Chemical analysis of as-received and HCl-treated attapulgite, and hierarchical ZSM-5 before and after treatment with phase-separated attapulgite, hz40_{sep}.

Sample	Composition [wt.%]							
	MgO	Al ₂ O ₃	SiO ₂	P ₂ O ₅	K ₂ O	CaO	TiO ₂	Fe ₂ O ₃
at	14.2	17.9	53.9	3.7	1.1	2.6	0.4	6.1
at _{HCl}	11.5	19.6	61.1	0.0	1.2	0.2	0.4	6.0
hz40	0.0	6.4	93.7	0.0	0.0	0.0	0.0	0.0
hz40 _{sep}	0.36	6.4	93.0	0.0	0.06	0.06	0.10	0.10

As mentioned in Section 4.3.1, the as-received attapulgite contains several species (*e.g.*, Mg, Si, Al, P, K, Ca, Ti, Fe) that could interact with the zeolite (Table 4.3). To further understand their potential effects, both the influence of purifying the attapulgite clay by acid treatment, a typical approach for the removal of soluble metals present in clays,^[200] and of doping the kaolin binder with alkaline oxides present in the attapulgite (*e.g.*, MgO) were assessed. Herein, ball milling was applied as a rapid method to screen for zeolite-binder interactions with smaller sample quantities. Losses of Brønsted acid sites originating as a result of ion exchange should be preventable, if the responsible cationic species could be eliminated from the clay binder prior to shaping. Acid treatment of the attapulgite with 1 M HCl solution for 1 h (at_{HCl}), decreased the concentration of magnesium, and completely removed calcium and phosphorus from the sample (Table 4.3). When milled with the hierarchical ZSM-5, the promoting effect of at_{HCl} was much less significant than that of at, resulting in an MTH lifetime of 57 h with respect to 80 h. Consistently, c_B was less prominently reduced in the milled hz40-at_{HCl} (Figure 4.4a), suggesting a considerable decline in the amount of mobile species.

The concept of ion exchange of the Brønsted acid sites could be supported by verifying the reversibility of the interaction.^[102] Accordingly, we re-exchanged the milled hz40-at admixture by treatment with ammonium nitrate, which decreased the MTH lifetime from 80 to 70 h over hz40-at_{IE}, further corroborating the link with the exchangeable cations. The strongest evidence for the identity of the responsible mobile species was gained by slowly flushing water through a vertical column filled with phase-separated attapulgite (top) and hierarchical ZSM-5 (bottom). This permitted the water-mediated migration of soluble ions from the binder to the zeolite without their direct contact. XRF analysis revealed the introduction of a significant amount of

magnesium into hz40 after the treatment (Table 4.3).

Assuming that the promoting action of the attapulgite binder on the MTH performance of ZSM-5 zeolites originates from the neutralization of Brønsted acid sites due to exchange with Mg^{2+} , we expected that this result could be extrapolated to other systems. To test this hypothesis, we milled wet MgO-doped admixtures of the kaolin and hierarchical ZSM-5 (Figure 4.9a). No major lifetime enhancement was previously evidenced over the hz40-ka extrudate with respect to that observed over the pure hierarchical zeolite (*vide supra*). As a reference, the milled hz40-ka admixture was found to exhibit a lifetime equivalent to that of its physically mixed analogue (48 h), confirming that the ball milling itself did not alter the catalytic performance. Strikingly, the addition of MgO more than doubled the cycle time (100 h) with respect to the milled hz40-ka, which is consistent with the reduced Brønsted and increased Lewis acid site density exhibited by this sample (Table 4.2). Comparison of the average product distribution of the milled hz40-ka_{Mg} evidenced a similar substantial increase of up to 56% in light olefin selectivity, as previously observed in the attapulgite-containing zeolite catalysts (Figure 4.9b). Moreover, a similar behavior in catalyst lifetime and selectivity was observed over the hierarchical ZSM-5 powder when doped with MgO (Table 4.2), consistent

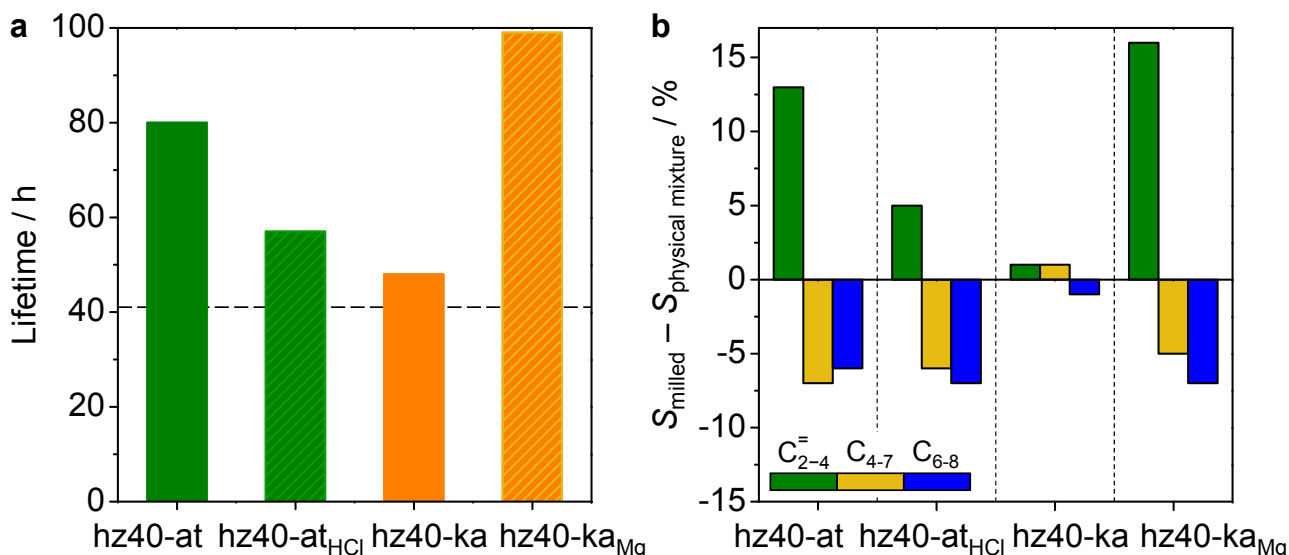


Figure 4.9. (a) MTH lifetime over milled hierarchical ZSM-5 admixtures with attapulgite, HCl-treated attapulgite, kaolin, and MgO-doped kaolin, and (b) the difference in average product selectivity with respect to the corresponding physical mixtures. The lifetime of the single-phase hierarchical ZSM-5 powder is indicated by the dashed line in part (a). Conditions: $T = 723$ K, $P = 1$ bar, and $\text{WHSV} = 9.5 \text{ g}_{\text{methanol}} \text{ g}_{\text{zeolite}}^{-1} \text{ h}^{-1}$.

with its expected promoting role. Prior studies have reported an enhanced olefin selectivity over MgO-modified ZSM-5 zeolites in the MTH reaction.^[191,192]

Finally, it was attempted to rationalize the impact of zeolite-binder interactions of both physical and chemical origin on the MTH performance over all physical, extruded, and milled hierarchical ZSM-5 admixtures tested. Analysis of the MTH lifetime as a function of the Brønsted acidity (Figure 4.10a) revealed two distinct behaviors resulting from zeolite-binder interactions: (i) that an improved coke tolerance and light olefin selectivity could be achieved through the partial and reversible neutralization of Brønsted acid sites through the migration of soluble alkaline oxide species present in clay binders, and (ii) that thermally or mechanically induced dealumination of the zeolite framework appears to be detrimental to the performance, reducing the cycle time significantly. In the first case, the promoting effects, observed over kaolin-containing zeolite catalysts before and after MgO-doping (Figure 4.10b), demonstrate that performance enhancements are achievable by solely varying the zeolite acidity because the porous properties were unaltered. However, in the second case, the possible contributions

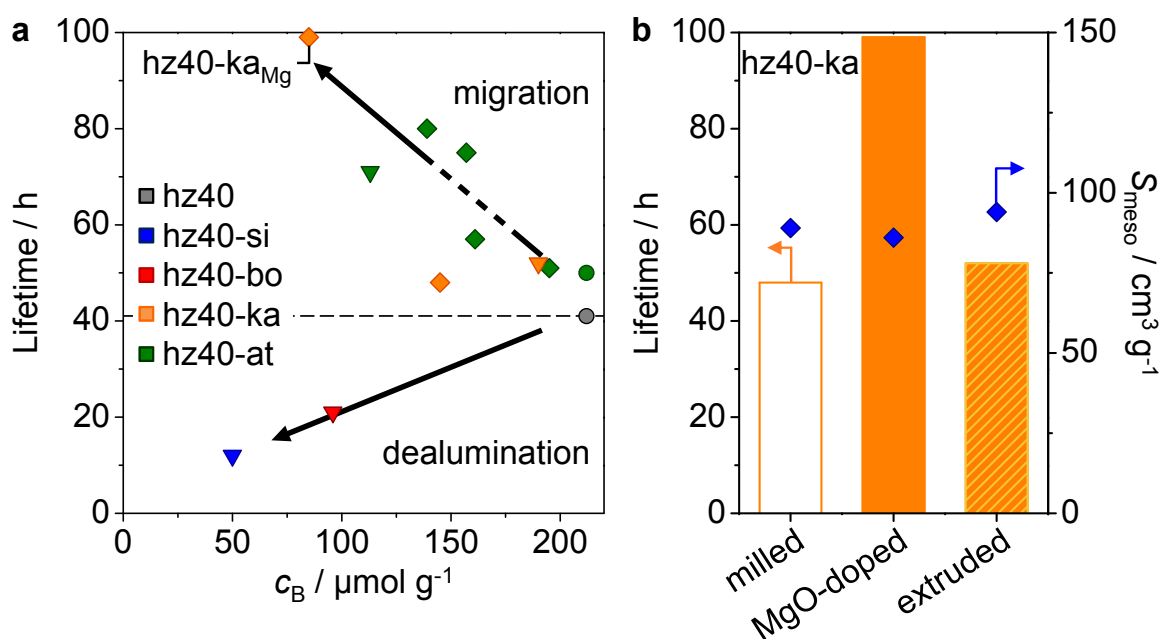


Figure 4.10. (a) Impact of the amount of Brønsted acid sites on the MTH lifetime exhibited by the binder-containing hierarchical ZSM-5 admixtures in physical (circle), extruded (triangle), and ball milled (diamond) form. The dashed line indicates the lifetime of the single-phase hierarchical ZSM-5, which possesses the highest intrinsic c_B . (b) Comparison of the MTH lifetime and mesopore surface area (S_{meso}) of extruded, milled, and MgO-doped hz40-ka admixtures evidences the lack of direct correlation between these two parameters. Conditions: $T = 723 \text{ K}$, $P = 1 \text{ bar}$, and $\text{WHSV} = 9.5 \text{ g}_{\text{methanol}} \text{ g}_{\text{zeolite}}^{-1} \text{ h}^{-1}$.

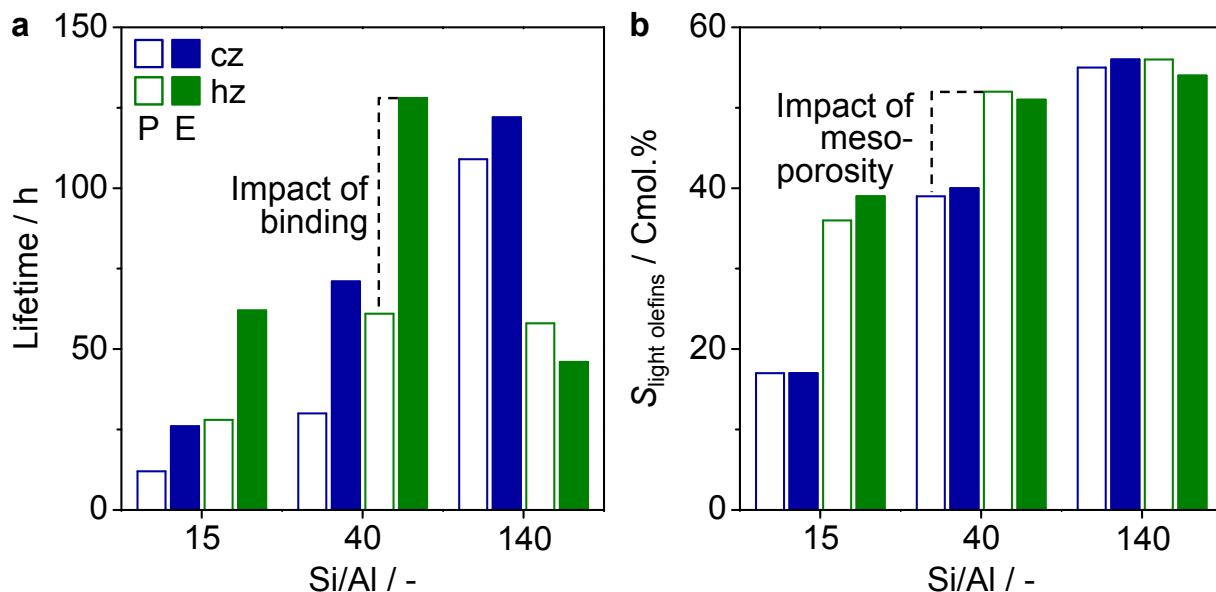


Figure 4.11. (a) MTH lifetime and (b) average light olefin selectivity evidenced over conventional ZSM-5 zeolite powders of different Si/Al ratio with respect to their hierarchical analogues and to the attapulgite-bound counterparts. Conditions: $T = 723$ K, $P = 1$ bar, and $WHSV = 4.8$ $\text{g}_{\text{methanol}} \text{g}_{\text{zeolite}}^{-1} \text{h}^{-1}$.

of porosity cannot be completely neglected because these samples correspond to the catalysts shaped with boehmite and silica binders, the densely packed structures of which could also contribute to the higher amounts of coke formed and shorter MTH lifetimes.

4.3.4. Interplay between Zeolite Composition, Mesoporosity, and Binder Effects

It is well known that in addition to the influence of porosity, the MTH lifetimes of single-phase ZSM-5 zeolites depends on the Si/Al ratio of the framework and, consequently, the relative concentration of Brønsted acid sites.^[182,183,187] The latter could also impact the interaction of the zeolite with binders applied during shaping. To generalize the significance of the performance benefits that we had observed upon both mesoporosity introduction and shaping the ZSM-5 zeolite with the attapulgite binder, we verified the potential impact of varying the zeolite composition. For this purpose, ZSM-5 zeolites with nominal Si/Al ratios of 15 and 140 (cz15 and cz140, respectively) and their hierarchical analogues (hz15 and hz140, respectively) obtained by desilication as well as the corresponding attapulgite-bound extrudates (*e.g.*, hz15-at) were tested in the MTH reaction at WHSV of $4.8 \text{ g}_{\text{methanol}} \text{g}_{\text{zeolite}}^{-1} \text{h}^{-1}$. It is noteworthy that the comparative evaluation at the higher WHSV ($9.5 \text{ g}_{\text{methanol}} \text{g}_{\text{zeolite}}^{-1} \text{h}^{-1}$) applied in the previous section was not possible because complete conversion was not achieved over the high-

Table 4.4. Characterization and performance data of the pure powder and extruded zeolite catalysts.

Sample	Form ^a	V_{micro}^b [cm ³ g ⁻¹]	S_{meso}^b [m ² g ⁻¹]	V_{meso}^c [cm ³ g ⁻¹]	c_B^d [μmol g ⁻¹]	c_L^d [μmol g ⁻¹]	Lifetime ^e [h]	$S(\text{C}_{2-4})^e$ [Cmol.%]	$S(\text{C}_{6-8})^e$ [Cmol.%]
cz15	P	0.15	52	0.08	304	43	12	17	24
hz15	P	0.15	136	0.40	152	124	36	17	25
cz15-at	E	0.07	93	0.22	189	107	28	36	17
hz15-at	E	0.07	138	0.33	78	141	68	39	13
cz140	P	0.14	66	0.21	36	7	109	54	7
hz140	P	0.12	185	0.33	38	23	122	56	4
cz140-at	E	0.07	98	0.31	24	47	58	56	3
hz140-at	E	0.06	172	0.35	21	63	46	54	4

^a Zeolite binder 1:1 dry mass ratio; ^b *t*-plot method; ^c $V_{\text{meso}} = V_{\text{pore}} - V_{\text{micro}}$; ^d Concentration of Brønsted (c_B) or Lewis (c_L) acid sites derived from the IR study of adsorbed pyridine; ^e MTH reaction studied at $T = 723$ K, $P = 1$ bar, and $\text{WHSV} = 9.5$ Gmethanol Gzeolite⁻¹ h⁻¹.

silica zeolite catalysts under those conditions. Nonetheless, a 9-fold extended lifetime was observed over the conventional ZSM-5 when increasing the Si/Al from 15 to 140 (12 *vs.* 109 h, respectively).

Interestingly, the lifetime enhancement evidenced over the series of hierarchical analogues hz15, hz40, and hz140 was reduced with an increase in the Si/Al ratio from 3 to 2.4 to 1.2-times, respectively, suggesting that the effectiveness of mesoporosity development in MTH is lower in the case of high-silica zeolites (Figure 4.11a). Since both hz140 and hz40 possess almost equivalent porous properties (Table 4.4), the different resistance to deactivation appears to be more strongly related to the relative acidity of the conventional and hierarchical zeolites (Table 4.1 and 4.4), and related activity.

Extrusion with attapulgite further increased the MTH lifetime of hz15-at with respect to hz15 by a factor of 1.8, in agreement with the enhancement achieved over hz40-at (*vide supra*). However, a similar promoting effect was not observed in the case of Si/Al = 140, significantly reducing the lifetime of hz140-at with respect to hz140. As expected, both hz15-at and hz140-at exhibited a diminished c_B relative to their respective powder analogues, (Table 4.4). However, although the zeolite-binder interaction proved beneficial for the Al-rich hz15-at, the density of acid sites was reduced so considerably in hz140-at that a lifetime of only 46 h was reached.

The initial light olefin selectivity was found to increase with varying Si/Al, consistent with a moderation in acid sites due to less aluminum in the zeolite framework (Figure 4.11b). Furthermore, although mesoporosity introduction exhibited only a very moderate improvement, binding hz15 with attapulgite more than doubled the C_{2-4}^- olefin selectivity. Interestingly, this effect became less significant with increasing Si/Al, reaching a plateau at 60% over hz140-at.

It is worth mentioning that the longest lifetime extensions observed at higher methanol loadings (*e.g.*, 100 h over hz40-ka_{Mg}; *vide supra*) put the binder-containing hierarchical zeolites in the same range as the high-silica zeolites in terms of cycle times while enabling twice the productivity. Consequently, the introduction of intracrystalline mesoporosity needs to be coupled with the optimization of binder selection to maximize lifetime and, thus, product yield, since both can give substantial improvements. Increasing the Si/Al ratio of the zeolite phase can also extend the cycle time but at the expense of the productivity.

4.4. Conclusions

Through systematic comparison of the individual components, and of physical, extruded, and milled zeolite-binder composites, the significant impact binders can have on the methanol-to-hydrocarbons performance of shaped hierarchical ZSM-5 zeolites has been demonstrated. As revealed by Hg porosimetry, the microscopic examination of internal cross-sections, and the gravimetric uptake of 2,2-dimethylbutane, the interaction of the larger particles of the clay binders yields technical bodies exhibiting superior macroporosity and mass transfer properties. Comparatively, distinct variations in the acid site density and speciation were evidenced by spectroscopic and temperature-programmed studies, depending on the binder applied. Although a decreased Brønsted acidity due to the reversible neutralization or dealumination of the zeolite framework reduced the intrinsic activity of the catalysts, no direct correlation was observed with the selectivity or the catalyst lifetime. Without optimization, the findings show that the combined chemical and physical effects of binders can match or even exceed those established on application of hierarchically-structured zeolites featuring intracrystalline mesopores and should be considered from the start of the catalyst development program. Attapulgite was the only binder that promoted the longevity and light olefin selectivity of the MFI catalysts, which was linked to the partial ion exchange with mobile Mg species. In contrast, extrusion with silica or boehmite adversely affected the performance of the zeolites. Ball milling was demonstrated as a complementary tool, enabling the accelerated screening of chemical interactions between the zeolite and binder at bench scale without the need for shaping. The identification of compositional and structural performance descriptors to selectively tune complex zeolite-binder interactions will enable more effective utilization of the diverse properties of these composite catalysts.

Structuring Zeolite Bodies for Enhanced Heat-Transfer Properties

5.1. Introduction

The performance of heterogeneously-catalyzed processes is inextricably linked with transport phenomena. Compared to the significant progress witnessed in the engineering of catalytic solids with enhanced mass-transfer properties through nano-structuring or the design of hierarchical pore networks (Chapters 2–4),^[116,201–203] strategies to optimize their thermophysical properties have received much less attention. In an industrial reactor (Figure 5.1a), thermal regulation is a multi-scale task encompassing both axial and radial profiles within the catalyst bed and local gradients within individual catalyst bodies (ensembles).^[204,205] Often, solutions for heat management remain heavily reliant on improving the efficiency of exchange at the reactor level, through the choice of reactor technology and/or process conditions.^[206–209] Aside from potentially catastrophic risks as thermal runaway, inefficient heat exchange can accelerate catalyst deactivation due to increased coking or irreversible degradation of the active phase, increase energy demands, and restrict space-time yields,^[210,211] bringing major economic and environmental incentives to optimize the thermal control by other means.

Of the basic modes of heat transfer,^[212,213] conduction via microscopic diffusion presents a wide window for improved control by materials design. As highly conductive materials, metals as copper,^[214] ceramics as silicon carbide,^[215,216] boron nitride^[216] or aluminum nitride,^[217] and carbons as graphite,^[218] carbon nanotubes^[219,220] or graphene,^[221] could be integrated for this purpose. Their use as structured catalyst supports (monoliths, foams, *etc.*) attract great interest to avoid the development of high local temperature gradients within catalysts applied in highly exo-/endothermic reactions, as the partial oxidation of methane,^[222] steam cracking/reforming,^[223] Fischer-Tropsch synthesis,^[224] and methanol-to-

hydrocarbons,^[225] as well as during subsequent oxidative regeneration (coke burn off)^[222,223]. However, although effective, this strategy often results in an unacceptably low catalyst loading per unit reactor volume. On the other hand, only exceptional works have considered the application of conductive additives to enhance the thermophysical properties of more widely applied structured zeolite geometries as pellets, extrudates, or granules.^[208,209] In this regard, it is worth emphasizing that it is not uncommon for technical zeolite catalysts to contain high additive contents (*e.g.*, up to 90%), offering significant room for modification of the formulation.^[174] Furthermore, the enhanced thermophysical properties, where quantified, have not been rationalized in relation to the structural organization. Since the increased thermal resistivity imposed by grain boundaries (due to phonon-interface scattering) and interstitial fluids can severely penalize the thermal conductivity of a composite body, the intrinsic properties of the additive cannot be directly extrapolated.^[226] Furthermore, strategies to directly incorporate conductive additives within shaped catalysts are virtually non-existent.

Zeolites are arguably the most successful heterogeneous catalysts, widely exploited in refinery and petrochemical applications.^[174] Building on continued efforts to improve fundamental understanding in the scale-up of zeolite catalysts,^[155,180,227] this chapter explores the impact of well-known conductive additives of distinct type and particle properties on the thermophysical properties of these insulating materials. A transient hot-plate method is selected to quantify the thermal conductivity since, unlike steady-state or membrane/thin film-specific measurements, it enables the convenient assessment over a wide range of length scales and shapes (Figure 5.1b). Binary and ternary systems, the latter additionally incorporating a binder, are shaped by different methods to decouple the contribution of catalyst geometry, while comparative measurements across a catalyst beds demonstrate that superior heat-transfer properties are retained even when the fluid phase becomes more influential. Visualization of the spatial integration of the additive, and in particular the three-dimensional insights gained by micro-computed X-ray tomography and focused ion beam-scanning electron microscopy, reveals the decisive role of phase connectivity in the up to one order of magnitude enhancements achieved. Thermographic profiling provides additional spatio-temporal resolution, confirming the enhanced heat-transfer properties of the catalyst ensembles. The findings are expected to

be of wide relevance for catalysis and other fields of application in which inefficient heat transfer hampers the performance such as sorbents, electrochemical, and energy storage.

5.2. Experimental

5.2.1. Materials

Catalyst pellets (20 mm diameter, 2 mm height) were prepared from the single-phase zeolite (ZSM-5) or additive powders (1 g) or from homogenized physical mixtures thereof (zeolite:additive dry mass ratio = 1:1) using a Specac press at 10 bar (unless otherwise specified) for 5 min. Catalyst extrudates (2 mm diameter, 5 mm length) were attained by extruding (Mini Screw Extruder, Caleva) the zeolite or zeolite-additive admixtures with an attapulgite clay binder (zeolite:binder:additive dry mass ratio = 1:1:2). The resulting bodies were dried (393 K, 12 h) and subsequently hardened (873 K, 3 h, 2 K min⁻¹) in flowing air (60 cm³ min⁻¹).

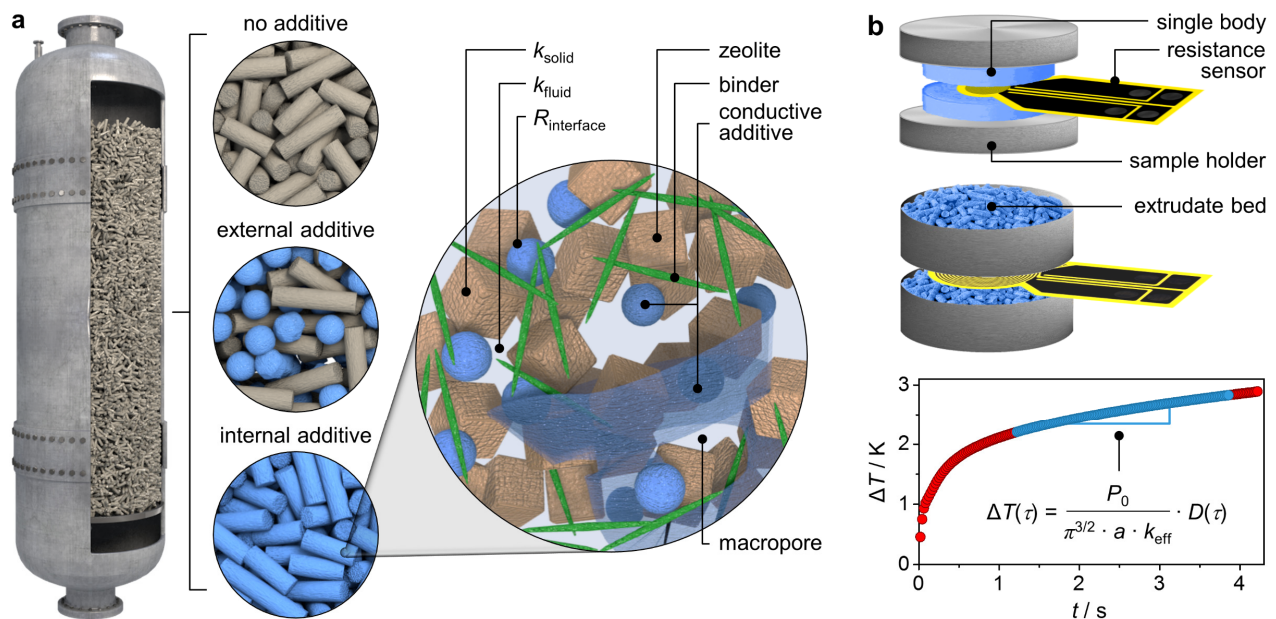


Figure 5.1. (a) Temperature regulation in industrial reactors is a multiscale task encompassing both radial and axial gradients across the packed bed and those localized within individual catalyst bodies. Heat transfer could be improved through the application of conductive additives, either external to, or within, the catalyst ensemble. The effective thermal conductivity of the latter, here illustrated for a zeolite catalyst, depends on the type and organization of the component phases and on the surrounding fluid medium. (b) A versatile transient hot-plate method is used to determine the impact of diverse additives on the thermal conductivity of catalyst bodies and beds, which is derived from the temperature change (ΔT) in relation to the total power output (P_0) and the radius of the resistance sensor (a) as a function of time $D(\tau)$.

5.2.2. Characterization Techniques

Mercury porosimetry was carried out in a Micromeritics Autopore IV 9510 instrument. Thermal gravimetric analysis in air was performed in a Mettler Toledo TGA/SDTA851e microbalance. Electrical conductivity across a sample pellet was measured with a Voltcraft VC130 multimeter. Micro-CT was undertaken by scanning extrudates stepwise (0.4°) through 360° , using a Skyscan 1172 system operated at 100 kV and 100 mA. FIB-SEM tomography was undertaken on non-embedded cross-sections using a Zeiss NVision 40 instrument (2 kV). 3D reconstructions of micro-CT and FIB-SEM 2D slices were generated using Amira and CTvox software, respectively. A FEI Tecnai F30 FEG microscope was used for TEM and SAED measurements. Thermography analysis was performed by using either a FLIR SC6000 MWIR (spectral range 3–5 μm , nominal resolution of 640×512 pixels) infrared camera equipped with a macroscopic objective ($f/2.3$) supporting a lateral geometrical resolution of up to 15 μm , or a FLIR E60 allowing imaging above 673 K. The accuracy of both cameras is ± 2 K. Videos in full frame mode were recorded to visualize thermal heat fluxes through the bodies (320×240 pixels). Infrared thermal imaging of the bodies was performed both during dynamic heating (296–873 K, 10 K min^{-1} , 2000 W) and in steady state (473, 573, 673, 773, and 873 K, 20 min equilibration time) phases using a precision titanic heating plate (PZ 28 3TD, Co. Gestigkeit GmbH, 23×16 cm, ± 2 K) covered with a closure head to ensure homogeneous heating.

5.2.3. Thermal Conductivity Measurement

The thermal conductivity of the shaped zeolites was determined by a transient method using a TPS 2500S Thermal Constants Analyzer according to ISO 22007–2. The full experimental protocol is detailed in Annex A (Figure A.17). In a typical measurement across a single body, the resistance sensor (Ni metal double spiral, mica insulated, 6.4 mm diameter) was fixed between two pellets of the desired composition in a thermally-insulated oven and heated to the desired temperature (573–723 K). Analogously, the thermal conductivity of a catalyst bed was determined by fixing a larger sensor (29.2 mm diameter) between two cylindrical containers (60 mm diameter, 25 mm height) filled with catalyst extrudates. Prior to measurement, the apparatus was thermally-equilibrated for 90 min. The sensor operates as both the heat source

Table 5.1. Structural and thermophysical characteristics of the additives studied.

Additive	d_{additive}^a [μm]	k_{eff}^b [$\text{W m}^{-2} \text{K}^{-1}$]	k_{in}^c [$\text{W m}^{-2} \text{K}^{-1}$]
Silicon carbide, SiC_n	<0.1	0.37	270 ^[228]
Silicon carbide, SiC_p	~ 50	0.65	-
Silicon carbide, SiC_m	~ 400	- ^d	-
Aluminum nitride, AlN	~ 10	1.2	320 ^[228]
Copper spherical, Cu_s	<75	5.5	400 ^[228]
Copper fiber, Cu_f	50×1000	5.5	-
Carbon nanotubes, CNT	0.1×10	-	<10000 ^[220]
Boron nitride sheets, BN_n	<1	1.7	~ 2000 ^[216]
Boron nitride sheets, BN_m	~ 44	10	-
Graphite sheets, gr	<20	10	~ 2000 ^[218]

^a Average particle diameter according to manufacturer's specifications; ^b Effective thermal conductivity of the single-phase body; ^c Literature values of the intrinsic thermal conductivity; ^d Shaped body not attained.

and a resistance thermometer, recording the temperature change over time. The electrical power supplied (P_0) was adjusted to achieve a temperature increase (ΔT) of approximately 0.5–2 K during the measurement time (t), which in turn was set to ensure that heat propagation did not exceed the sample boundaries. Subsequently, the thermal conductivity is calculated within a region of validity, omitting the initial and final data points relating to the sensor pellet heat transition and thermal spill over, respectively. Each measurement was conducted at least 5 times, with a 15 min interval to allow for thermal relaxation of the material.

5.3. Results and Discussion

5.3.1. Impact of Additives on the Thermal Conductivity of Zeolite Bodies

To rationalize the effect of additive integration in zeolite bodies, it was first necessary to develop a robust approach to evaluate the thermal conductivity of a catalyst in technical form. Upon powder agglomeration, the porosity of a shaped body, and hence its effective

thermal conductivity, depends on the degree of compaction. For single-phase zeolite pellets, conductivity values were found to vary within a narrow range ($0.17\text{--}0.41\text{ W m}^2\text{ K}^{-1}$) depending on the pelletization pressure, exhibiting an inverse relation with the pore volume determined by Hg porosimetry (Figure A.12a). As the latter technique only probes pores $>3\text{ nm}$, the amount of mercury intruded closely relates to the interparticle porosity and not that of the microporous zeolite. Another parameter that can impact the effective thermal conductivity is the degree of hydration. Comparatively, the effect of pre-treatment of zeolite pellets under vacuum or at 75% relative humidity for 2 weeks emerged to be negligible (Figure A.12b).

Table 5.1 overviews the nomenclature, and the particle and thermophysical characteristics of the highly-conductive additives explored in this work. As expected, higher effective thermal conductivities ($0.37\text{--}10\text{ W m}^2\text{ K}^{-1}$) were evidenced over the single-phase additive bodies than that of the pure zeolite ($0.28\text{ W m}^2\text{ K}^{-1}$) when shaped under equivalent conditions (10 bar, 5 min). The significant reduction with respect to their intrinsic values (typically well above $100\text{ W m}^2\text{ K}^{-1}$) reflects the fact that the calculations or experiments, from which they are derived, do not account for additional resistances, arising from the increased density of grain boundaries and void volume within the shaped materials. When integrated into zeolite bodies (1:1 dry mass ratio, coded cz40-x where x is the additive applied), effective thermal conductivity enhancements were achieved with respect to the single-phase zeolite in all cases (Figure 5.2a), reaching over an order of magnitude ($3.6\text{ W m}^2\text{ K}^{-1}$) on introduction of graphite (cz40-gr). This range of improvement in the thermal conductivity is comparable with those previously evidenced over graphite-containing pellets of zeolite 4A (from $0.15\text{--}0.43\text{ W m}^2\text{ K}^{-1}$)^[208] or MOF-5 ($0.1\text{--}0.9\text{ W m}^2\text{ K}^{-1}$)^[209], the absolute values depending on the compaction density, amount of additive, and differences in the shaping protocol. Interestingly, the enhancements appeared to correlate with the additive morphology, with sheet-like $>$ rod-like $>$ pseudo-spherical particles. Complementary analysis of the electrical conductivity of the graphite- and copper-containing (cz40-Cu_s) catalysts revealed similar trends with respect to particle morphology, indicating a possibly influential role. In contrast to the significant ohmic resistance ($R < 6\ \Omega$) observed in the case of cz40-gr, much higher values ($R > 20\text{ M}\Omega$) were evidenced for cz40-Cu_s, despite the fact that bulk copper is an excellent electrical conductor.

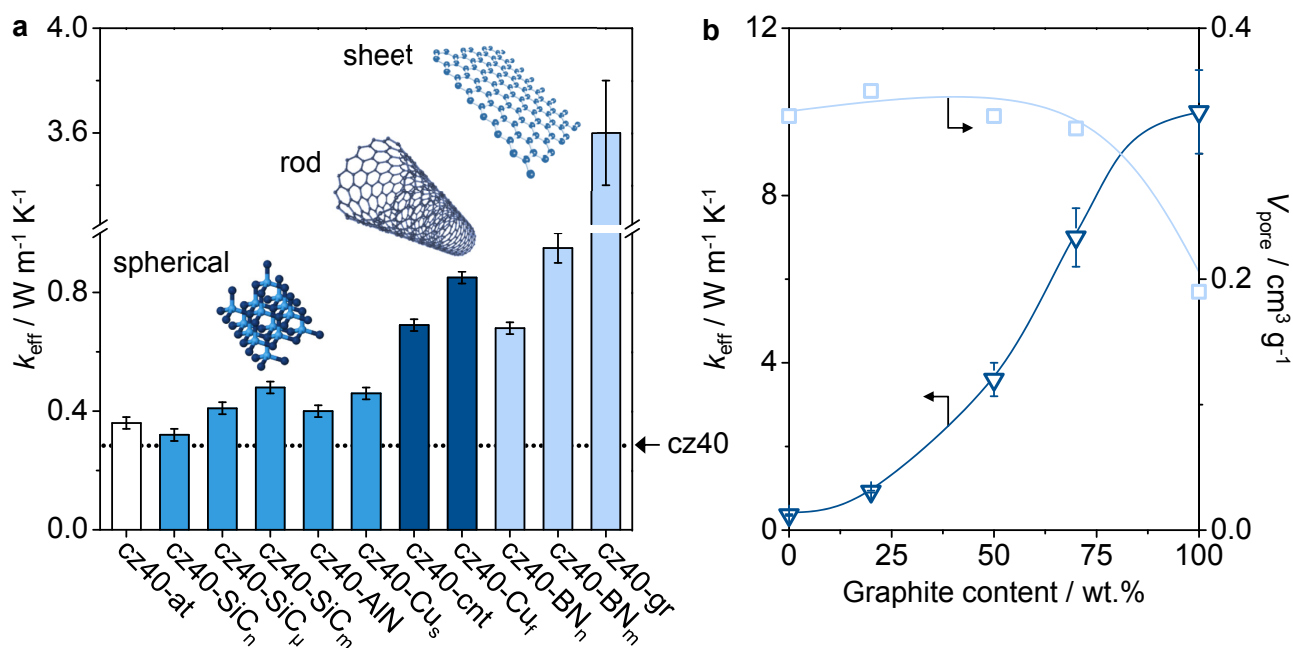


Figure 5.2. (a) Effective thermal conductivity of individual zeolite bodies integrating additives of different type, particle size, and morphology, compared to the single-phase zeolite (dotted line). (b) Relative trend in the effective thermal conductivity and the interparticle pore volume of graphite-containing composites as a function of the additive content.

For a given morphology, a clear impact of particle size was also evident. In particular, nano-sized SiC_n and BN_n , which offer high specific surface areas, performed less effectively than their macro-sized SiC_m and BN_m analogues. Aside from increasing the interfacial thermal resistances due to a higher density of grain boundaries, decreasing the particle size can also change the surface chemistry of the additives. In both cases, the nano-sized additives were found to be more susceptible to surface oxidation, as evidenced by thermogravimetry (Figure A.13), which could lower their intrinsic thermal conductivity. One of the most revealing insights came upon comparison of the thermal conductivity of the zeolite additive composites as a function of the interparticle pore volume (Figure 5.3). An almost linear dependence was observed for additives of pseudo-spherical character, which also described the effective thermal conductivity of the pure zeolite reference and zeolite-binder samples, indicating that the improvements attained on application of these additives purely originates from the reduced interparticle pore volume of the catalyst ensemble. On the other hand, rod- and sheet-like additives displayed distinct correlations, further supporting the strong dependence of the thermal conductivity enhancement on the particle morphology, which dominated over the impact of their intrinsic thermal conductivity. Finally, as exemplified for the graphite-containing body, the additive content

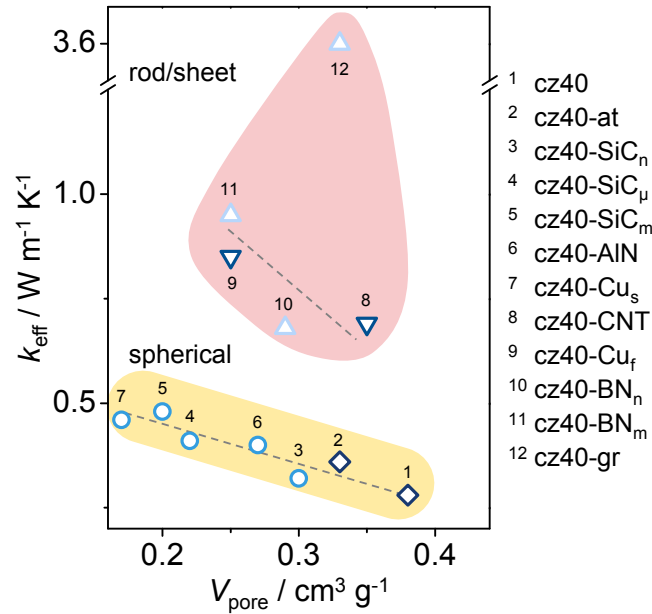


Figure 5.3. The effective thermal conductivity of zeolite bodies integrating conductive additives of different morphology as a function of the interparticle pore volume. The greyish shaded areas group additives of pseudo-spherical and rod-/sheet-like morphologies, respectively.

played a significant role (Figure 5.2b). The sigmoidal dependence in the effective thermal conductivity implies that the observed enhancement did not simply reflect the proportional contribution of the zeolite and additive phases, and was also not directly correlated with the total pore volume of the pellet ($0.3 \text{ cm}^3 \text{ g}^{-1}$), being one of the highest of any of the additive-containing bodies.

5.3.2. Temperature- and Length-Scale Dependence of Additive Effects

To evaluate the scope of the superior thermal conductivity, the effectiveness of graphite and silicon carbide, representative of additives of sheet-like and pseudo-spherical morphology, was evaluated as a function of temperature with respect to the additive-free reference. In agreement with the suspected dominance of the interparticle porosity, the thermal conductivity of the cz40-SiC _{μ} follows a very similar trend to the reference sample; almost doubling as the temperature approached 723 K (Figure 5.4a). This behavior is typical of insulating solids and stems from the increased contribution of radiative heat transfer and conduction via the fluid phase. In contrast, the exceptional thermal conductivity of the cz40-gr body remained almost unchanged upon heating to 723 K. The slightly decreased values observed at elevated temperatures stem from the high Debye³ temperature ($>1000 \text{ K}$) of graphite, which causes the

thermal diffusivity to govern.^[218]

To verify the impact of the superior thermophysical properties of the catalyst bodies over different length scales, we also evaluated the effective thermal conductivity of packed beds of graphite-containing or additive-free extrudates or granules. Herein, it was necessary to investigate ternary-component systems integrating a clay binder (attapulgite) to ensure the mechanical integrity of the bodies (coded cz40-at or cz40-at-gr). Compared with the individual bodies, the heat conduction was noticeably reduced in air at 723 K, to less than 20 or 50% over the graphite-containing and additive-free extrudates, respectively (Figure 5.4b). Under these circumstances, the temperature dependency of the graphite-containing ensembles also changed. These observations emphasized the severe limitations posed by the interfacial contact between shaped bodies, which limit the scope of enhancement of heat transfer via better conduction at the reactor scale. Nonetheless, the improved thermal properties evidenced over the single bodies were retained across the packed bed, implying that local heat transfer management of shaped bodies is still very relevant. The geometry and size distribution of the individual bodies determine the packing density and consequently the porosity of the catalyst bed. Comparatively, a linear correlation between the effective thermal conductivity and the packing density was evidenced upon measurement of extrudates or of granules of decreasing average diameter (Figure A.14).

In research, the bed porosity is often reduced by the addition of inert diluents as SiC,^[206] which fill the voids between the catalyst bodies. While this is partly to suppress the axial dispersion and bypassing effects, their presence also promotes isothermality within the bed, which is widely exploited in kinetic studies.^[229] In fact, the thermal conductivity of the packed beds was clearly increased upon introduction of SiC_m particles as an external diluent (Figure 5.4c). Importantly, the graphite-containing composites remained 50% higher than that of the additive-free bed, coinciding with that of a bed of pure SiC_m particles ($0.29 \text{ W m}^{-2} \text{ K}^{-1}$), representing the upper limit for potential heat transfer enhancements achievable by the external addition of silicon carbide.

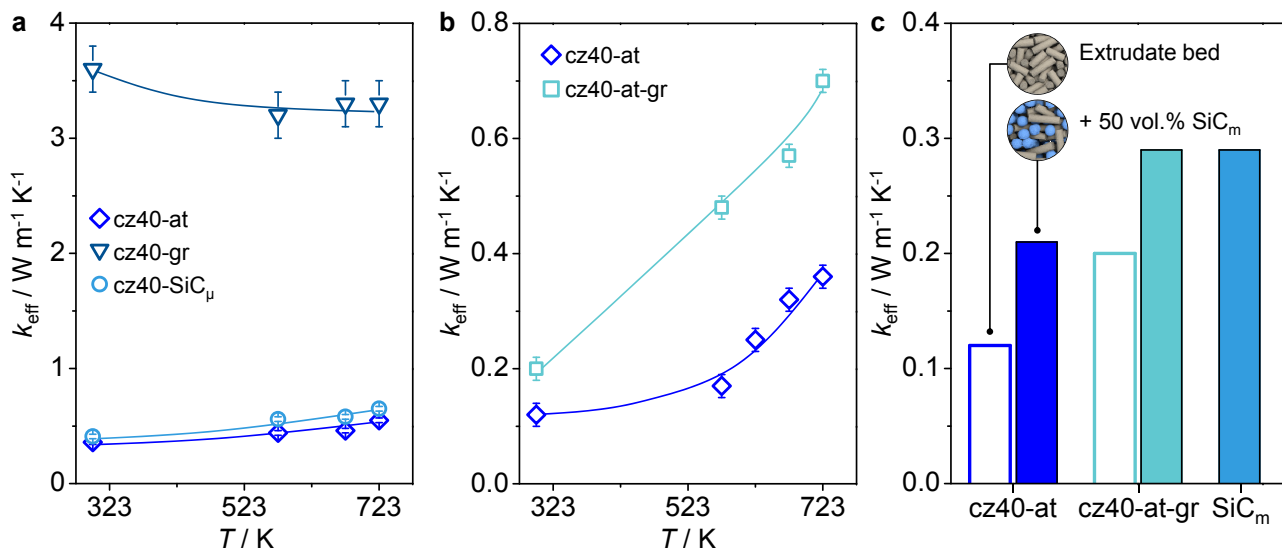


Figure 5.4. Impact of temperature on the effective thermal conductivity of SiC- and graphite-containing zeolite catalyst (a) bodies and (b) packed beds with respect to the analogous additive-free case. (c) Effective thermal conductivity of additive-free and graphite-containing catalyst beds at room temperature in the presence or absence of SiC_m introduced as an external diluent. The conductivity of a single-phase additive bed is shown for reference.

5.3.3. Rationalization of Additive Effects

To further understand the influence of the particle properties, differences in the phase distribution and local particle arrangement within the composite bodies were explored by state-of-the-art microscopic and tomographic techniques (Figures 5.5 and A.15). We have previously demonstrated the wide applicability of focused ion beam-scanning electron microscopy (FIB-SEM) to resolve these properties, particularly when coupled with X-ray microtomography (micro-CT) for the non-destructive analysis of macroscopic features and equivalently transmission electron microscopy (TEM) to access finer details of the nanostructure.^[180,227] FIB-SEM examination of extrudate cross-sections highlighted the widely varying interaction of the additives with the zeolite and binder in relation to their distinct morphology and size (Figure 5.5a-c). In the copper-containing samples, evidence of melt was observed for both the pseudo-spherical and rod-like forms, which engulfed the zeolite and binder particles in close proximity, and was most evident around the copper fiber due to the larger diameter. This observation explains the reduced interparticle pore volume evidenced in these samples, which could not have been predicted from the particle properties of the as-received additive. Nonetheless, the additives remained discretely located in the 2D section. On the other hand,

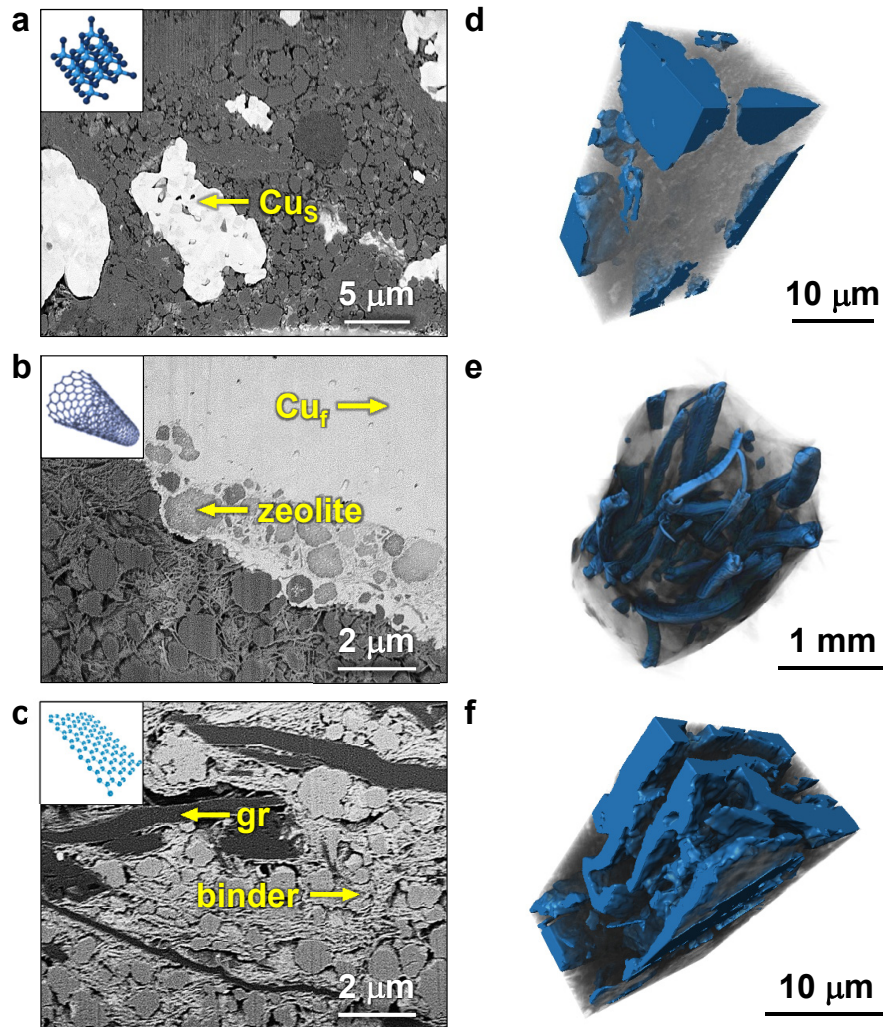


Figure 5.5. Backscattered FIB-SEM micrographs of the phase distribution within internal cross-sections of extruded zeolite catalysts containing (a) pseudo-spherical copper, (b) rod-like copper, or (c) sheet-like graphite additives. Computed reconstructions of the corresponding three-dimensional organization of the additive phase (blue) with respect to the zeolite-binder matrix (grey) as imaged by (d,f) FIB-SEM or (e) micro-CT.

the sub-micrometer sheet-like structure of graphite was seen to wind between the zeolite-binder matrix, which in 2D micrographs appeared like veins extending across the entire image (Figure 5.5c).

The origin of the superior connectivity of large elongated additives became clearly apparent from three-dimensional reconstructions computed from FIB-SEM and micro-CT datasets. The isolated distribution of large heterogeneously-sized copper particles within the matrix lacked a clear path of low thermal resistivity, while the 1D shortcuts created by the copper fibers extended over much larger distances with respect to the zeolite particle length scale (Figure 5.5d,e). In the latter case, the preferred orientation of the copper rods, which increased

the thermal percolation in the axial direction of the extrudate due to a reduced number of grain boundaries, stems from the extrusion process. However, the fibers were widely spaced and therefore comparatively large volumes of the catalyst ensemble may not benefit from the enhanced thermal conductivity. The three-dimensional interconnectivity of the graphite sheets, providing facile closely-spaced paths of heat conduction throughout the whole body, were pivotal to the substantial benefits observed for this additive (Figure 5.5f).

Further insight into the lower relative effectivity of the boron nitride sheets, which have an isoelectronic hexagonal structure and large theoretical in-plane thermal conductivity similar to graphite, was attained by transmission electron microscopy (Figure A.15). In this case, although the additive nicely surrounds the zeolite, a high density of grain boundaries was inevitable due to the smaller particle size of the additive. A similar argument could be extended for the relative impact of the carbon nanotubes and nano-sized SiC, both of which also retain their crystal and particle integrity after the shaping process. TEM images further confirm the preserved crystallinity and highlight the large in-plane dimensions of graphite, which could easily provide efficient conduction paths.

5.3.4. Profiling Thermal Gradients in Composite Bodies

To fully contextualize heat transfer within composite bodies, it is necessary to study the response to temperature changes in a spatially-resolved manner. Infrared thermography is a powerful tool to detect thermal gradients during static or dynamic heating under a wide range of conditions, and has been previously applied to screen for potential leads in combinatorial library of heterogeneous catalyst powders,^[230] or for changes in catalytic activity as a result of external stimulus.^[231]

Here, thermographic analysis of individual cz40-at, cz40-SiC_n, and cz40-gr pellets during dynamic heating revealed significant variations in the heat-transfer properties (Figure A.18), which directly correlated with the increasing effective thermal conductivity of these samples. In particular, the temperature of the graphite-containing body clearly increased at a much faster rate than the additive-free or the SiC-containing bodies. Furthermore, inhomogeneous local (and temporal) heat fluctuations were evidenced on the surfaces of the latter, forming cold and hot spots, which became more pronounced at elevated temperatures. Following isothermal

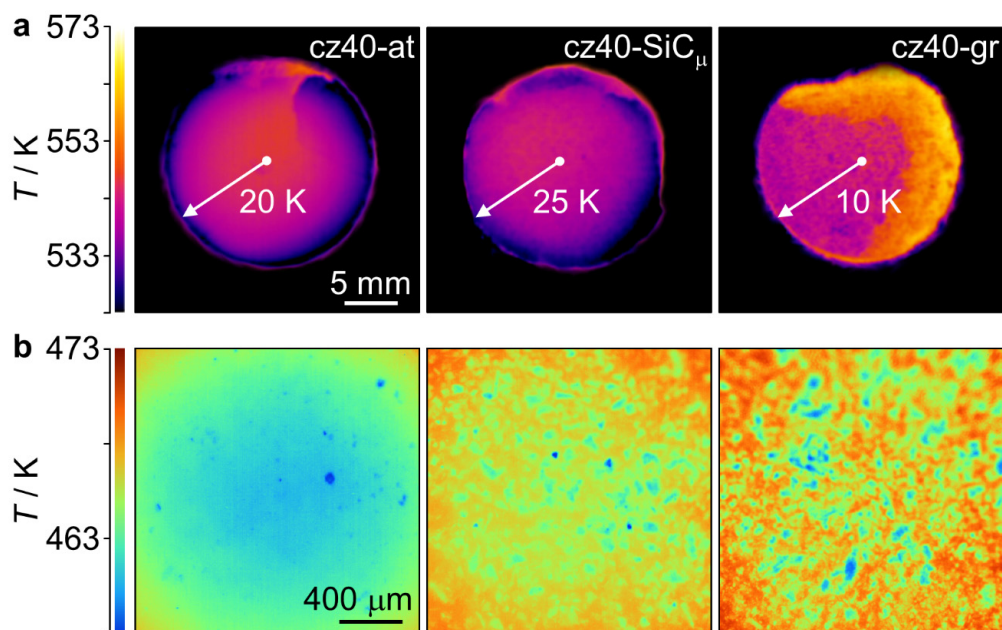


Figure 5.6. (a) Low- and (b) high-magnification infrared thermographs of the additive-free and of the SiC-, and graphite-containing zeolite catalysts acquired after isothermal heating for 20 min at 573 K. The average radial temperature gradients are indicated. The scale bars apply to all images in the same row.

heating, low magnification IR thermographs of cz40-at and cz40-SiC_μ displayed a core shell-like heat distribution with a hot center and cool edge, while cz40-gr exhibited a more uniform heat profile (Figure 5.6a). Emissivity-corrected quantification of the surface temperature along the radial direction (Figure A.16) revealed comparative temperature gradients of approximately 10, 25, and 20 K over cz40-gr, cz40-at, and cz40-SiC_μ after static heating at 573 K, respectively.

Using a macro lens to obtain a higher spatial resolution, the acquirement of high-magnification maps of the temperature distribution over the center of the pellets (*ca.* 2×2 mm) enabled further correlation of the improved heat transfer with the additive morphology (Figure 5.6b). While the additive-free body exhibited the coolest and most homogenous heat profile, local heterogeneities were observed in the presence of SiC_μ or graphite which resembled the morphological appearance of the additives identified by the prior microscopy analysis. Infrared profiling of thermal distributions and variations at high spatial resolution permits to identify, characterize, and quantify heat transfer patterns in complex composite bodies.

5.4. Conclusions

Applying a robust transient hot-plate technique coupled with appropriate visualization tools to quantify and understand the benefits of introducing conductive additives, this chapter has demonstrated a rational approach through which to enhance the heat-transfer properties of zeolites in common technical forms. Computed reconstruction of the internal particle arrangement in three dimensions as well as infrared thermography proved crucial to corroborate the tremendous importance of additive interconnectivity. In particular, the exceptional order-of-magnitude improvement in the effective thermal conductivity evidence on application of graphite could be rationalized on the basis of its elongated sheet like particles, which created an interwoven network of paths of decreased thermal resistivity between the other constituents. On the other hand, independent of their bulk characteristics, additives of pseudo-spherical morphology did not benefit the thermal conductivity of zeolite ensembles, which emphasized the importance of macro-sizing in one or more dimensions. The effects of optimal additive integration were shown to significantly outweigh those of decreasing the interparticle pore volume or increasing the degree of hydration of the shaped body, and noticeably improved the thermal conductivity of the packed bed, where the contributions of fluid-phase conduction and radiative heat transfer are more dominant. Considering their general nature, the findings are expected to provide key insights to enable the improved exploitation of additives to improve heat transfer within insulating materials in diverse applications like catalysis, sorbents, electrochemical, and energy storage.

Chapter 6

Conclusions and Outlook

Scientific developments in catalysis over the last two decades justified a change in mind-set to face the challenge of going beyond the atomic level understanding of model systems and to apply the theory, knowledge, and insights gained to technical catalysts. As evidenced in this thesis, the latter exhibit widely divergent performance from research analogues, and hence this step is crucial to comprehend the opportunities, which formulation and structuring can bring to their function, or, in contrast, the havoc, which poor choices can wreak. With this in mind, a new stream of academic research looking into basic aspects of industrial catalyst preparation, characterization, and application is envisaged.

Prior to the commencement of this thesis, the understanding of (hierarchical) zeolites and the interpretation of their catalytic enhancement was limited to the powder form. To fully utilize the potential of these advanced materials, the critical steps, which needed to be succeeded, included (i) the transition from gram-to-ton-scale manufacture, and the structuring of powders with additives into optimal macroscopic shapes, (ii) the identification of suitable characterization approaches to unlock the structural complexity of catalysts in technical form, and (iii) the understanding of the cause and nature of zeolite-additive interactions, which can occur during structuring.

6.1. Industrial Manufacture

Although being realized daily by industry, the academic study of technical catalyst preparation has remained in its infancy far too long. The need to rationalize the latter directly relates to the proficiency in translating scientific advancements from the lab to the industrial scale. Exemplary progress has been achieved in the scale-up, that is the industrial-scale manufacture and subsequent structuring, of hierarchical ZSM-5 prepared by treatment in alkaline media.

Scale-up. Among the wide variety of synthetic approaches available to amend conventional zeolites to their hierarchical analogues, so far only the desilication of commercial zeolites was demonstrated as a cost-effective route, that fulfills the primary attributes (effective, versatile, and scalable) to reach the market in a relatively short timeframe. The hierarchical ZSM-5 powders prepared at bench and industrial scale evidenced identical properties, despite the necessary adjustment of individual unit operations to scale-up. Similar key steps could be extrapolated to prepare hierarchical zeolites of other frameworks, like USY, retrofitting existing laboratory protocols to industrial standards. However, if additional compounds (*e.g.*, pore-directing agents) or additional treatment steps (*e.g.* acid washing) are required, supplementary unit operations may be necessary.

Structuring. Without clear fundamental guidelines on how to shape the powders obtained, a convenient starting point was to follow protocols established for conventional zeolites. In this way, mechanically-stable mm-sized hierarchical ZSM-5 granules and extrudates were attained that preserved their outstanding properties and functionality. Herein, the industrial collaboration with Zeochem through the sharing of expertise and equipment provided the platform from which to advance with the scale-up from a practical standpoint, being exemplary for promoting a more fluid dialog between academia and industry. Having fitted our laboratory with bench-scale shaping tools, it was then possible to study in more depth the impact of binders and the shaping step.

6.2. Characterization Toolbox

While the use of characterization techniques and the information derived to assess the quality of catalysts at the laboratory-scale is second nature, most of these methods have been designed for the analysis of powders, and thus the direct extrapolation to precisely represent the properties and function of technical bodies could not be taken for granted. In this context, visualization approaches, capable of connecting atomic-scale features of the active surface with the macroscopic properties of shaped catalysts, helped to improve some of the more empirical aspects of scale-up (Figure 6.1). Advances in visualization methodologies, in terms of sample preparation, achievable resolution, practical availability, and data analysis, have



Figure 6.1. Learning to characterize technical materials to optimize their assembly and function.

greatly widened their scope, enabling unprecedented insight into the properties of catalysts. A graphical overview of relevant techniques and the types of information currently accessible is presented in Figure 6.2.

Bulk vs. Spatially-Resolved Techniques. Standard techniques of bulk characterization quantify solid material characteristics (structure, porosity, particle size, and chemical composition), but provide no information on their spatial (and time) resolution, like the distribution of phases and related connectivity of the pore networks within the technical bodies. The application of a battery of imaging techniques granted complementary and corroborative insight into the complex organization of the zeolite and binder particles and the corresponding distribution of the different levels of porosity within the technical bodies. Moreover, in contrast to the well-established methods of bulk acidity assessment (*e.g.*, infrared spectroscopy of adsorbed probe molecules), which are limited to probing powder samples, that is in form of crushed bodies, confocal laser scanning microscopy of appropriately stained technical catalyst was recognized to qualitatively distinguish acidity variations over whole bodies in a non-invasive manner.

Single vs. Combinative Visualization Techniques. Typically, method development has largely focused on extracting characteristic information from data collected through single techniques. Because any technique only provides partial knowledge, consolidating the overlapping scope gained through multiple techniques is particularly useful, as it provided both complementary information and a means of confirming the representativeness of the observations made. Since the detail discernible by any given imaging technique is limited by its intrinsic resolving power, the desired field of view, and the specific sample, here the technical body, integrative approaches were essential to trace property relationships over the complete range of scales. A major challenge was to ensure that the observations made remain representative, as the field of view was diminished, which became even more demanding when tackling bodies of increasing dimensions.

At the nanoscale, while TEM tomography provides beneficial high-resolution insight, for example, to confirm the pore connectivity of hierarchical zeolites, this technique is limited by the requirement for beam transparency, necessitating extensive sample preparation to image the internal structure of mm-sized specimens. Micro-computed X-ray tomography and focused ion beam-scanning electron microscopy emerged as a robust combination to supplement the nanoscale information, gained by TEM, and bridge with the macroscopic structure, allowing corroborative insight. The acquired FIB-SEM data highlighted differences in the dispersion of the binding phase and in the tortuosity of the interparticle pore network, depending on the shaping method. Simultaneous EDX analysis over the same sample area could also identify compositional variations. As the non-invasive technique, the whole specimen could be visualized by micro-CT with minimal risk of altering the sampled volume. Although this technique cannot yet match the spatial resolution of its electron microscopy counterparts, it revealed large differences between the granulated and the extruded catalysts with respect to both the homogeneity of the phase distribution and the presence of structural defects such as cracks and voids.

Furthermore, the scope of the complementary visualization approach could be extended to other solid catalysts in technical form, *e.g.*, pelletized $\text{RuO}_2/\text{SnO}_2\text{-Al}_2\text{O}_3$ catalyst used industrially for the HCl oxidation to Cl_2 and an extruded metal-organic framework (Cu-BTC).

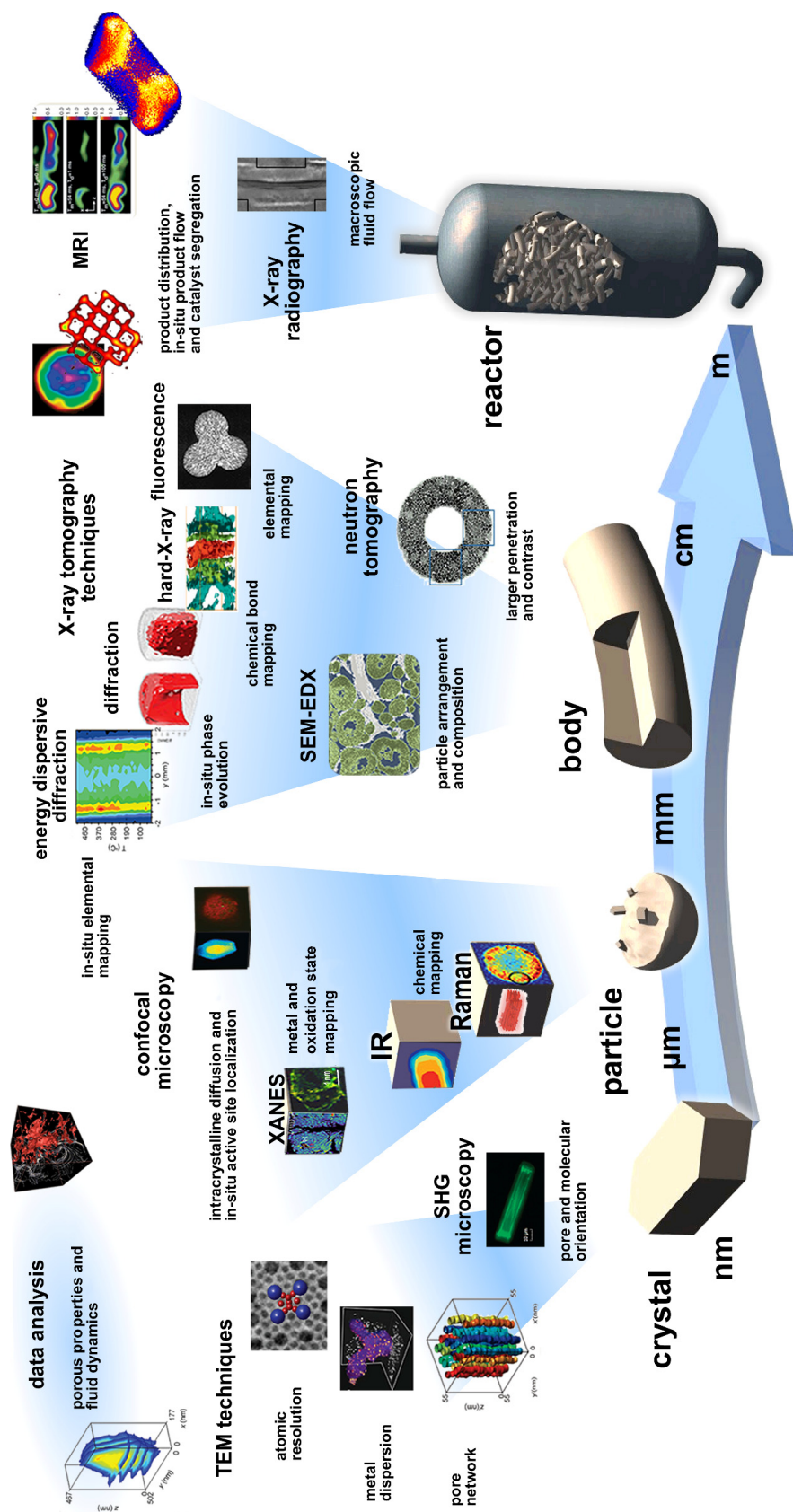


Figure 6.2. State-of-the-art visualization tools can be applied to gain a deeper understanding of catalysts from the properties of single particles and their interface, to the bodies in which they are applied and upwards to the reactor scale. Sample imaging becomes more challenging with increasing size, and the characterization of technical forms has only been tackled by a limited number of studies. In this respect, non-invasive techniques with larger penetration offer distinct advantages, in particular for in situ studies. Complementing all the summarized techniques, advanced methods to analyze the data acquired help to derive and quantify different properties throughout the whole range of scales.

FIB-SEM and micro-CT observations furthered the understanding with respect to prior microscopic techniques, and allowed to reveal to-date unknown information on the internal arrangement of component species within the technical forms.

Reference Materials. Unlike research catalysts, the screening of technical catalysts is impractical due to the larger sample requirements. A solution was found in the systematic characterization of zeolite-binder admixtures prepared by physical mixing or ball milling. The as-received individual component powders could be pre-treated under equivalent conditions to simulate those, which would be experienced during shaping, serving as reference materials.

The techniques, presented in this thesis, comprise a rich toolbox for unraveling the inner processes of catalyst bodies, especially FIB-SEM complemented by EDX proved a most informative method, providing a broad field of view with sufficient resolution to assess the distribution and composition of the binder and zeolite phases, irrespective of the specimen size and thickness. Nonetheless, improvements in the resolution achievable within technical bodies will be important to understand their evolution during assembly and application, in particular when striving to understand functional details under realistic conditions (*i.e.*, temperature, pressure, atmosphere). These difficulties will hopefully be overcome with the extended application of in situ techniques and recent technological advances, such as aberration correction for electron microscopes, far-field optical nanoscopy, nano X-ray focusing, laboratory-scale bright light sources, and high-definition NMR spectroscopy, which permit increased penetration depth and resolution in complex samples. However, for these techniques to become partners in the rationalization of catalyst scale-up, substantial efforts are also required to correlate the visualization data with the observed reaction kinetics and transport phenomena. As a final point, it is noteworthy that most catalytic processes occur within much faster timeframes than that, which can possibly be measured using existing visualization techniques, leaving the time resolution as the main limitation.

6.3. Zeolite-Additive Interactions

The use of additives, in particular binders, to structure the active phase into technical bodies is common practice at industrial scale. Yet, understanding the wide range of opportunities, which

formulation and structuring can contribute to the catalytic function, is largely overlooked. Additives can exhibit, besides their evident primary function, a number of secondary functions. In **Chapter 4** it was demonstrated that the combined chemical and physical effects of inexpensive binders brought about significant performance benefits, exceeding those established by the introduction of mesopores in the zeolite crystals. Consequently, the multifunctional nature of technical zeolite catalysts should be properly exploited to rationally design catalysts already at laboratory scale for targeted applications. This requires the identification of compositional and structural performance descriptors over technical catalysts. to first catalogue and then selectively tune complex zeolite-additive interactions.

Binders. Indispensable to attain durable bodies, in particular if the active phase exhibits poor self-binding properties (*e.g.*, zeolites), binders typically constitute a large portion of the technical catalyst. Aluminas, silicas, and natural clays are commonly applied due to their refractory properties, high earth abundance, non-toxicity, and relative low cost. Ideally, they can also enhance the catalytic performance, like shown for clay binders, which due to their large particles contribute to a well-defined internal macropore network, enhancing mass transfer properties. In contrast, a more densely packed internal structure proved less beneficial. Moreover, while a partial dealumination or exchange of acid sites with mobile ion species can reduce the acidic properties of technical catalysts, no direct correlation could be derived from catalytic data, emphasizing the complexity of zeolite-binder interactions.

Thermally-Conductive Agents. Fundamental strategies of heat transfer enhancements in technical bodies have so far been reduced to the use of catalyst carriers made from SiC, being less appropriate for zeolite-based applications. While the addition of thermally-conductive agents was shown to considerably increase the thermophysical properties of the shaped zeolite bodies, the degree of improvement could be rationalized, in terms of additive morphology and interconnectivity required, to provide facile closely-spaced paths of heat conduction throughout the whole body. To reduce the density of grain boundaries, macro-sizing in one or more dimension was essential, maintaining an elongated continuous phase network.

Cause and Nature. In the most general sense, zeolite-additive interactions can be defined as an alteration of a property of the active phase, which occurs upon contact with additives

during processing of a body. They can be distinguished according to their nature into physical (*i.e.*, changes in morphology/porosity resulting from particle arrangement in the shaped body) or chemical (*i.e.*, changes in acid site distribution/quality/accessibility through creation of new or modification of existing sites) interactions. While intimate contact between the component species is irrevocably required, a zeolite-additive interaction could be induced by assistance of a solvent, or thermal or mechanical activation, individually or simultaneously during the process of scale-up. For example, whereas thermal activation may suffice to cause the sintering of the binder (*e.g.*, aluminum phosphate), others require the presence of water to allow mobile ions to migrate from the binder to the zeolite (*e.g.*, attapulgite).

Despite the ubiquitous relevance, methods to assess the interactions between component species, such as between zeolite and binder, were not yet devised. Ball milling was shown as an effective lab-scale tool to screen for chemical interactions in zeolite-additive admixtures, but more sophisticated sample preparation and selection is crucial to gain better insight. Building on the toolbox of complementary imaging techniques, a combination of confocal laser scanning microscopy and elemental mapping by X-ray fluorescence spectrometry allows the detection and localization of zeolite-binder interactions.

Moreover, it can be expected that the knowledge of the presence of certain zeolite-additive interactions could be extrapolated to other shaping techniques or structuring protocols. For example, spray drying a suspension of zeolites in the presence of a binder, containing alkaline species, could cause the solvent-assisted partial migration of mobile ions, altering the acidic properties in the resulting spray-dried microsphere.

6.4. Outlook

The work, described in this thesis, has led to major achievements in the understanding of scale-up of zeolite catalysts with enhanced functionality, and the identification of suitable advanced characterization techniques to unravel the complexity of the resulting technical bodies. Headway has been achieved in the elucidation of the cause and nature of zeolite-additive interactions. Nonetheless, some aspects need further dedication.

For example, the synthesis of the catalyst particles, including their size and shape as well

as their porous structure and distribution of active sites, is always done within the context of the overall process requirements, giving consideration to kinetic and mass transport as well as hydrodynamic parameters of the selected reactor configurations.^[26–31] While reactor engineering was beyond the scope of this thesis, it yet remains to be addressed how the geometry of the technical body (*e.g.*, extrudates, trilobes, miniliths, *etc.*) would impact on the catalytic performance.

Moreover, in terms of understanding zeolite-additive interactions, this thesis has only been exploring the implication of the latter in the conversion of methanol to hydrocarbons. It is of general interest to expand the scope to other processes in the field of catalysis and adsorption. This entails a reassessment of the impact of zeolite-additive interactions on the function, but ultimately aids in the establishment of a catalog of potential component interactions for any targeted application.

Also the development of novel descriptors remains of interest. For example, while the importance of the mesopore size, distribution and connectivity on the catalytic activity was recently demonstrated over hierarchical zeolite powders prepared by varying synthetic routes, a similar design criteria could be established in technical form. Structuring of zeolites with various binders gave rise to technical bodies with different macroporosity, which was related to differences in the diffusivity of 2,2-dimethylbutane. Thus, it could be envisaged to identify a mass transfer descriptor for technical catalysts. Herein, the use of porogen could facilitate the tuning of the macroporosity.

Numerous advances have been and continue to be made in methods to characterize the structure of complex porous materials. As these techniques become more accessible, the magnitude and the value of the data, which can be attained and how it can be exploited in catalyst design, will undoubtedly grow. With the continued demand to improve process efficiency, attaining a more detailed understanding of the inner complexity of technical catalysts is vital. Correlation of the in-depth knowledge gained by visualization with the formulation and structuring protocol, the physico-chemical properties, and the performance will clearly facilitate the understanding and optimization of their scale-up.

In conclusion, knowing that zeolite-additive interactions can have major implications,

it would be necessary to rethink traditional strategies of catalyst development without compromising the scientific quality. Understanding the relative implications of composition and porosity in technical forms will enable the earlier consideration of appropriate shape and additives in catalyst development programs, depending on the process requirements of the targeted application.

Bibliography

- [1] Anastas, P. T., Kirchhoff, M. M., and Williamson, T. C. *Appl. Catal., A* **221**, 3–13 (2001).
- [2] Hölderich, W., Röseler, J., Heitmann, G., and Liebens, A. T. *Catal. Today* **37**, 353–366 (1997).
- [3] *Acmite Market Intelligence, Market Report: Global Catalyst Market, 2nd Edition*, (2010).
- [4] *BCC Research, Catalysts for Environmental and Energy Applications, Wellesley, USA*, (2010).
- [5] Anastas, P. T. and Eghbali, N. *Chem. Soc. Rev.* **39**, 301–312 (2010).
- [6] Wan, K. T. and Davis, M. E. *Nature* **370**, 449–450 (1994).
- [7] Besenbacher, F., Chorkendorff, I., Clausen, B. S., Hammer, B., Molenbroek, A. M., Nørskov, J. K., and Stensgaard, I. *Science* **279**, 1913–1915 (1998).
- [8] Thomas, J. M. *Angew. Chem., Int. Ed.* **38**, 3588–3628 (1999).
- [9] Wight, A. P. and Davis, M. E. *Chem. Rev.* **102**, 3589–3614 (2002).
- [10] Topsøe, H. *J. Catal.* **216**, 155–164 (2003).
- [11] McMorn, P. and Hutchings, G. J. *Chem. Soc. Rev.* **33**, 108–122 (2004).
- [12] Astruc, D., Lu, F., and Aranzaes, J. R. *Angew. Chem., Int. Ed.* **44**, 7852–7872 (2005).
- [13] Thomas, J. M., Raja, R., and Lewis, D. W. *Angew. Chem., Int. Ed.* **44**, 6456–6482 (2005).
- [14] Férey, G. *Chem. Soc. Rev.* **37**, 191–214 (2008).
- [15] Nørskov, J. K., Bligaard, T., Rossmeisl, J., and Christensen, C. H. *Nature Chem.* **1**, 37–46 (2009).
- [16] Senkan, S. M. *Nature* **394**, 350–353 (1998).
- [17] Schlögl, R. *Angew. Chem., Int. Ed.* **37**, 2333–2336 (1998).
- [18] Jandeleit, B., Schaefer, D. J., Powers, T. S., Turner, H. W., and Weinberg, W. H. *Angew. Chem., Int. Ed.* **38**, 2494–2532 (1999).

- [19] Greeley, J., Jaramillo, T. F., Bonde, J., Chorkendorff, I., and Nørskov, J. K. *Nature Mater.* **5**, 909–913 (2006).
- [20] Perego, C. and Villa, P. *Catal. Today* **34**, 281–305 (1997).
- [21] Campanati, M., Fornasari, G., and Vaccari, A. *Catal. Today* **77**, 299–314 (2003).
- [22] Stiles, A. B. and Koch, T. A. *Catalyst Manufacture*. Marcel Dekker Inc., New York, (1995).
- [23] Kraushaar, B. and Müller, S. P. *Synthesis of Solid Catalysts*. Wiley-VCH, Weinheim, (2009).
- [24] Deutschmann, O., Knözinger, H., Kochloefl, K., and Turek, T. *Ullmann's Encyclopedia of Industrial Chemistry*. Wiley-VCH, Weinheim, (2009).
- [25] Lloyd, L. *Handbook of Industrial Catalysts, Fundamental and Applied Catalysis*. Springer, New York, (2011).
- [26] Krishna, R. and Sie, S. *Chem. Eng. Sci.* **49**, 4029–4065 (1994).
- [27] Sie, S. T. and Krishna, R. *Rev. Chem. Eng.* **14**, 159–202 (1998).
- [28] Rase, H. F. *Handbook of Commercial Catalysts*. CRC Press, (2000).
- [29] Moulijn, J. A., Makkee, M., and van Diepen, A. *Chemical Process Technology*. Wiley-VCH, Weinheim, (2001).
- [30] Eigenberger, G. *Handbook of Heterogeneous Catalysis*. Wiley-VCH, Weinheim, (2001).
- [31] Dudukovic, M. P. *Science* **325**, 698–701 (2009).
- [32] Gallei, E. and Schwab, E. *Catal. Today* **51**, 535–546 (1999).
- [33] Bell, A. T. *Chem. Eng. Sci.* **45**, 2013–2026 (1990).
- [34] Christensen, C. H. and Nørskov, J. K. *J. Chem. Phys.* **128**, 182503/1–182503/8 (2008).
- [35] Thomas, J. M. *Chem. Eur. J.* **3**, 1557–1562 (1997).
- [36] Ertl, G. *Angew. Chem., Int. Ed.* **47**, 3524–3535 (2008).
- [37] Øygarden, A. H., Pérez-Ramírez, J., Waller, D., Schöffel, K., and Brackenbury, D. M. *Eur. Pat.*, 1,641,562 (2004).
- [38] Michels, N.-L., Mitchell, S., Milina, M., Kunze, K., Krumeich, F., Marone, F., Erdmann, M., Marti, N., and Pérez-Ramírez, J. *Adv. Funct. Mater.* **22**, 2509–2518 (2012).

- [39] van Garderen, N., Clemens, F. J., Aneziris, C. G., and Graule, T. *Ceram. Int.* **38**, 5481–5492 (2012).
- [40] Trimm, D. and Stanislaus, A. *Appl. Catal.* **21**, 215–238 (1986).
- [41] Ramsay, J. D. F., Daish, S. R., and Wright, C. J. *Faraday Discuss. Chem. Soc.* **65**, 65–75 (1978).
- [42] Lewis, J. A. *J. Am. Ceram. Soc.* **83**, 2341–2359 (2000).
- [43] Chen, Y., Burbidge, A., and Bridgwater, J. *J. Am. Ceram. Soc.* **80**, 1841–1850 (1997).
- [44] Sigmund, W. M., Bell, N. S., and Bergström, L. *J. Am. Ceram. Soc.* **83**, 1557–1574 (2000).
- [45] Lange, F. F. *J. Am. Ceram. Soc.* **72**, 3–15 (1989).
- [46] Addiego, W. P. and Liu, W. *Eur. Pat.*, 1,283,745 (2004).
- [47] Jan, D.-Y., Gehee, J. F. M., Woodle, G. B., Takayama, M., and Miller, R. M. *U.S. Pat.*, 6,376,730 (2002).
- [48] Kumar, K.-N. P., Keizer, K., Burggraaf, A., Okubo, T., Nagamoto, H., and Morooka, S. *Nature* **358**, 48–51 (1992).
- [49] Hench, L. L. and West, J. K. *Chem. Rev.* **90**, 33–72 (1990).
- [50] Freiding, J., Patcas, F.-C., and Kraushaar-Czarnetzki, B. *Appl. Catal., A* **328**, 210–218 (2007).
- [51] Vergunst, T., Kapteijn, F., and Moulijn, J. A. *Appl. Catal., A* **213**, 179–187 (2001).
- [52] Bergwerff, J. A., Visser, T., Leliveld, G., Rossenaar, B. D., de Jong, K. P., and Weckhuysen, B. M. *J. Am. Chem. Soc.* **126**, 14548–14556 (2004).
- [53] Mondelli, C., Amrute, A. P., Krumeich, F., Schmidt, T., and Pérez-Ramírez, J. *ChemCatChem* **3**, 657–660 (2011).
- [54] Corma, A. *Chem. Rev.* **97**, 2373–2420 (1997).
- [55] Rabo, J. A. and Schoonover, M. W. *Appl. Catal., A* **222**, 261–275 (2001).
- [56] Smit, B. and Maesen, T. L. *Nature* **451**, 671–678 (2008).
- [57] Valtchev, V., Majano, G., Mintova, S., and Pérez-Ramírez, J. *Chem. Soc. Rev.* **42**, 263–290 (2013).

- [58] Serrano, D. P., Sanz, R., Pizarro, P., Moreno, I., de Frutos, P., and Blázquez, S. *Catal. Today* **143**, 151–157 (2009).
- [59] Xue, N., Olindo, R., and Lercher, J. A. *J. Phys. Chem., C* **114**, 15763–15770 (2010).
- [60] Hargreaves, J. S. J. and Munnoch, A. L. *Catal. Sci. Technol.* **3**, 1165–1171 (2013).
- [61] Maselli, J. M. and Peters, A. W. *Catal. Rev.* **26**, 525–554 (1984).
- [62] Beck, W. H., Carruthers, J. D., Cornelius, E. B., Kmecak, R. A., Kovach, S. M., and Hettinger Jr., W. P. *U.S. Pat.*, 4,480,047 (1984).
- [63] Woltermann, G. M., Magee, J. S., and Griffith, S. D. *Stud. Surf. Sci. Catal.* **76**, 105–144 (1993).
- [64] Scherzer, J. *Octane-Enhancing Zeolitic FCC Catalysts*. Marcel Dekker, Inc., New York, USA, (1990).
- [65] Scherzer, J. *Stud. Surf. Sci. Catal.* **76**, 145–182 (1993).
- [66] Corma, A. and Wojciechowski, B. W. *Catal. Rev.* **27**, 29–150 (1985).
- [67] Vaughan, D. E. W. *Stud. Surf. Sci. Catal.* **76**, 83–104 (1993).
- [68] Avidan, A. A. *Stud. Surf. Sci. Catal.* **76**, 1–39 (1993).
- [69] Abdo, F. S. *Zeolites in Industrial Separation and Catalysis*. Wiley-VCH, Weinheim, Germany, (2010).
- [70] Nee, J. R. D., Harding, R. H., Yaluris, G., Cheng, W. C., Zhao, X., Dougan, T. J., and Riley, J. R. *Kirk-Othmer Encyclopedia of Chemical Technology*. Wiley-VCH, Weinheim, Germany, (2004).
- [71] Otterstedt, J.-E., Zhu, Y.-M., and Sterte, J. *Appl. Catal.* **70**, 43–52 (1991).
- [72] Corma, A., Martínez, C., and Sauvanaud, L. *Catal. Today* **127**, 3–16 (2007).
- [73] Thomas, C. L. and Barmby, D. S. *J. Catal.* **12**, 341–346 (1968).
- [74] Mitchell, M. M., Hoffman, J. F., and Moore, F. H. *Stud. Surf. Sci. Catal.* **76**, 293–338 (1993).
- [75] Perego, C. and Millini, R. *Chem. Soc. Rev.* **42**, 3956–3976 (2013).
- [76] O'Connor, P. and Humphries, A. *Prepr. - Am. Chem. Soc., Div. Pet. Chem.* **38**, 598–603 (1993).

- [77] Braithwaite, D. G., Mcgrew, E. H., Hettinger Jr., W. P., and Amico, J. D. S. *U.S. Pat.*, 3,034,995 May (1962).
- [78] Manton, M. R. and Davidtz, J. C. *J. Catal.* **60**, 156–166 (1979).
- [79] Reagan, W. J., Speronello, B. K., Brown, S. M., and Durante, V. A. *Eur. Pat.*, 117,545 (1990).
- [80] Degnan, T., Chitnis, G., and Schipper, P. *Micropor. Mesopor. Mater.* **35–36**, 245–252 (2000).
- [81] Chester, A. W., Cormier Jr., W. E., and Stover, W. A. *U.S. Pat.*, 4,309,279 (1982).
- [82] Knight, J. and Mehlberg, R. *Hydrocarbon Process., Int. Ed.*, **9**, 91–96 (2011).
- [83] Nielsen, R. H. and Doolin, P. K. *Stud. Surf. Sci. Catal.* **76**, 339–384 (1993).
- [84] McLaughlin, J., Podwirny, P. S., and Morley, J. C. *U.S. Pat.*, 5,935,890 (1999).
- [85] Lee, F.-M. *Appl. Catal., A* **82**, 215–230 (1992).
- [86] Occelli, M., Kowalczyk, D., and Kibby, C. *Appl. Catal.* **16**, 227–236 (1985).
- [87] Wakao, N. and Smith, J. M. *Chem. Eng. Sci.* **17**, 825–834 (1962).
- [88] Bedard, R. L. *Zeolites in Industrial Separation and Catalysis*. Wiley-VCH, Weinheim, Germany, (2010).
- [89] Schwarz, S., Kojima, M., and O'Connor, C. *Appl. Catal.* **68**, 81–96 (1991).
- [90] Bellussi, G., Carati, A., and Millini, R. *Zeolites and Catalysis: Synthesis, Reactions and Applications*. Wiley-VCH, Weinheim, Germany, (2010).
- [91] Sharma, S. B., Kulach, J., and Imrie, A. J. *U.S. Pat.*, 6,617,275 (2003).
- [92] Wachter, W. A. and Soled, S. L. *Eur. Pat.*, 0,635,302 (2001).
- [93] Lange, J.-P. and Mesters, C. M. *Appl. Catal., A* **210**, 247–255 (2001).
- [94] Richter, M., Fiebig, W., Jerschke, H.-G., Lischke, G., and Öhlmann, G. *Zeolites* **9**, 238–246 (1989).
- [95] Bhat, Y. S., Das, J., and Halgeri, A. B. *Appl. Catal., A* **122**, 161–168 (1995).
- [96] Klier, K. *Appl. Surf. Sci.* **19**, 267–297 (1984).
- [97] Shihabi, D. S., Garwood, W. E., Chu, P., Miale, J. N., Lago, R. M., Chu, C. T.-W., and Chang, C. D. *J. Catal.* **93**, 471–474 (1985).

- [98] Chang, C. D., Hellring, S. D., Miale, J. N., Schmitt, K. D., Brigandi, P. W., and Wu, E. L. *J. Chem. Soc., Faraday Trans.* **81**, 2215–2224 (1985).
- [99] Chu, C. T.-W., Kuehl, G. H., Lago, R. M., and Chang, C. D. *J. Catal.* **93**, 451–458 (1985).
- [100] Landau, M. V., Tavor, D., Regev, O., Kaliya, M. L., Herskowitz, M., Valtchev, V., and Mintova, S. *Chem. Mater.* **11**, 2030–2037 (1999).
- [101] Martin, A., Berndt, H., Lohse, U., and Wolf, U. *J. Chem. Soc., Faraday Trans.* **89**, 1277–1282 (1993).
- [102] Uguina, M., Sotelo, J., and Serrano, D. *Appl. Catal.* **76**, 183–198 (1991).
- [103] Absil, R. P. L., Angevine, P. J., Herbst, J. A., Klocke, D. J., Mcwilliams, J. P., Han, S., and Shihabi, D. S. *U.S. Pat.*, 5,053,374 (1991).
- [104] Marler, D. O. *U.S. Pat.*, 5,182,242 (1993).
- [105] Corma, A., Grande, M., Fornés, V., Carlidge, S., and Shatlock, M. *Appl. Catal.* **66**, 45–57 (1990).
- [106] Gélin, P. and Gueguen, C. *Appl. Catal.* **38**, 225–233 (1988).
- [107] Gélin, P. and Courières, T. D. *Appl. Catal.* **72**, 179–192 (1991).
- [108] Choudhary, V., Devadas, P., Kinage, A., and Guisnet, M. *Appl. Catal., A* **162**, 223–233 (1997).
- [109] Jasra, R. V., Tyagi, B., Badheka, Y. M., Choudary, V. N., and Bhat, T. S. G. *Ind. Eng. Chem. Res.* **42**, 3263–3272 (2003).
- [110] Canizares, P., Durán, A., Dorado, F., and Carmona, M. *Appl. Clay Sci.* **16**, 273–287 (2000).
- [111] van Donk, S., Janssen, A. H., Bitter, J. H., and de Jong, K. P. *Catal. Rev.* **45**, 297–319 (2003).
- [112] Hartmann, M. *Angew. Chem., Int. Ed.* **43**, 5880–5882 (2004).
- [113] Tosheva, L. and Valtchev, V. P. *Chem. Mater.* **17**, 2494–2513 (2005).
- [114] Tao, Y., Kanoh, H., Abrams, L., and Kaneko, K. *Chem. Rev.* **106**, 896–910 (2006).
- [115] Čejka, J. and Mintova, S. *Catal. Rev.* **49**, 457–509 (2007).
- [116] Pérez-Ramírez, J., Christensen, C. H., Egeblad, K., Christensen, C. H., and Groen, J. C. *Chem. Soc. Rev.* **37**, 2530–2542 (2008).

- [117] Egeblad, K., Christensen, C. H., Kustova, M., and Christensen, C. H. *Chem. Mater.* **20**, 946–960 (2007).
- [118] Schmidt, W. *ChemCatChem* **1**, 53–67 (2009).
- [119] Chal, R., Gérardin, C., Bulut, M., and van Donk, S. *ChemCatChem* **3**, 67–81 (2011).
- [120] Groen, J. C., Zhu, W., Brouwer, S., Huynink, S. J., Kapteijn, F., Moulijn, J. A., and Pérez-Ramírez, J. *J. Am. Chem. Soc.* **129**, 355–360 (2007).
- [121] Zhao, L., Shen, B., Gao, J., and Xu, C. *J. Catal.* **258**, 228–234 (2008).
- [122] Cho, K., Cho, H. S., de Menorval, L.-C., and Ryoo, R. *Chem. Mater.* **21**, 5664–5673 (2009).
- [123] Thibault-Starzyk, F., Stan, I., Abelló, S., Bonilla, A., Thomas, K., Fernandez, C., Gilson, J.-P., and Pérez-Ramírez, J. *J. Catal.* **264**, 11–14 (2009).
- [124] Christensen, C. H., Johannsen, K., Schmidt, I., and Christensen, C. H. *J. Am. Chem. Soc.* **125**, 13370–13371 (2003).
- [125] Choi, M., Cho, H. S., Srivastava, R., Venkatesan, C., Choi, D.-H., and Ryoo, R. *Nature Mater.* **5**, 718–723 (2006).
- [126] Pérez-Ramírez, J., Verboekend, D., Bonilla, A., and Abelló, S. *Adv. Funct. Mater.* **19**, 3972–3979 (2009).
- [127] de Jong, K. P., Zečević, J., Friedrich, H., de Jongh, P. E., Bulut, M., van Donk, S., Kenmogne, R., Finiels, A., Hulea, V., and Fajula, F. *Angew. Chem., Int. Ed.* **49**, 10074–10078 (2010).
- [128] Holm, M. S., Taarning, E., Egeblad, K., and Christensen, C. H. *Catal. Today* **168**, 3–16 (2011).
- [129] le van Mao, R., Xiao, S., Ramsaran, A., and Yao, J. *J. Mater. Chem.* **4**, 605–610 (1994).
- [130] Melian-Cabrera, I., Espinosa, S., Groen, J. C., Kapteijn, F., and Moulijn, J. A. *J. Catal.* **238**, 250–259 (2006).
- [131] Yang, J., Zhou, Y., Yang, J. Y., Lin, W. G., Wu, Y. J., Lin, N., Wang, J., and Zhu, J. H. *J. Phys. Chem., C* **114**, 9588–9595 (2010).
- [132] Groen, J. C., Peffer, L. A., Moulijn, J. A., and Pérez-Ramírez, J. *Chem. Eur. J.* **11**, 4983–4994 (2005).
- [133] Lippens, B. and de Boer, J. *J. Catal.* **4**, 319–323 (1965).

- [134] Brunauer, S., Emmett, P. H., and Teller, E. *J. Am. Chem. Soc.* **60**, 309–319 (1938).
- [135] Barrett, E. P., Joyner, L. G., and Halenda, P. P. *J. Am. Chem. Soc.* **73**, 373–380 (1951).
- [136] Ogura, M., Shinomiya, S., Tateno, J., Nara, Y., Nomura, M., Kikuchi, E., and Matsukata, M. *Appl. Catal., A* **219**, 33–43 (2001).
- [137] Groen, J. C., Moulijn, J. A., and Pérez-Ramírez, J. *J. Mater. Chem.* **16**, 2121–2131 (2006).
- [138] Verboekend, D. and Pérez-Ramírez, J. *Catal. Sci. Technol.* **1**, 879–890 (2011).
- [139] Groen, J. C., Bach, T., Ziese, U., Paulaime-van Donk, A. M., de Jong, K. P., Moulijn, J. A., and Pérez-Ramírez, J. *J. Am. Chem. Soc.* **127**, 10792–10793 (2005).
- [140] Danilina, N., Krumeich, F., Castelanelli, S. A., and van Bokhoven, J. A. *J. Phys. Chem., C* **114**, 6640–6645 (2010).
- [141] Verboekend, D. and Pérez-Ramírez, J. *ChemSusChem* **7**, 753–764 (2014).
- [142] Groen, J. C., Moulijn, J. A., and Pérez-Ramírez, J. *Ind. Eng. Chem. Res.* **46**, 4193–4201 (2007).
- [143] Louis, B., Laugel, G., Pale, P., and Pereira, M. M. *ChemCatChem* **3**, 1263–1272 (2011).
- [144] Davis, M. E. *Nature* **417**, 813–821 (2002).
- [145] Na, K., Jo, C., Kim, J., Cho, K., Jung, J., Seo, Y., Messinger, R. J., Chmelka, B. F., and Ryoo, R. *Science* **333**, 328–332 (2011).
- [146] Boissière, C., Grosso, D., Chaumonnot, A., Nicole, L., and Sanchez, C. *Adv. Mater.* **23**, 599–623 (2011).
- [147] Schüth, F. and Hesse, M. *Handbook of Heterogeneous Catalysis*. Wiley-VCH, Weinheim, Germany, (2008).
- [148] Espinosa-Alonso, L., Beale, A. M., and Weckhuysen, B. M. *Accounts Chem. Res.* **43**, 1279–1288 (2010).
- [149] Bergwerff, J. A., van de Water, L. G. A., Visser, T., de Peinder, P., Leliveld, B. R. G., de Jong, K. P., and Weckhuysen, B. M. *Chem. Eur. J.* **11**, 4591–4601 (2005).
- [150] Espinosa-Alonso, L., Lysova, A. A., Peinder, P. d., Jong, K. P. d., Koptuyug, I. V., and Weckhuysen, B. M. *J. Am. Chem. Soc.* **131**, 6525–6534 (2009).
- [151] Jacques, S. D. M., Di Michiel, M., Beale, A. M., Sochi, T., O’Brien, M. G., Espinosa-Alonso, L., Weckhuysen, B. M., and Barnes, P. *Angew. Chem., Int. Ed.* **50**, 10148–10152 (2011).

- [152] O'Brien, M. G., Jacques, S. D. M., Di Michiel, M., Barnes, P., Weckhuysen, B. M., and Beale, A. M. *Chem. Sci.* **3**, 509–523 (2012).
- [153] Valtchev, V., Balanzat, E., Mavrodinova, V., Diaz, I., El Fallah, J., and Goupil, J.-M. *J. Am. Chem. Soc.* **133**, 18950–18956 (2011).
- [154] Jiang, J., Jorda, J. L., Yu, J., Baumes, L. A., Mugnaioli, E., Diaz-Cabanas, M. J., Kolb, U., and Corma, A. *Science* **333**, 1131–1134 (2011).
- [155] Pérez-Ramírez, J., Mitchell, S., Verboekend, D., Milina, M., Michels, N.-L., Krumeich, F., Marti, N., and Erdmann, M. *ChemCatChem* **3**, 1731–1734 (2011).
- [156] Groen, J. C., Peffer, L. A., and Pérez-Ramírez, J. *Micropor. Mesopor. Mater.* **60**, 1–17 (2003).
- [157] Zečević, J., Gommès, C. J., Friedrich, H., de Jongh, P. E., and de Jong, K. P. *Angew. Chem., Int. Ed.* **51**, 4213–4217 (2012).
- [158] Friedrich, H., de Jongh, P. E., Verkleij, A. J., and de Jong, K. P. *Chem. Rev.* **109**, 1613–1629 (2009).
- [159] Bjørgen, M., Joensen, F., Holm, M. S., Olsbye, U., Lillerud, K.-P., and Svelle, S. *Appl. Catal., A* **345**, 43–50 (2008).
- [160] Kim, J., Choi, M., and Ryoo, R. *J. Catal.* **269**, 219–228 (2010).
- [161] Roeffaers, M. B. J., de Cremer, G., Libeert, J., Ameloot, R., Dedecker, P., Bons, A.-J., Bückins, M., Martens, J. A., Sels, B. F., de Vos, D. E., and Hofkens, J. *Angew. Chem., Int. Ed.* **48**, 9285–9289 (2009).
- [162] de Cremer, G., Sels, B. F., de Vos, D. E., Hofkens, J., and Roeffaers, M. B. J. *Chem. Soc. Rev.* **39**, 4703–4717 (2010).
- [163] Buurmans, I. L., Ruiz-Martínez, J., Knowles, W. V., van der Beek, D., Bergwerff, J. A., Vogt, E. T., and Weckhuysen, B. M. *Nature Chem.* **3**, 862–867 (2011).
- [164] Epting, W. K., Gelb, J., and Litster, S. *Adv. Funct. Mater.* **22**, 555–560 (2012).
- [165] Wilson, J. R., Kobsiriphat, W., Mendoza, R., Chen, H.-Y., Hiller, J. M., Miller, D. J., Thornton, K., Voorhees, P. W., Adler, S. B., and Barnett, S. A. *Nature Mater.* **5**, 541–544 (2006).
- [166] Hintermüller, C., Marone, F., Isenegger, A., and Stampanoni, M. *J. Synchrotron Radiat.* **17**, 550–559 (2010).

- [167] Stampanoni, M., Mokso, R., Marone, F., Vila-Comamala, J., Gorelick, S., Trtik, P., Jefimovs, K., and David, C. *Phys. Rev. B* **81**, 140105/1–140105/4 (2010).
- [168] Karwacki, L., de Winter, D. A. M., Aramburo, L. R., Lebbink, M. N., Post, J. A., Drury, M. R., and Weckhuysen, B. M. *Angew. Chem., Int. Ed.* **50**, 1294–1298 (2011).
- [169] Anderson, M. W., Ohsuna, T., Sakamoto, Y., Liu, Z., Carlsson, A., and Terasaki, O. *Chem. Commun.* **8**, 907–916 (2004).
- [170] Yuan, P., Sun, J., Xu, H., Zhou, L., Liu, J., Zhang, D., Wang, Y., Jack, K. S., Drennan, J., Zhao, D., Lu, G., Zou, X., Zou, J., and Yu, C. *Chem. Mater.* **23**, 229–238 (2011).
- [171] Ortalan, V., Uzun, A., Gates, B. C., and Browning, N. D. *Nature Nanotechnol.* **5**, 506–510 (2010).
- [172] Midgley, P. A. and Dunin-Borkowski, R. E. *Nature Mater.* **8**, 271–280 (2009).
- [173] Gommers, C. J., Friedrich, H., Wolters, M., de Jongh, P. E., and de Jong, K. P. *Chem. Mater.* **21**, 1311–1317 (2009).
- [174] Mitchell, S., Michels, N.-L., and Pérez-Ramírez, J. *Chem. Soc. Rev.* **42**, 6094–6112 (2013).
- [175] Hölderich, W., Einhorn, H., Lehnert, R., Marosi, R., Mross, W., Reinke, R., Ruppel, W., and Schlimper, H. *Proceedings of the Sixth International Zeolite Conference*. Butterworths, Reno, NV, USA, (1983).
- [176] Howden, M. G. and Müller, W. P. *Stud. Surf. Sci. Catal.* **84**, 1739–1747 (1994).
- [177] Patcas, F. *J. Catal.* **231**, 194–200 (2005).
- [178] Lee, K.-Y., Lee, H.-K., and Ihm, S.-K. *Top. Catal.* **53**, 247–253 (2010).
- [179] Freiding, J. and Kraushaar-Czarnetzki, B. *Appl. Catal., A* **391**, 254–260 (2011).
- [180] Mitchell, S., Michels, N.-L., Kunze, K., and Pérez-Ramírez, J. *Nature Chem.* **4**, 825–831 (2012).
- [181] Dahl, I. and Kolboe, S. *Catal. Lett.* **20**, 329–336 (1993).
- [182] Olsbye, U., Svelle, S., Bjørgen, M., Beato, P., Janssens, T. V. W., Joensen, F., Bordiga, S., and Lillerud, K. P. *Angew. Chem., Int. Ed.* **51**, 5810–5831 (2012).
- [183] Chang, C. D., Chu, C. T.-W., and Socha, R. F. *J. Catal.* **86**, 289–296 (1984).
- [184] Dessau, R. *J. Catal.* **99**, 111–116 (1986).
- [185] Svelle, S., Joensen, F., Nerlov, J., Olsbye, U., Lillerud, K.-P., Kolboe, S., and Bjørgen, M. *J. Am. Chem. Soc.* **128**, 14770–14771 (2006).

- [186] Bjørgen, M., Svelle, S., Joensen, F., Nerlov, J., Kolboe, S., Bonino, F., Palumbo, L., Bordiga, S., and Olsbye, U. *J. Catal.* **249**, 195–207 (2007).
- [187] Howden, M. G., Botha, J. J. C., and Scurrall, M. S. *Chem. Ind.-Lond.* **46**, 391–407 (1992).
- [188] Romannikov, V., Chumachenko, L., Mastikhin, V., and Ione, K. *React. Kinet. Catal. Lett.* **29**, 85–91 (1985).
- [189] Dyballa, M., Klemm, E., Weitkamp, J., and Hunger, M. *Chem. Ing. Tech.* **85**, 1719–1725 (2013).
- [190] Mentzel, U. V., Højholt, K. T., Holm, M. S., Fehrmann, R., and Beato, P. *Appl. Catal., A* **417–418**, 290–297 (2012).
- [191] McIntosh, R. J. and Seddon, D. *Appl. Catal.* **6**, 307–314 (1983).
- [192] Lévesque, P., Bianchi, D., le van Mao, R., and Pajonk, G. M. *Appl. Catal.* **57**, 31–43 (1990).
- [193] Aramburo, L. R., de Smit, E., Arstad, B., van Schooneveld, M. M., Sommer, L., Juhin, A., Yokosawa, T., Zandbergen, H. W., Olsbye, U., de Groot, F. M. F., and Weckhuysen, B. M. *Angew. Chem., Int. Ed.* **51**, 3616–3619 (2012).
- [194] Tynjälä, P. and Pakkanen, T. T. *J. Mol. Catal., A* **122**, 159–168 (1997).
- [195] Vennestrøm, P. N., Grill, M., Kustova, M., Egeblad, K., Lundegaard, L. F., Joensen, F., Christensen, C. H., and Beato, P. *Catal. Today* **168**, 71–79 (2011).
- [196] Qin, Z., Lakiss, L., Tosheva, L., Gilson, J.-P., Vicente, A., Fernandez, C., and Valtchev, V. *Adv. Funct. Mater.* **24**, 257–264 (2014).
- [197] Emeis, C. *J. Catal.* **141**, 347–354 (1993).
- [198] Gueudré, L., Milina, M., Mitchell, S., and Pérez-Ramírez, J. *Adv. Funct. Mater.* **24**, 209–219 (2014).
- [199] Chmelik, C. and Kärger, J. *Chem. Soc. Rev.* **39**, 4864–4884 (2010).
- [200] Barrios, M. S., González, L. V. F., Rodríguez, M. A. V., and Pozas, J. M. M. *Appl. Clay Sci.* **10**, 247–258 (1995).
- [201] Kärger, J., Binder, T., Chmelik, C., Hibbe, F., Krautscheid, H., Krishna, R., and Weitkamp, J. *Nature Mater.* **13**, 333–343 (2014).
- [202] Du, J., Lai, X., Yang, N., Zhai, J., Kisailus, D., Su, F., Wang, D., and Jiang, L. *ACS Nano* **5**, 590–596 (2010).

- [203] Lu, A.-H. and Schüth, F. *Adv. Mater.* **18**, 1793–1805 (2006).
- [204] Fedina, I., Litovsky, E., Shapiro, M., and Shavit, A. *J. Am. Ceram. Soc.* **80**, 2100–2108 (1997).
- [205] Vatcha, S. R. *Colloids Surf., A* **133**, 99–105 (1998).
- [206] Mears, D. E. *J. Catal.* **20**, 127–131 (1971).
- [207] Lang, R., Westerfeld, T., Gerlich, A., and Knoche, K. F. *Adsorption* **2**, 121–132 (1996).
- [208] Pino, L., Aristov, Y., Cacciola, G., and Retuccia, G. *Adsorption* **3**, 33–40 (1997).
- [209] Purewal, J. J., Liu, D., Sudik, A., Veenstra, M., Yang, J., Maurer, S., Mueller, U., Ni, J., and Siegel, D. J. *J. Phys. Chem., C* **116**, 20199–20212 (2012).
- [210] Bartholomew, C. H. *Appl. Catal., A* **212**, 17–60 (2001).
- [211] Peralta, M. A., Gross, M. S., Ulla, M. A., and Querini, C. A. *Appl. Catal., A* **367**, 59–69 (2009).
- [212] Tritt, T. M. *Thermal Conductivity - Theory, Properties, and Application*. Kluwer Academic/Plenum Publisher, New York, (2004).
- [213] Chen, G. *Int. J. Therm. Sci.* **39**, 471–480 (2000).
- [214] Sheng, M., Yang, H., Cahela, D. R., and Tatarchuk, B. J. *J. Catal.* **281**, 254–262 (2011).
- [215] Watari, K., Nakano, H., Sato, K., Urabe, K., Ishizaki, K., Cao, S., and Mori, K. *J. Am. Ceram. Soc.* **86**, 1812–1814 (2003).
- [216] Ledoux, M. J., Crouzet, C., Pham-Huu, C., Turines, V., Kourtakis, K., Mills, P. L., and Lerou, J. J. *J. Catal.* **203**, 495–508 (2001).
- [217] Liu, H.-M. and He, D.-H. *J. Phys. Chem., C* **114**, 13716–13721 (2010).
- [218] Balandin, A. A. *Nature Mater.* **10**, 569–581 (2011).
- [219] Kaur, S., Raravikar, N., Helms, B. A., Prasher, R., and Ogletree, D. F. *Nature Commun.* **5**, 1–8 (2014).
- [220] Huxtable, S. T., Cahill, D. G., Shenogin, S., Xue, L., Ozisik, R., Barone, P., Usrey, M., Strano, M. S., Siddons, G., Shim, M., et al. *Nature Mater.* **2**, 731–734 (2003).
- [221] Ghosh, S., Bao, W., Nika, D. L., Subrina, S., Pokatilov, E. P., Lau, C. N., and Balandin, A. A. *Nature Mater.* **9**, 555–558 (2010).

- [222] Ryu, J.-H., Lee, K.-Y., Kim, H.-J., Yang, J.-I., and Jung, H. *Appl. Catal., B* **80**, 306–312 (2008).
- [223] Ryu, J.-H., Lee, K.-Y., La, H., Kim, H.-J., Yang, J.-I., and Jung, H. *J. Power Sources* **171**, 499–505 (2007).
- [224] Liu, Y., Ersen, O., Meny, C., Luck, F., and Pham-Huu, C. *ChemSusChem* **7**, 1218–1239 (2014).
- [225] Ivanova, S., Louis, B., Madani, B., Tessonnier, J., Ledoux, M., and Pham-Huu, C. *J. Phys. Chem., C* **111**, 4368–4374 (2007).
- [226] Smith, D. S., Alzina, A., Bourret, J., Nait-Ali, B., Penneç, F., Tessier-Doyen, N., Otsu, K., Matsubara, H., Elser, P., and Gonzenbach, U. T. *J. Mater. Res.* **28**, 2260–2272 (2013).
- [227] Mitchell, S., Michels, N.-L., Majano, G., and Pérez-Ramírez, J. *Curr. Opin. Chem. Eng.* **2**, 304–311 (2013).
- [228] Chung, D. D. L. *Appl. Therm. Eng.* **21**, 1593–1605 (2001).
- [229] Berger, R. J., Pérez-Ramírez, J., Kapteijn, F., and Moulijn, J. A. *Appl. Catal., A* **227**, 321–333 (2002).
- [230] Holzwarth, A., Schmidt, H.-W., and Maier, W. F. *Angew. Chem., Int. Ed.* **37**, 2644–2647 (1998).
- [231] Seyler, M., Selzner, C., Holzapfel, C., Mücklich, F., and Maier, W. F. *Adv. Funct. Mater.* **18**, 1178–1185 (2008).
- [232] Bleken, F., Skistad, W., Barbera, K., Kustova, M., Bordiga, S., Beato, P., Lillerud, K. P., Svelle, S., and Olsbye, U. *Phys. Chem. Chem. Phys.* **13**, 2539–2549 (2011).

Appendix A

Annexes

Chapter 2

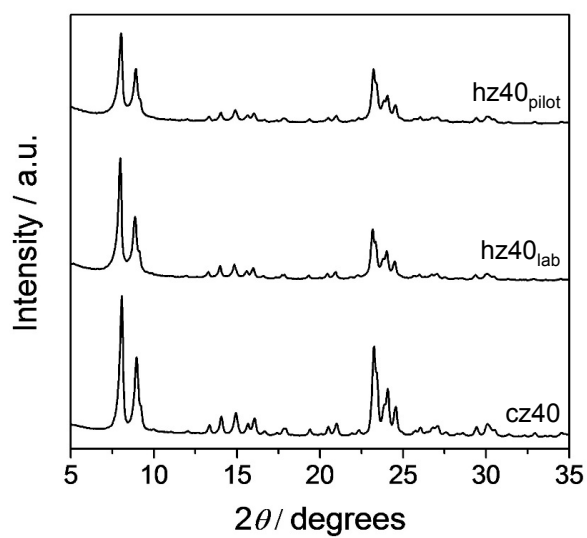


Figure A.1. Powder X-ray diffraction patterns of the zeolites acquired in a PANalytical X'Pert PRO-MPD diffractometer equipped with an X'Celerator linear detection system. The long-range crystallinity in the parent zeolite is preserved upon mesoporosity introduction by alkaline treatment.

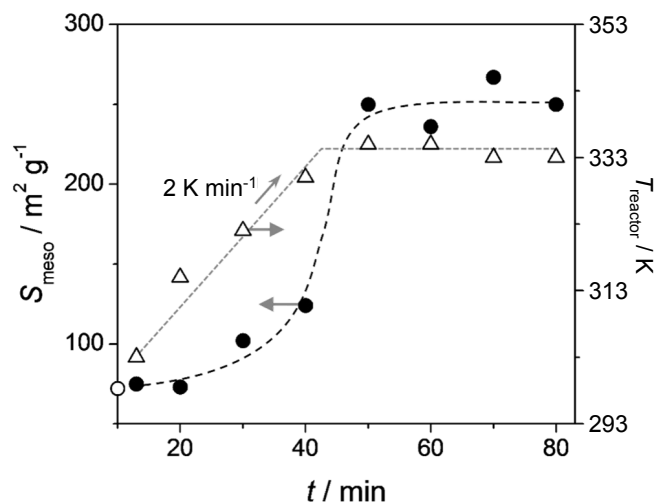


Figure A.2. Temperature profile (open triangles) and corresponding variation in zeolite mesopore surface area (S_{meso} , solid circles) during alkaline treatment in a 50 L reactor (mid scale). Slurry probes (50 cm^3) were taken at regular, quenched in ice, and the zeolite was isolated by filtration, washed, and dried, prior to characterization by N_2 adsorption. The open circle on the left y-axis corresponds to the S_{meso} of the conventional ZSM-5. Most of the mesoporosity during alkaline treatment is developed in the ramping of the temperature, while practically no porosity changes occur in the isothermal period.

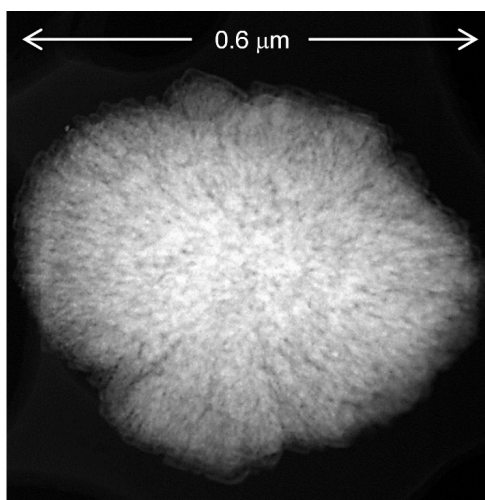


Figure A.3. Dark-field scanning transmission electron microscopy (STEM) image of the mesoporous zeolite prepared in the pilot reactor ($\text{hz40}_{\text{pilot}}$). STEM was undertaken using an aberration-corrected HD-2700CS microscope (Hitachi) operated at 200 kV. The uniform mesoporosity distribution along the crystal aggregate can be clearly seen.

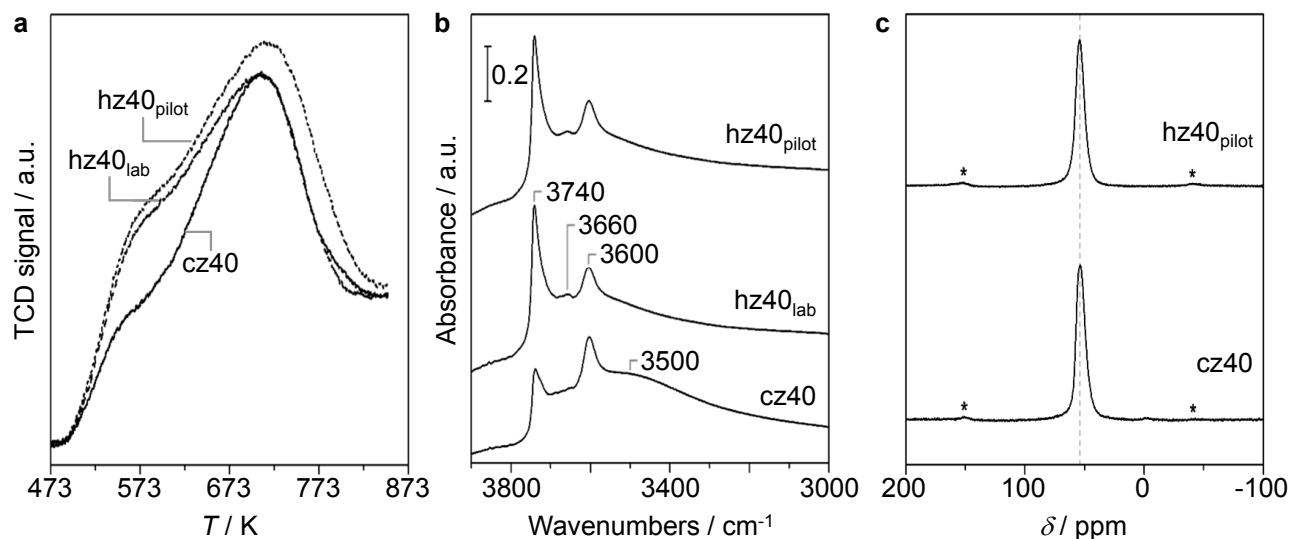


Figure A.4. (a) NH_3 -TPD of the zeolites. Alkaline treatment leads to an increased intensity of the low-temperature desorption peak (shoulder at 600 K), which is attributed to the increased presence of Lewis acid sites. No significant variation is observed in the high-temperature desorption peak, primarily associated with strong Brønsted acid sites. (b) FTIR of the zeolites in the hydroxyl-stretching region. Alkaline treatment of cz40 leads to an increased presence of isolated external silanol groups (3740 cm^{-1}), and a reduced amount of interacting silanol groups associated with internal defects (3500 cm^{-1}), while little variation in strong Brønsted acid sites (3600 cm^{-1}), or in the band, which has recently been ascribed to partially hydrolyzed framework Al (3660 cm^{-1}), is observed. No evidence of extraframework Al (3780 cm^{-1}) is visible. Band assignments were taken from ref. [232]. (c) ^{27}Al MAS NMR spectra of the cz40 and hz40_{pilot} zeolites. Asterisks indicate positions of spinning side bands. The single dominant peak at 55 ppm is characteristic of tetrahedral Al in lattice positions of the zeolite. No peak at 0 ppm, typical of octahedral Al in extraframework positions, was identified.

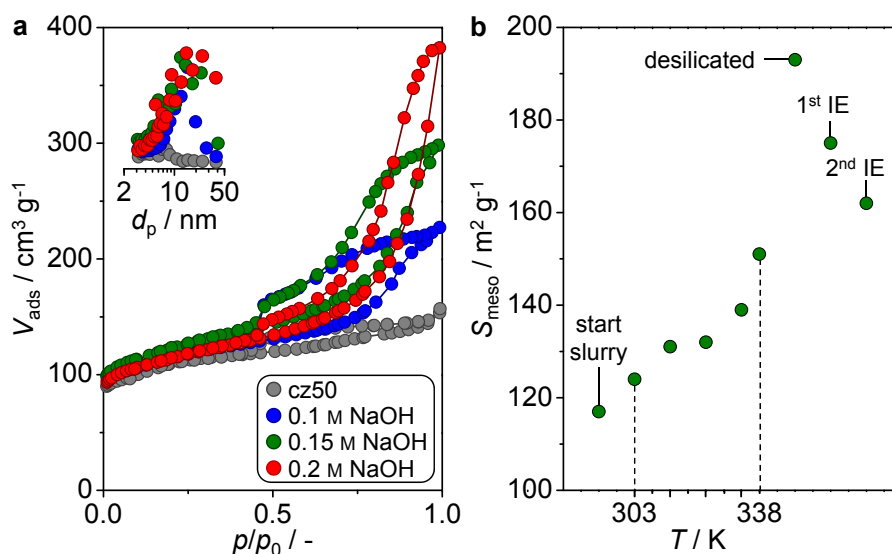


Figure A.5. (a) Validation of the effect of NaOH concentration prior to the plant trial. N_2 isotherms of the conventional zeolite (cz50) and its hierarchical analogues desilicated under varying alkalinity. (b) Evolution of the external surface area (S_{meso}) at industrial scale, evidencing the majority of the mesopore development occurring after the heating step.

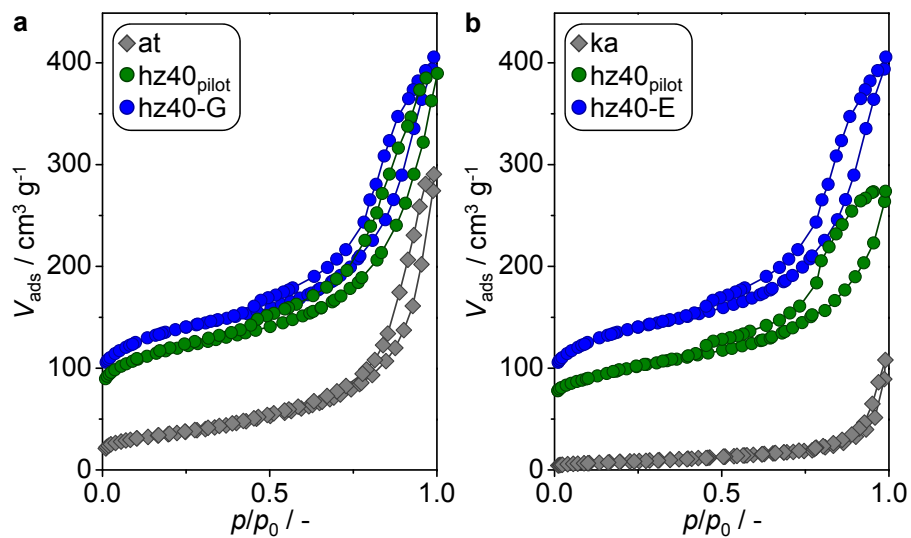


Figure A.6. Nitrogen isotherms of the hierarchical zeolite (a) granule (hz40-G) and (b) extrudate (hz40-E), and their respective component phases. All the samples were measured in the calcined form. The enhanced porous properties of the hierarchical zeolite obtained by alkaline treatment was affected neither by the presence of the binder nor by the shaping process.

Chapter 3

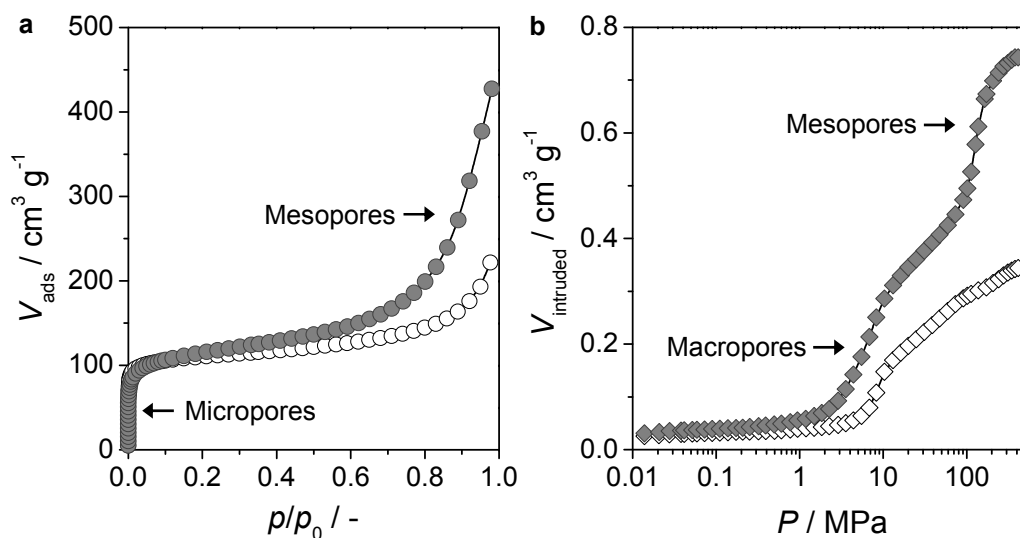


Figure A.7. (a) High-resolution low-pressure argon isotherms at 87 K and (b) mercury intrusion curves at 298 K of conventional (open symbols) and hierarchical (solid symbols) ZSM-5 granules. The increased Ar uptake and Hg intrusion, due to the presence of intra-zeolitic mesopores in the hierarchical body, is clearly observed. Equivalent results were obtained over ZSM-5 extrudates.

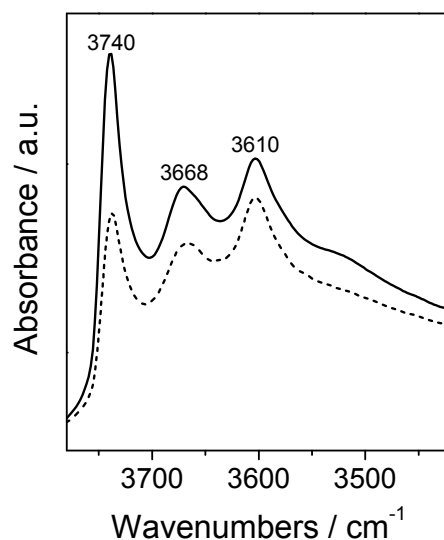


Figure A.8. Infrared spectra in the OH-stretching region of the conventional (dashed line) and hierarchical (solid line) ZSM-5 granules. The hierarchical sample shows an increased band associated with isolated silanols (3740 cm^{-1}) due to the increased external surface area, with a preserved Brønsted acidity (band at 3600 cm^{-1}). The absorption at 3668 cm^{-1} arises from hydroxyl stretches related to the binder. Equivalent results were obtained over ZSM-5 extrudates.

Chapter 4

Table A.1. Characterization and performance data of the calcined binders in powder form.

Binder	S_{meso}^a [m ² g ⁻¹]	V_{meso}^b [cm ³ g ⁻¹]	c_B^d [μmol g ⁻¹]	c_L^d [μmol g ⁻¹]	$X(\text{CH}_3\text{OH})^e$ [%]	$S(\text{CH}_3\text{OCH}_3)^e$ [Cmol.%]	$S(\text{C}_1)^e$ [Cmol.%]
si	172	0.52 (0.52) ^c	0	0	0	0	0
bo	182	0.37 (0.26)	0	94	90	41	32
ka	30	0.10 (0.10)	0	8	38	100	0
at	125	0.41 (0.29)	0	19	79	100	0

^a *t*-plot method; ^b $V_{\text{meso}} = V_{\text{pore}} - V_{\text{micro}}$; ^c In parenthesis, volume of Hg intruded into pores of 3.7–50 nm diameter; ^d Concentration of Brønsted (c_B) or Lewis (c_L) acid sites derived from the IR study of adsorbed pyridine; ^e MTH reaction studied at $T = 723$ K, $P = 1$ bar, and $\text{WHSV} = 9.5 \text{ g}_{\text{methanol}} \text{ g}_{\text{catalyst}}^{-1} \text{ h}^{-1}$.

Table A.2. Average product selectivity over the conventional and hierarchical ZSM-5 powders (P), and physical (PM), and extruded (E) binder-containing admixtures during a single cycle.

Sample	Form	Selectivity ^a [Cmol.%]							
		C ₁	C ₂ ⁼	C ₃ ⁼	C ₄ ⁼	C ₄	C _{5–7}	C _{6–8}	C ₉₊
cz40	P	7	9	19	11	14	22	15	1
hz40	P	5	7	22	11	15	26	10	2
hz40-si	E	5	7	18	8	15	29	12	2
hz40-bo	E	9	7	14	6	17	29	12	4
hz40-ka	E	4	7	22	13	13	26	10	2
hz40-at	E	3	7	30	14	11	28	5	1
hz40-at	PM	4	7	22	11	14	28	11	2

^a MTH reaction studied at $T = 723$ K, $P = 1$ bar, and $\text{WHSV} = 9.5 \text{ g}_{\text{methanol}} \text{ g}_{\text{catalyst}}^{-1} \text{ h}^{-1}$.

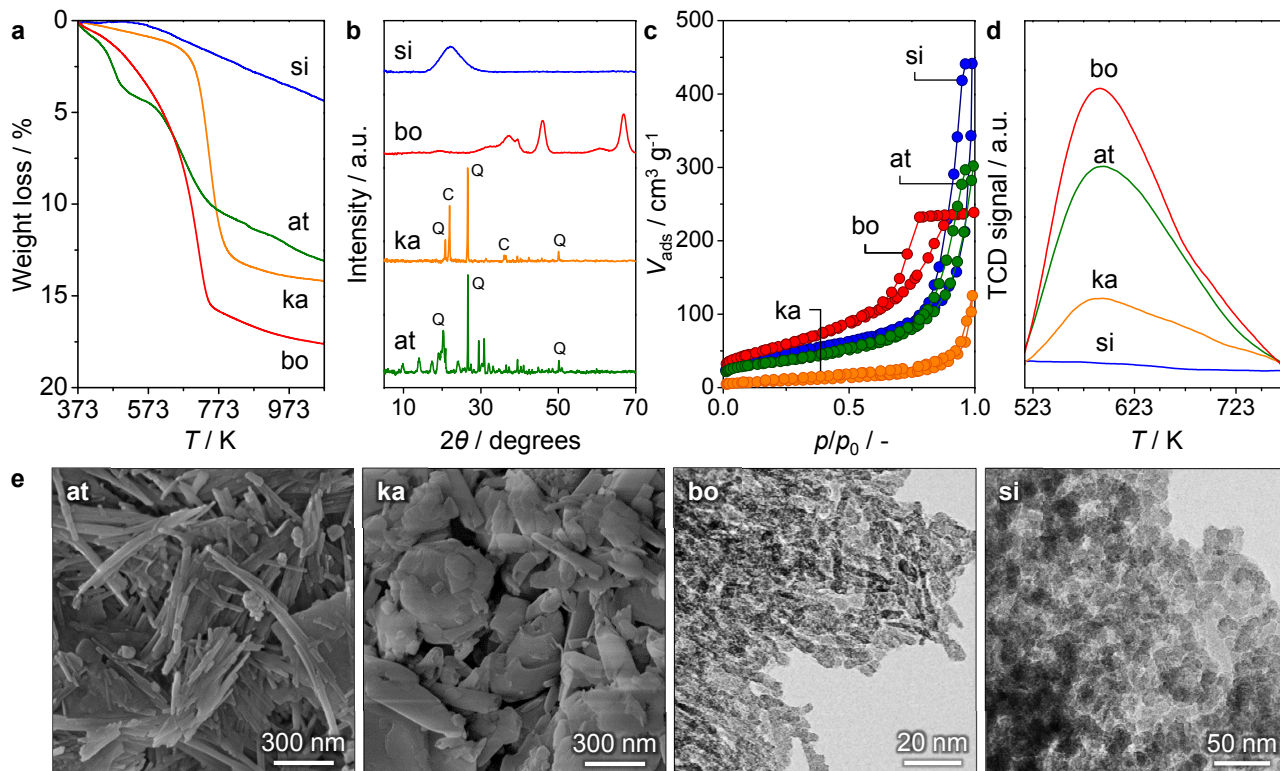


Figure A.9. (a) TG profiles of the as received binders, exhibiting weight losses characteristic of the dehydration of physisorbed H_2O (below 400 K), the progressive removal of bound H_2O , and/or the irreversible dehydroxylation at higher temperatures. (b) X-ray diffractograms of the binders after calcination at 873 K are attributed to the presence of a predominantly amorphous SiO_2 phase, a $\gamma\text{-Al}_2\text{O}_3$ phase, and amorphous mixed metal oxide phases (kaolin and attapulgite) containing small amounts of crystalline quartz (Q) and cristobalite- β (C) impurities (marked), respectively. (c) N_2 isotherms of the calcined binders. (d) NH_3 -TPD profiles of the calcined binders reveal an appreciable desorption peak at low temperature (*ca.* 580 K) due to weak acidity in the case of boehmite, kaolin and attapulgite. (e) SEM images of calcined attapulgite and kaolin powders showing their respective particle morphologies. TEM micrographs of the calcined boehmite and silica phases.

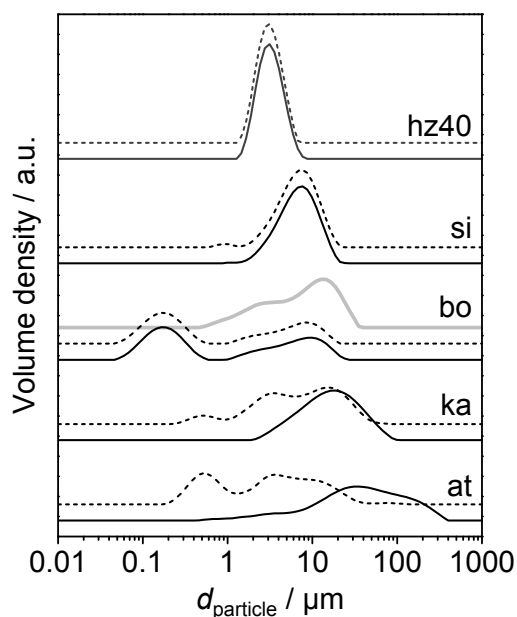


Figure A.10. Particle size distributions determined by laser diffraction (Malvern Mastersizer 3000) of water dispersed hierarchical ZSM-5 and binders before (solid) and after ultrasonication (dashed). The thick grey line shown in the case of boehmite represents its state prior to peptization.

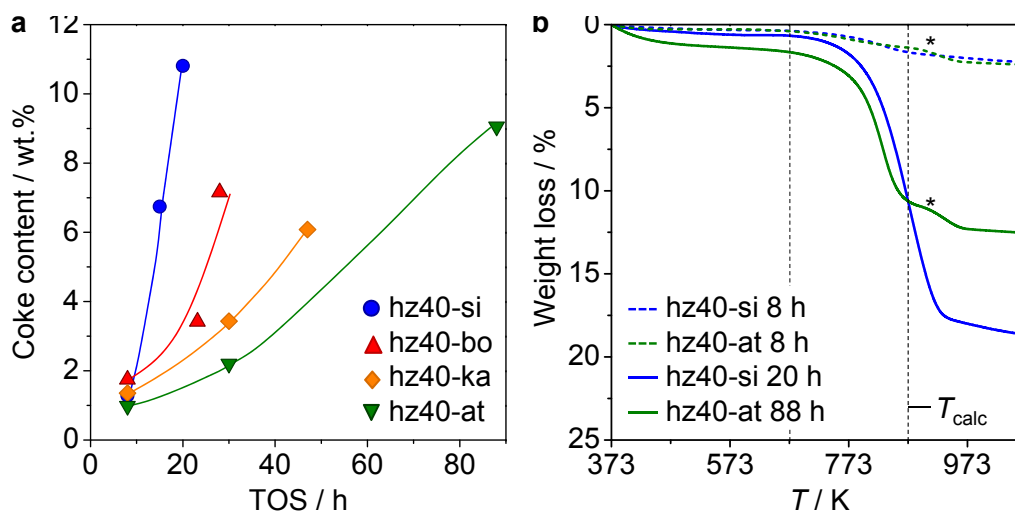


Figure A.11. (a) Coke content and (b) selected corresponding TG profiles of the binder containing hierarchical ZSM-5 extrudates *vs.* time-on-stream at $T = 723$ K and $WHSV = 9.5 \text{ g}_{\text{methanol}} \text{ g}_{\text{zeolite}}^{-1} \text{ h}^{-1}$. The trendlines in (a) are drawn for guidance only. The coke content in the used catalysts was assessed by the percentage weight loss in the range of 673–873 K, the latter corresponding to the calcination temperature, T_{calc} . The asterisk in (b) represents the weight loss characteristic of the dehydroxylation of attapulgite.

Chapter 5

Experimental

Method. The thermal conductivity of solids can be measured by either steady-state or transient approaches. In the former, heat is applied to one side of the sample and discharged at the opposite side, leading to a temperature gradient in the direction of heat flux. The effective thermal conductivity k_{eff} ($\text{W m}^{-2} \text{K}^{-1}$) is determined by measuring the temperature at (a minimum of) two different points within the sample according to Equation A.1, where q (W) is the heat input per unit time, Δx (m) is the distance between the temperature sensors, A (m^2) is the area and ΔT (K) is the absolute temperature difference between the sensors. However, this method requires long equilibrium times and large sample dimensions (such as packed beds) to guarantee an appropriate distance between the temperature sensors.

$$k_{\text{eff}} = -\frac{q \cdot \Delta x}{A \cdot \Delta T} \quad (\text{A.1})$$

In transient approaches, a thermal disturbance is introduced into a thermally equilibrated system by a singular (or periodic) heat impulse that spreads through the sample with a certain speed, the decay of which is detected by a temperature sensor. Laser Flash techniques, for example, use a short laser impulse to heat the front side of a planar sample. The time-dependency of the heat propagation to the backside of the sample is detected by an infrared detector. The thermal conductivity is indirectly determined by measuring the thermal diffusivity α ($\text{m}^2 \text{s}^{-1}$), which can be converted according to Equation A.2, where c_p ($\text{J kg}^{-1} \text{K}^{-1}$) is the specific heat capacity at constant pressure and ρ (kg m^3) is the effective density of the material. However, this technique is only applicable to thin specimen (as films or membranes).

$$k_{\text{eff}} = \alpha \cdot \rho \cdot c_p \quad (\text{A.2})$$

A transient hot-plate approach combining the advantages of the prior techniques, permits the convenient assessment of thermal conductivity over a wide range of length scales. For this study, we used the TPS 2500S Thermal Constants Analyzer (Hot Disk), to quantify the thermal conductivity of individual millimeter-sized catalyst bodies and packed catalyst

beds. The operating principle utilizes thin resistance sensors in which a double nickel spiral is mechanically-supported between two insulating layers of mica, which enables measurement up to 750 K. To get a representative overview of a multiphasic sample (such as a porous composite material or a packed bed), the diameter of the sensor should be at least ten times larger than the size of the largest individual phase (that is the pore, the single body, or the grain, respectively). Furthermore, it is necessary to ensure that there is enough sample on all sides of the sensor to minimize any influence from the surroundings during the measurement. To guarantee the latter, the depth probed Δp (m) can be estimated according to Equation A.3. Herein, α ($\text{m}^2 \text{s}^{-1}$) is the thermal diffusivity and t (s) is the total time of the transient recording. The constant c depends on the sensitivity of the method, but in most practical situations can be fixed at a value of 2.

$$\Delta p = c \cdot \sqrt{\alpha t} \quad (\text{A.3})$$

To investigate the thermal conductivity of individual catalyst bodies and packed beds, single phase powders or physical mixtures comprising the zeolite and additive phases were shaped by either dry pressing into uniform cylindrical pellets (20 mm diameter, 2 mm height) at 10 bar for 5 min using a Specac press (Patman Instrument AG) or by extrusion (Mini Screw Extruder, Caleva) into cylindrical extrudates (2 mm diameter, 5 mm length), respectively (Figure A.17).

In a typical measurement over a single body, the resistance sensor (6.4 mm diameter) was fixed between two pellets of the desired composition, located within a thermally-insulated oven and heated to the desired temperature. Similarly, the thermal conductivity of a bed of extrudates was determined by fixing a larger sensor (29.2 mm diameter) between two hollow cylindrical containers (stainless steel, 60 mm diameter, 25 mm height) filled with extrudates. Prior to testing, the apparatus was thermally-equilibrated for 90 min. The total electrical power P_0 (W) was adjusted to achieve a temperature increase ΔT (K) between 0.5–2 K over the measurement duration. The temperature rise was controlled in order to ensure that the heat wave did not exceed the sample edges. Typically, 30 mW for 3 s was found to be suitable. The sensor records the temperature change over time (approximately 200 data points) and thermal conductivity was calculated from the slope of Equation A.4, where a is the radius of

the sensor (m) and $D(\tau)$ is the time function (s).

$$\Delta T = \frac{P_0}{\pi^{\frac{3}{2}} \cdot a \cdot k_{\text{eff}}} \cdot D(\tau) \quad (\text{A.4})$$

The sensor resistivity influences the resolution and accuracy of the measured temperature increase. Although sensor materials like Kapton have lower resistivities compared to mica, they are limited to application only up to 450 K. For comparability, mica sensors were used for all experiments over the temperature range of 298–723 K. The relatively larger standard deviation for the thermal conductivity of graphite containing samples ($\sigma = 0.5 \text{ W m}^2 \text{ K}^{-1}$) originates from their high thermal diffusivity, which permitted only the minimum measurement duration (1 s). Due to the small temperature changes studied (0.5–2 K), fluctuations in the oven temperature, such as the periodic heat pulses may influence the accuracy. Therefore, each measurement was conducted at least 5 times, with a 15 min interval to allow for the complete thermal relaxation of the material. The standard deviation (σ) was reported as the error of each measurement.

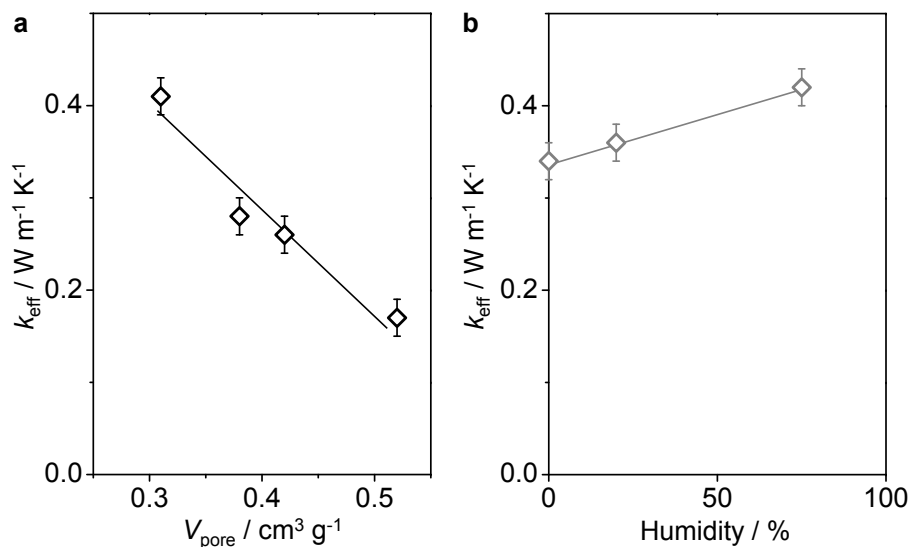


Figure A.12. The effective thermal conductivity as a function of a) the pore volume of the additive free zeolite body determined by mercury porosimetry and b) the degree of sample hydration. The former was decreased by increasing the degree of compaction during the pelletization, while the latter was varied by ageing the sample for in vacuum or at 75% relative humidity for 24 h.

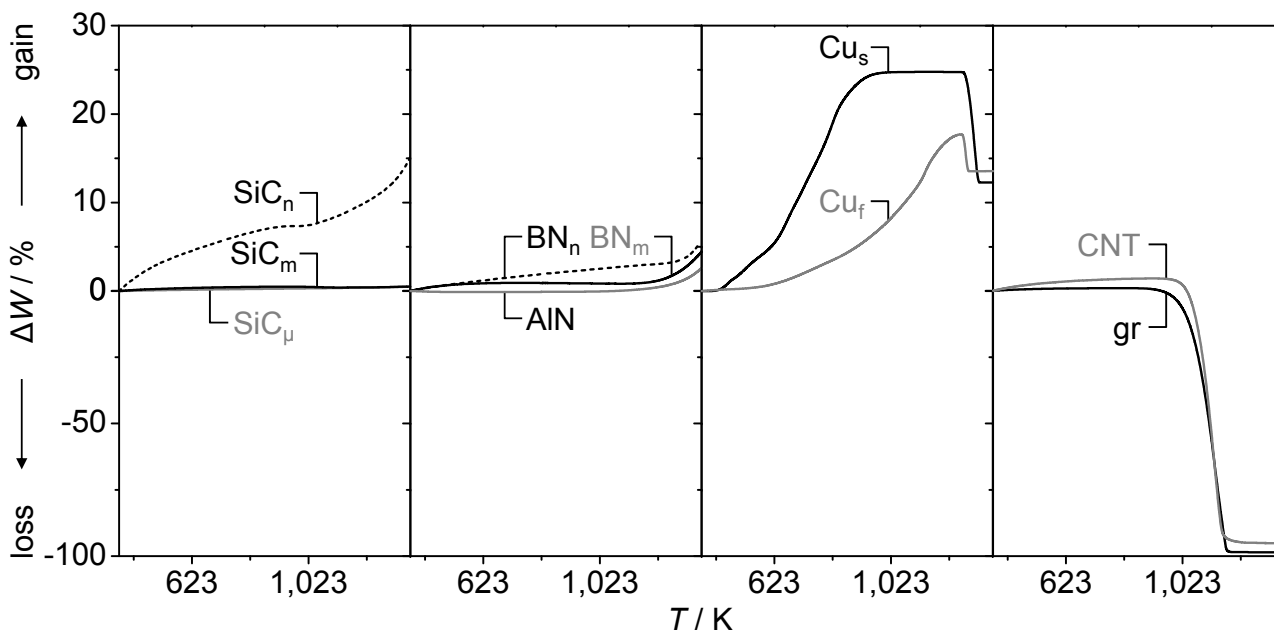


Figure A.13. The weight loss or gain evidenced over the conductive additives by thermogravimetry upon heating (10 K min^{-1}) in air ($50 \text{ cm}^3 \text{ min}^{-1}$). As expected, the ceramics exhibit a high thermal stability under the conditions studied, except for the nano-sized forms of silicon carbide and, to a lesser extent, boron nitride, which exhibit appreciable weight gains resulting from oxidation at high temperature due to their high surface areas. The copper particles are fully oxidized as the temperature increases, before being reduced at higher temperature. In contrast, the carbon nanotubes and graphite undergo oxidative combustion in a single decomposition step above 1000 K.

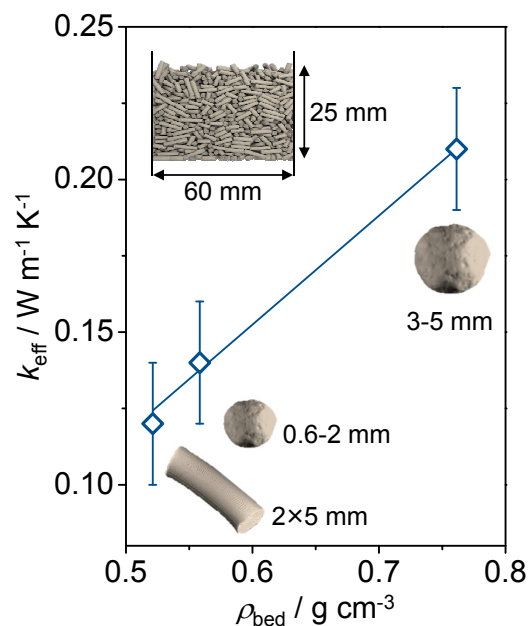


Figure A.14. Variation of the effective thermal conductivity of additive-free zeolite catalyst beds of extrudates or granules as a function of the bed density. Granules of different size (0.6–2 and 3–5 mm diameter) were shaped by agglomeration using a pan granulator (1:4 zeolite:binder mass ratio).

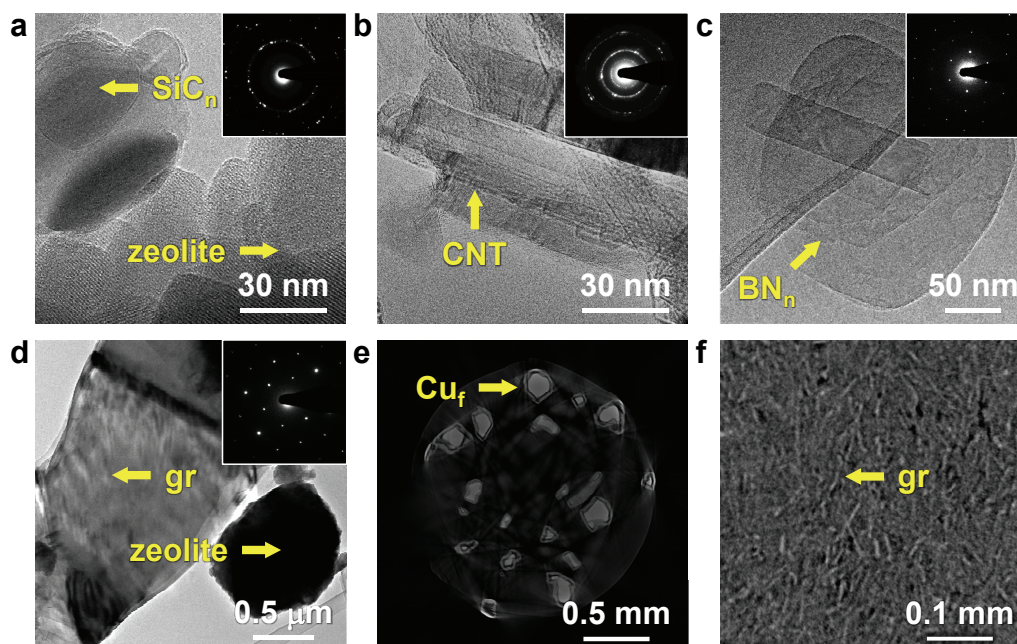


Figure A.15. Transmission electron micrographs of the crushed zeolite bodies confirm the pseudo spherical, rod-, or sheet-like morphology of the SiCn (a), CNT (b), BNn (c), and gr (d) additives, respectively. The crystalline integrity of these additives following shaping is confirmed by the selected area electron diffraction patterns (inset). Two-dimensional virtual slices obtained through non-destructive micro-CT analysis of extrudates containing copper fibers (e) or graphite (f) confirm the distribution of the additive phase within the whole body.

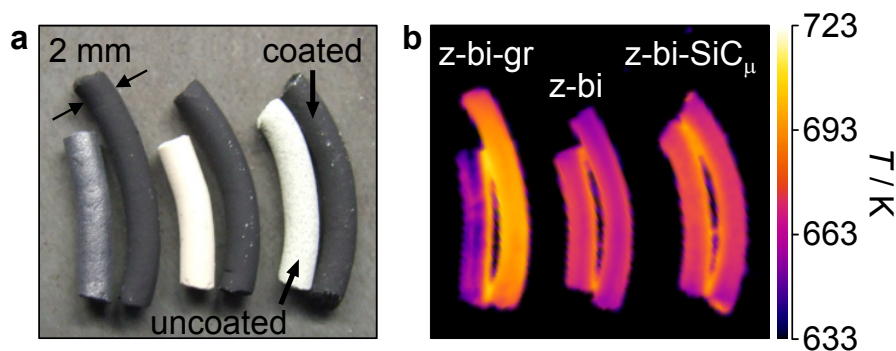


Figure A.16. The application of a temperature-stable coating of known emissivity ($\epsilon = 0.92$) permits the determination, using Planck's law, of the relative emissivity of the shaped bodies (a). The latter is composition dependent, which without correction can prevent the direct comparison of the actual surface temperature of the bodies. Due to their highly reflective surface, the largest temperature difference between the coated and uncoated states is observed for the graphite-containing bodies (b). The significantly higher temperature observed for the coated graphite sample stems from its high thermal conductivity. The color scale (right) corresponds to the specific photon intensities of detected IR radiation.

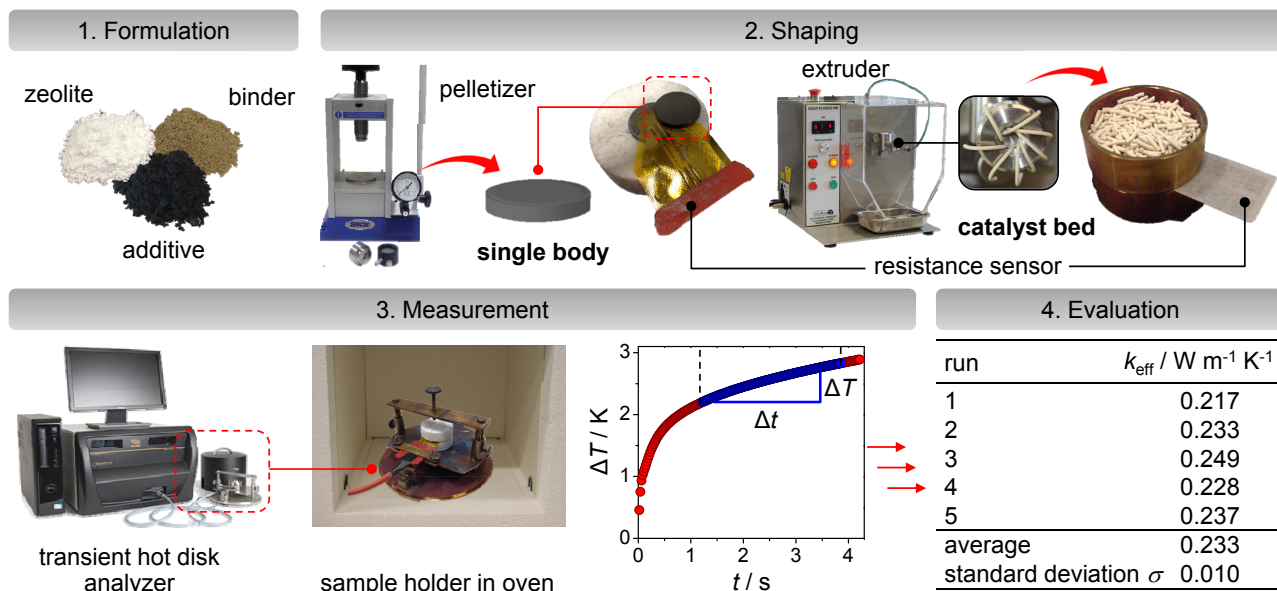


Figure A.17. Thermal conductivity assessment. Experimental protocol to assess the thermal conductivity of shaped catalysts. The component powders are first pelletized for the measurement of single bodies or extruded or granulated for the measurement of catalyst beds. A transient hot-plate technique is used to monitor the temperature change in response to the power input and the acquired data are subsequently evaluated.

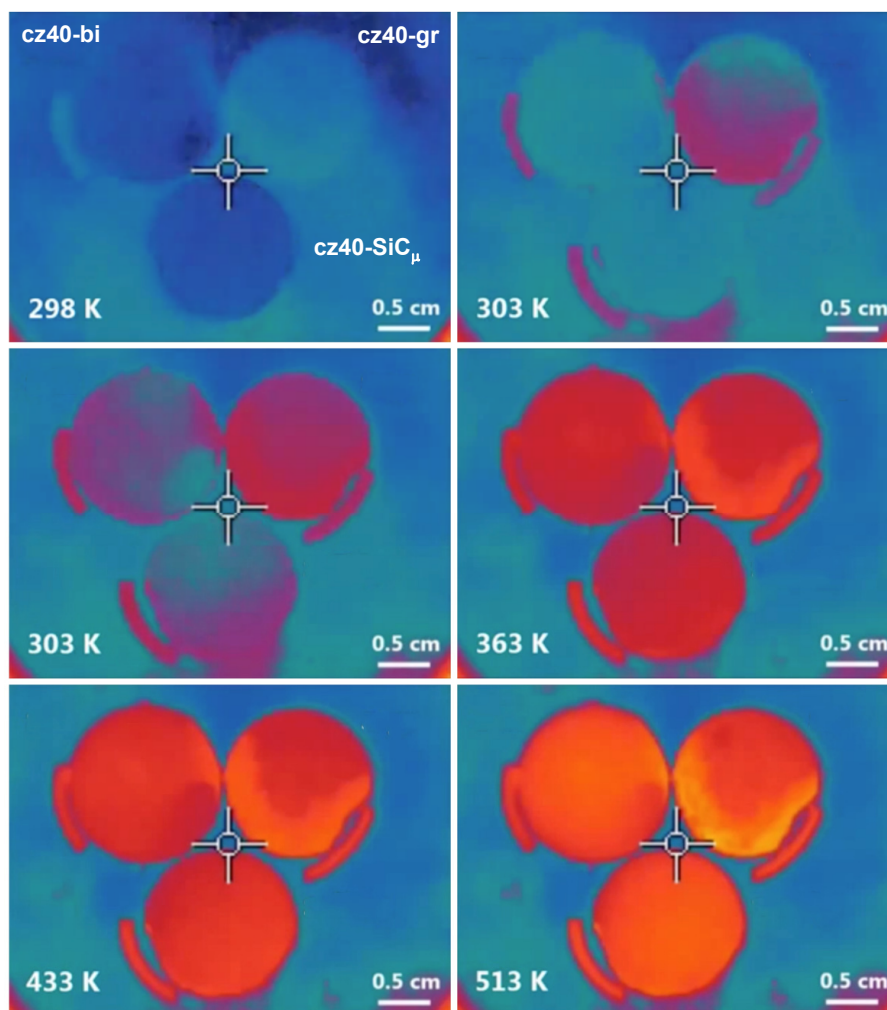


Figure A.18. The additive free (cz40-bi), micro-sized SiC (cz40-SiC_μ), and graphite-containing (cz40-gr) catalyst pellets are imaged by infrared thermography during continuous heating at 10 K min⁻¹ from 298–523 K. Selected frames are shown here. Lacquer-coated extrudates of equivalent composition are included for emissivity correction in order to accurately compare the heat-transfer properties.

Appendix B

List of Publications

Doctoral Publications

L. Borchardt, N.-L. Michels, S. Mitchell, T. Nowak, J. Pérez-Ramírez

Structuring Zeolite Bodies for Enhanced Heat-Transfer Properties

Micropor. Mesopor. Mater. **2014**, submitted

N.-L. Michels, S. Mitchell, J. Pérez-Ramírez

Effects of Binders on the Performance of Shaped Hierarchical MFI Zeolites in Methanol-to-Hydrocarbons

ACS Catal. **2014**, *4*, 2409-2417 (front cover)

M. Milina, S. Mitchell, N.-L. Michels, J. Kenvin, J. Pérez-Ramírez

Interdependence Between Porosity, Acidity, and Catalytic Performance in Hierarchical ZSM-5 Zeolites Prepared by Post-Synthetic Modification

J. Catal. **2013**, *308*, 398-407

S. Mitchell, N.-L. Michels, G. Majano, J. Pérez-Ramírez

Advanced Visualization Strategies Bridge the Multidimensional Complexity of Technical Catalysts

Curr. Opin. Chem. Eng. **2013**, *2*, 304-311

S. Mitchell, N.-L. Michels, J. Pérez-Ramírez

From Powder to Technical Body: the Undervalued Science of Catalyst Scale-up

Chem. Soc. Rev. **2013**, *42*, 6094-6112 (inside cover)

S. Mitchell*, N.-L. Michels*, K. Kunze, J. Pérez-Ramírez

*these authors contributed equally

Visualization of Hierarchically-Structured Zeolite Bodies from Macro to Nano Length Scales

Nat. Chem. **2012**, *4*, 825-831

N.-L. Michels, S. Mitchell, M. Milina, K. Kunze, F. Krumeich, F. Marone, M. Erdmann, N. Marti, J. Pérez-Ramírez

Hierarchically Structured Zeolite Bodies: Assembling Micro-, Meso-, and Macroporosity Levels in Complex Materials with Enhanced Properties

Adv. Funct. Mater. **2012**, *22*, 2509-2518

J. Pérez-Ramírez, S. Mitchell, D. Verboekend, M. Milina, N.-L. Michels, F. Krumeich, N. Marti, M. Erdmann

Expanding the Horizons of Hierarchical Zeolites: Beyond Laboratory Curiosity towards Industrial Realization

ChemCatChem **2011**, *3*, 1731-1734

Pre-Doctoral Publications

N.-L. Michels, A. Kapalka, A.A. Abd-El-Latif, H. Baltruschat, C. Comninellis

Enhanced Ammonia Oxidation on BDD Induced by Inhibition of Oxygen Evolution Reaction

Electrochem. Commun. **2010**, *12*, 1199-1202

A. Kapalka, A. Katsaounis, N.-L. Michels, A. Leonidova, S. Souentie, C. Comninellis, K. M. Udert

Ammonia Oxidation to Nitrogen Mediated by Electrogenerated Active Chlorine on Ti/PtO_x-IrO₂

Electrochem. Commun. **2010**, *12*, 1203-1205

Appendix C

Presentations

SCS Fall Meeting 2014, Zurich, Switzerland, 2014

Poster: "Effects of Binders on the Performance of Shaped Hierarchical MFI Zeolites in Methanol-to-Hydrocarbons"

N.-L. Michels, S. Mitchell, J. Pérez-Ramírez

Poster: "Structuring high-thermal conductivity catalyst bodies"

N.-L. Michels, L. Borchardt, S. Mitchell, J. Pérez-Ramírez

6th International FEZA Conference, Leipzig, Germany, 2014

Poster: "Effects of Binders on the Performance of Shaped Hierarchical MFI Zeolites in Methanol-to-Hydrocarbons"

S. Mitchell, N.-L. Michels, M. Milina, J. Pérez-Ramírez

EuropaCat XI - 20 Years of European Catalysis and Beyond, Lyon, France, 2013

Talk: "Towards the Rational Scale-up of Shaped Hierarchical Zeolite Catalysts for Methanol-to-Olefins"

N.-L. Michels, S. Mitchell, M. Milina, J. Pérez-Ramírez

5th International Symposium on Advanced Micro- and Mesoporous Materials, Varna, Bulgaria, 2013

Poster: "Designing Hierarchical Zeolite Catalysts for Methanol-to-Olefins"

N.-L. Michels, S. Mitchell, J. Pérez-Ramírez

SCS Fall Meeting 2013, Zurich, Switzerland, 2013

Poster: "Hierarchical Zeolite Catalysts: from Powders to Technical Shapes"

N.-L. Michels, S. Mitchell, M. Milina, J. Pérez-Ramírez

SCS Fall Meeting 2012, Zurich, Switzerland, 2012

Poster: "Scale-up of Hierarchically Structured Zeolite Catalysts"

N.-L. Michels, S. Mitchell, M. Milina, J. Pérez-Ramírez (Award for the Best Poster Presentation)

15th International Congress on Catalysis (ICC) 2012, Munich, Germany, 2012

Poster: "Hierarchical Zeolite Catalysts: from Powders to Technical Shapes"

N.-L. Michels, S. Mitchell, M. Milina, J. Pérez-Ramírez

Appendix D

Cover Gallery

Based on the work embodied in this thesis, two covers were published in distinct journal, which are presented on the following pages. Each cover comes along with a short explanation to illustrate the scientific background.

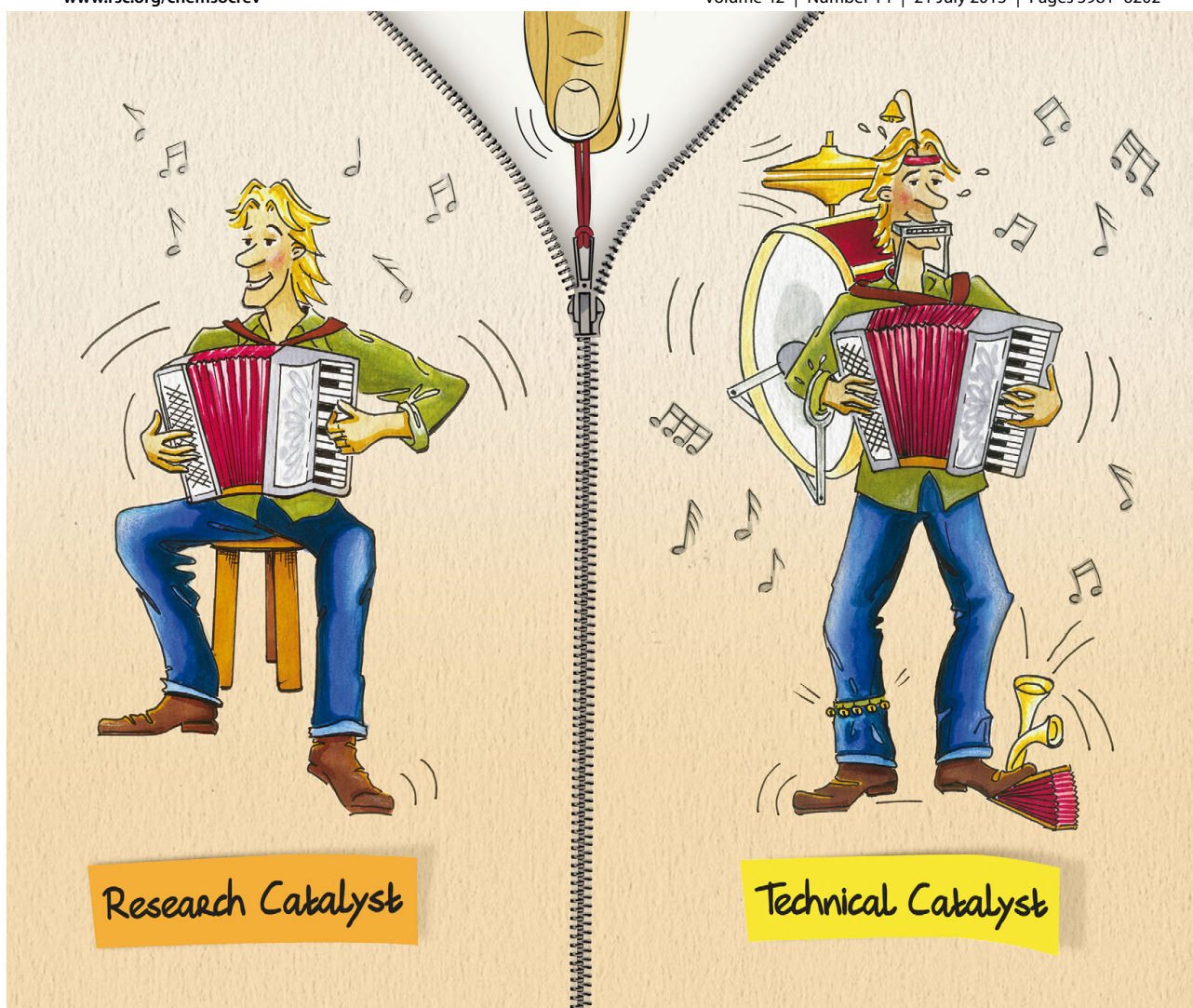
This (inside) cover relates to a review published in Chemistry Society Reviews, and is based on **Chapter 1**. It portrays the contrast between a research and a technical catalyst that can be likened to the difference between a solo player and a one-man orchestra. As opposed to the pure sound of a single instrument, in the latter case an ensemble of musical instruments have to be harmonized to ensure a good performance, which is akin to coordinating the distinct functions of the multiple constituent phases in industrial catalysts.

Chem Soc Rev

Chemical Society Reviews

www.rsc.org/chemsocrev

Volume 42 | Number 14 | 21 July 2013 | Pages 5981–6202



ISSN 0306-0012

RSC Publishing

REVIEW ARTICLE

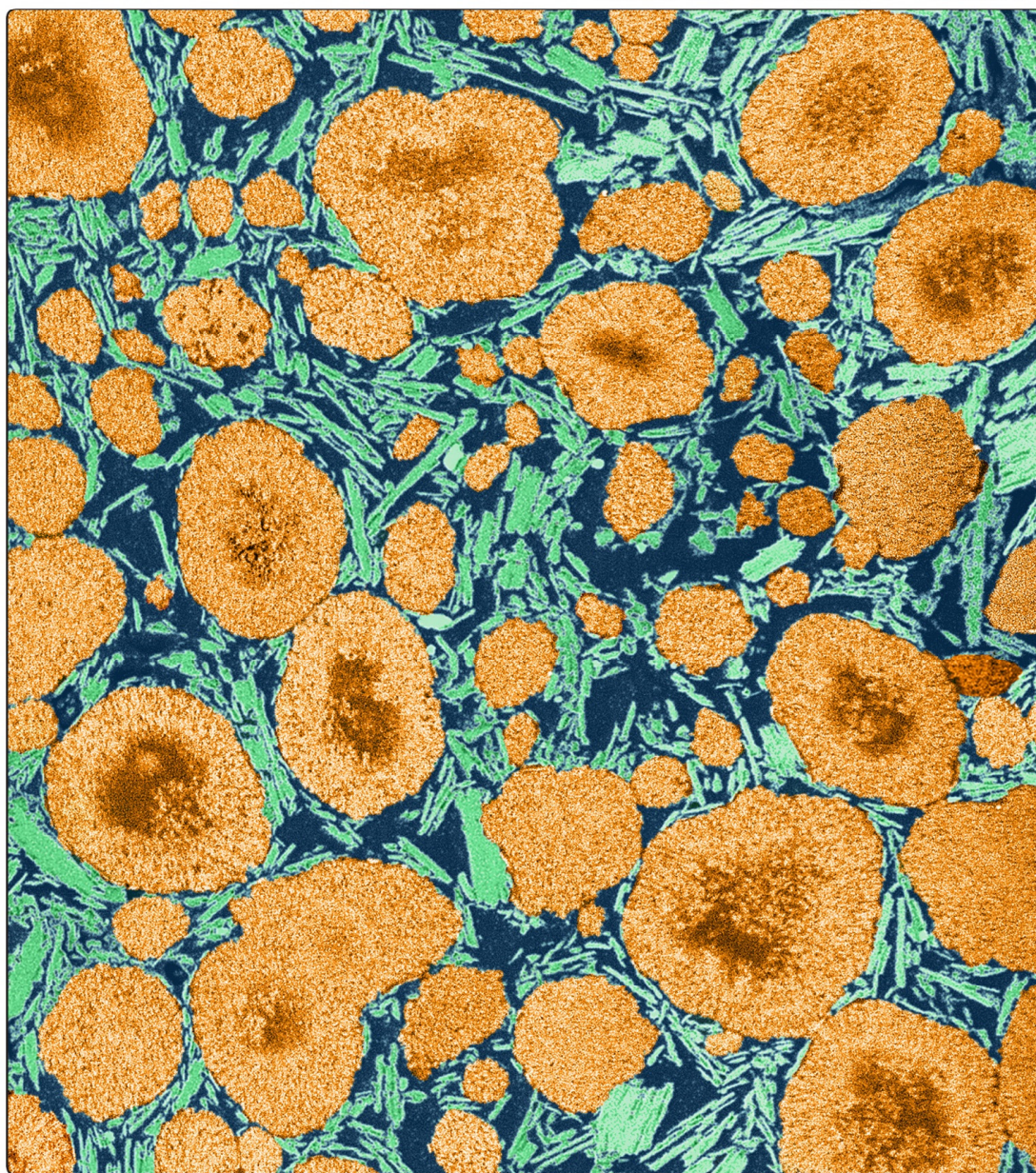
Sharon Mitchell, Nina-Luisa Michels and Javier Pérez-Ramírez

From powder to technical body: the undervalued science of catalyst scale up

This cover, based on results presented in **Chapter 4**, shows an artificially colored focused ion beam-scanning electron micrograph of a kaolin-bound ZSM-5 extrudate. The corresponding article published in ACS Catalysis assesses the complexity of harmonizing the interaction between the zeolite and binder phases for the catalytic conversion of methanol to hydrocarbons. The major differences in performance observed highlight the critical need to rationalize the role of additives in heterogeneous catalysis.

ACS Catalysis

AUGUST 2014 VOLUME 4 NUMBER 8



Appendix E

Curriculum Vitae

Name	Nina-Luisa Michels
Date of birth	May 20 th , 1986
Place of birth	Munich, Bavaria
Nationality	German

Education

2010 – 2014	Ph.D. under the supervision of Prof. Dr. J. Pérez-Ramírez at ETH Zurich, Switzerland
2008 – 2010	M.Sc. studies in Chemical & Biochemical Engineering, EPF Lausanne, Switzerland
2007 – 2008	Exchange year at McGill University, Montreal, Canada
2005 – 2008	B.Sc. studies in Chemistry & Chemical Engineering, EPF Lausanne, Switzerland

